CENTRUM BADAŃ KOSMICZNYCH
POLSKIEJ AKADEMII NAUK

DOCTORAL THESIS

in the field of **Exact and Natural Sciences**
in the discipline of **Earth and Environmental Sciences**

---

# Multi-approach Chronostratigraphic Reconstruction of Tharsis Volcanism in the Arsia Mons-Noctis Labyrinthus province, Mars

---

mgr Pierre-Antoine TESSON

*Supervisor:*
dr hab. Daniel MÈGE

Warsaw, 2023

## Abstract

The eruptive activity of the largest volcanic province on Mars, the Tharsis dome, has spanned most of the Martian geologic history, forming extensive flood lava plains, giant shield volcanoes, volcanic rift zones, airfall deposits, and countless individual lava flows, most of them still unmapped. Constraining the eruptive rate is critical to magma production models, which in turn improve models of Mars' internal evolution. However, estimating the eruptive rate requires careful reconstruction of the chronology and extent of the volcanic products. In this work, the Amazonian (3.0-0 Ga) eruptive sequence is reconstructed at Arsia Mons, a shield volcano at Tharsis. To do so, two approaches are followed. First, an integrated workflow, AROMAS (Automated Reconstruction Of Morphology And Stratigraphy), was developed. It generates a chronostratigraphic map of lava flows from digitised contacts with no flow number limitation. Additionally, the workflow makes it possible to infer some lava flow morphological properties, such as length, width, thickness, and the fractal dimension of the flow boundaries, opening perspectives to better understand lava rheology. The workflow is validated using a terrestrial example, a set of lava flows erupted from the upper Pleistocene La Corona volcano in Lanzarote, Spain, where fieldwork was conducted. It is applied to a set of 424 overlapping lava flows located southeast of Arsia Mons. A chronostratigraphic map at 1:50,000 is generated. The combination of relative stratigraphy from AROMAS with impact crater retention age determination shows that the latest effusive activity at Arsia Mons spanned 190 to 350 Myrs, with a peak at ∼150 Ma and an average effusive eruption rate of 0.23-0.98 $km^3$/Myr. These lavas post-date 400-600 Ma flows, as well as extensive loose material deposits forming bedform-like features. The second approach followed in this work consists of a morphometric analysis of such features, located on the slopes of Noctis Labyrinthus, the complex canyon system located east of Arsia Mons. Digital terrain models (DTMs) were generated by joint photogrammetric and photoclinometric processing of stereo imagery obtained by the ExoMars Trace Gas Orbiter Colour and Stereo Surface Imaging System (CaSSIS). The models have a vertical precision 5 times better than the 4.6 m/pixel horizontal resolution, and similar to DTMs generated using the 0.25 m/pixel stereoscopic images obtained by the Mars Reconnaissance Orbiter HiRISE camera. The capabilities of CaSSIS for geological interpretation of metre-scale morphologies are demonstrated by morphometric analysis of these bedforms, which are shown to be composed of cemented and eroded mobile material propagated from an overlying, 100 m thick, pyroclastic level deposited on top of Hesperian (3.7-3.0 Ga) flood basalts. This work highlights the complex volcanic evolution of the eastern Tharsis region, which probably echoes the evolution of the other giant shield volcanoes. It also provides tools for the automated extraction of key morphometric parameters from highly complex multi-phased volcanic landforms, which can be further used to constrain volcano dynamics and mechanical properties of the erupted products.

## Streszczenie

Aktywność erupcyjna w obrębie największej prowincji wulkanicznej na Marsie, Tharsis, obejmowała większość historii geologicznej Marsa, przybierając postać rozległych pokryw lawowych, gigantycznych wulkanów tarczowych ze strefami ryftów wulkanicznych, osadów pylastych oraz niezliczonych pojedynczych potoków lawowych, z których większość dotąd nie została wykartowana. Ustalenie tempa erupcji jest kluczowe dla modeli tworzenia się magmy, które z kolei umożliwiają lepsze zrozumienie ewolucji wnętrza Marsa. Jednakże oszacowanie tempa erupcji wymaga starannego odtworzenia chronologii i zasięgu produktów erupcji wulkanicznych. W ramach tej pracy została zrekonstruowana sekwencja erupcji epoki amazońskiej (3.0-0 mld lat) na wulkanie tarczowym Arsia Mons, położonym w obrębie kopuły Tharsis. Zastosowano w tym celu dwie metody. Po pierwsze, opracowano zintegrowany przepływ pracy o nazwie AROMAS (Automated Reconstruction Of Morphology And Stratigraphy). Generuje on mapy stratygraficzne potoków lawowych ze zdigitalizowanych linii granicznych, bez ograniczeń co do liczby potoków. Dodatkowo metoda ta umożliwia wnioskowanie o niektórych morfologicznych cechach potoku lawowego, takich jak długość, szerokość i grubość, a także wymiar fraktalny granic potoku, otwierając perspektywy lepszego zrozumienia reologii lawy. Metoda została zweryfikowana na przykładzie z Ziemi, z zastosowaniem serii potoków lawowych z wulkanu z epoki późnego plejstocenu, La Corona (Lanzarote, Hiszpania), gdzie przeprowadzono badania terenowe. Zastosowano ją do zestawu 424 nieprzeobrażonych, zachodzących na siebie potoków lawowych, zlokalizowanych na południowy wschód od Arsia Mons. Wygenerowano mapę stratygraficzną w skali 1:50 000. Połączenie względnej stratygrafii z AROMAS z określeniem wieku retencji kraterów uderzeniowych pokazuje, że najmłodsza aktywność efuzywna na Arsia Mons trwała 190-350 milionów lat, osiągając szczyt ∼150 milionów lat temu, przy średnim tempie erupcji efuzywnej wynoszącym 0.23-0.98 $km^3$ na milion lat. Lawy są pozostałością po erupcjach sprzed 400-600 milionów lat, i są młodsze niż rozległe osady luźnego materiału, które utworzyły formy dna. Drugą zastosowaną w tej pracy metodą jest analiza morfometryczna takich form, zlokalizowanych na zboczach Noctis Labyrinthus, złożonego systemu kanionów na wschód od Arsia Mons. Numeryczne modele terenu zostały wygenerowane poprzez połączone przetwarzanie fotogrametryczne i fotoklinometryczne obrazów stereo uzyskanych przez kamerę CaSSIS (Colour and Stereo Surface Imaging System) misji ExoMars. Modele te mają precyzję pionową 5 razy większą niż rozdzielczość pozioma wynosząca 4,6 m/piksel, zbliżoną do modeli terenu generowanych przy użyciu obrazów stereoskopowych o rozdzielczości 0,25 m/piksel uzyskanych przez kamerę HiRISE misji Mars Reconnaissance Orbiter. Możliwości geologicznej interpretacji morfologii rzędu metrów z użyciem CaSSIS zostały zademonstrowane przez analizę morfometryczną form dna, złożonych ze scementowanego, zerodowanego materiału pochodzącego z

nadległego, 100-metrowego, rozległego poziomu osadów piroklastycznych osadzonego na podłożu z hesperiańskiej (3.7-3.0 mld lat) pokrywy bazaltowej. Niniejsza praca podkreśla złożoną ewolucję wulkanów wschodniej części regionu Tharsis, która prawdopodobnie odzwierciedla ewolucję innych olbrzymich wulkanów tarczowych. Zapewnia również narzędzia do automatycznego uzyskania kluczowych parametrów morfometrycznych z bardzo złożonych, wielofazowych form wulkanicznych, które mogą być wykorzystane do ustalania dynamiki wulkanów i właściwości mechanicznych produktów erupcji wulkanicznych.

# *Acknowledgements*

*This work was supported by the EXOMHYDR project financed within the framework of the TEAM Programme of the Foundation for Polish Science (FNP - agreement TEAM/2016-3/20, project POIR.04.04.00-00-3CD8/16), as well as the Europlanet 2024 Geologic Mapping of Planetary Bodies (GMAP) project.*

*I would like to express my sincere gratitude to my supervisor, Daniel Mège, for his invaluable guidance, support, and encouragement throughout my PhD. I would also like to thank Joanna Gurgurewicz for her continuous support and help during the last years.*

*Finally, I would like to thank my family, my friends and my partner for their unwavering love and support. Their encouragement has been a constant source of inspiration and motivation.*

# Contents

# List of Figures

# List of Tables

# List of Abbreviations

| | |
|---|---|
| **AROMAS** | **A**utomated **R**econstruction **O**f **S**tratigraphy **A**nd **M**orphology |
| **ASP** | **A**mes **S**tereo **P**ipeline |
| **BLF** | **B**edform-**L**ike **F**eature |
| **CaSSIS** | **C**olour and **S**tereo **S**urface **I**maging **S**ystem |
| **CaST** | **C**aSSIS **S**cience **T**argeting |
| **CaTL** | **C**aSSIS **T**argeting **L**ead |
| **CSFD** | **C**rater **S**ize **F**requency **D**istribution |
| **CTX** | **C**on**T**e**X**t Camera |
| **DEM** | **D**igital **E**levation **M**odel |
| **DTM** | **D**igital **T**errain **M**odel |
| **EDR** | **E**xperimental **D**ata **R**ecord |
| **ESA** | **E**uropean **S**pace **A**gency |
| **HiRISE** | **H**igh **R**esolution **I**maging **S**cience **E**xperiement |
| **HRSC** | **H**igh **R**esolution and **S**tereo **C**amera |
| **INAF** | **I**stituto **N**azionale di **A**stro**F**isica |
| **ISIS** | **I**ntegrated **S**oftware for **I**magers and **S**pectrometers |
| **JMARS** | **J**ava **M**ission-planning and **A**nalysis **R**emote sensing |
| **LD** | **L**ayered **D**eposit |
| **LLD** | **L**ight-toned **L**ayered **D**eposit |
| **LIP** | **L**arge **I**gneous **P**rovince |
| **MOLA** | **M**ars **O**rbiter **L**aser **A**ltimeter |
| **MRO** | **M**ars **R**econnaissance **O**rbiter |
| **MGS** | **M**ars **G**lobal **S**urveyor |
| **NASA** | **N**ational **A**dministration of **S**pace and **A**eronautics |
| **PDS** | **P**lanetary **D**ata **S**ystem |
| **PSA** | **P**lanetary **S**cience **A**rchive |
| **SNC** | **S**hergottites **N**akhlites **C**hassignites |
| **SPICE** | **S**pacecraft **P**lanet **I**nstrument **C**-matrix **E**vents |
| **STP** | **S**hort **T**erm **P**lanning |
| **THEMIS** | **TH**ermal **EM**ission **I**maging **S**ystem |
| **TGO** | **T**race **G**as **O**rbiter |
| **TPW** | **T**rue **P**olar **W**ander |
| **USGS** | **U**nited **S**tates **G**eological **S**urvey |

# Chapter 1

# Tharsis: A Volcanic Province on Mars

## Introduction

In the 1960s and early 70s, NASA launched a total of 10 missions dedicated to the exploration of planets in the inner solar system. In 1964, Mariner 4 did the first successful flyby of Mars and provided the first-ever close-up picture of the surface. In 1971, the Mariner 9 spacecraft became the first to orbit the planet and eventually managed to image about 85% of the surface. One of the most exciting discoveries at the time was the giant volcanoes of the Tharsis bulge and the lobate lava flows mantling the surface (Carr, 1973; Masursky, 1973; McCauley et al., 1972).
This discovery showed that volcanism was once widespread at the surface of Mars and the shield volcanoes were compared to their terrestrial intraplate counterparts (Carr, 1973). In fact, it was quickly understood that plate tectonics was absent on Mars and that Martian crust immobility with respect to the mantle allowed the shields to grow throughout geological time. The formation of Martian giant volcanoes over a static hotspot in turn indicates that a moving plate is not a prerequisite to shield development as some people were arguing back then (Carr, 1973).
This approach perfectly illustrates that planetary science constantly goes back and forth between terrestrial examples that are used to understand what we see on other planets, and in return what we see on other planets teaches us things about the Earth.

## 1.1 Tharsis formation: origin, evolution and consequences

### 1.1.1 Extent and origin

Although Tharsis has no precisely defined boundaries, it commonly refers to a 10 to 30 million km$^2$ wide area located between 300°E and 215°E of longitude, and from 55°N to 43°S of latitude (Fig 1.1). It consists of an up to 11 km high plateau (excluding the shield volcanoes) bounded by Amazonis and Chryse Planitiae in the west and the east, and Alba Mons and Thaumasia Planum in the north and the south. Tharsis is often referred to as the "Tharsis bulge" or "dome" due to its height and overall shape. It is the main volcano-tectonic province on Mars, where features

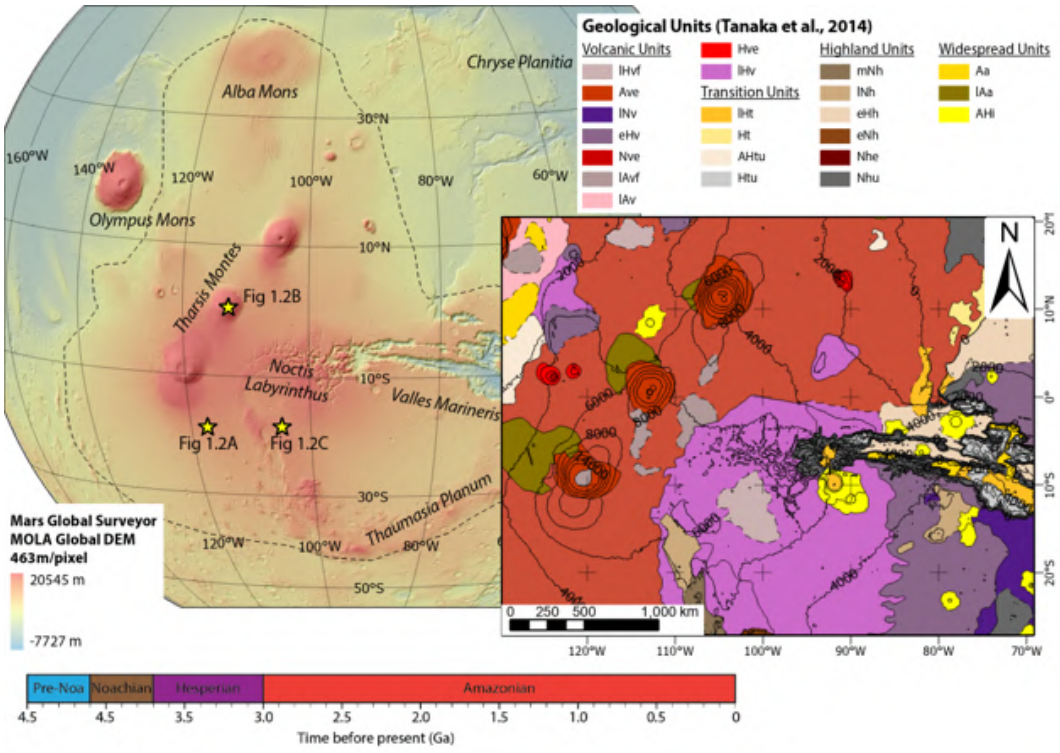


FIGURE 1.1: **Top left**: Location of the Tharsis province on Mars (dashed line) with Mars Orbiter Laser Altimeter (MOLA) hillshade as a background and MOLA Global Digital Elevation Model (463 m/pixel) for elevation. Stars indicate the locations of Fig 1.2. **Right**: Geological map from (Tanaka et al., 2014) focused on Tharsis Montes and Noctis Labyrinthus. Contour lines derived from MOLA Global DEM, spaced by 2000 m. Unit descriptions: e = early, m = mid, l = late; N = Noachian, H = Hesperian, A = Amazonian; v = volcanic, e = edifices, f = field, t = transition, u = unit, h = highland; a = apron, i = impact. **Bottom**: geological timescale.

like lava flows and shield volcanoes (Fig. 1.2A & B - Carr, 1973), concentric and radial, contractional and extensive faults (Fig. 1.2C - Bouley et al., 2018) that spans the whole Hesperian and Amazonian periods can be found (Fig. 1.1).

Many models were proposed to explain the Tharsis dome formation, but the most common interpretation involves a single, putative mantle plume located underneath the province (Fig. 1.3 - Costa et al., 2020; Hartmann, 1973; Mège and Masson, 1996b), similar to terrestrial hotspots found, for instance, under Hawaii (J. T. Wilson, 1963) or the Canary Islands (Carracedo et al., 1998). This interpretation is supported by the distribution and orientation of the tectonic features found on Tharsis (Bouley et al., 2018; Mège & Masson, 1996a). In addition, deep-mantle mineralogical models were found to be consistent with a single, long-lived plume hypothesis (Breuer et al., 1998; Plesa et al., 2022). Recently, evidence has been found for a similar and active mantle plume underneath Elysium Planitia, the other major volcano-tectonic province on Mars (Broquet & Andrews-Hanna, 2022), as demonstrated by recent volcanic (Horvath et al., 2021) and seismic activity (Giardini et al., 2020).

Combined with the lack of plate tectonics on Mars, a long-lived plume under Tharsis could have induced a flexure of the lithosphere, partial melting that would feed

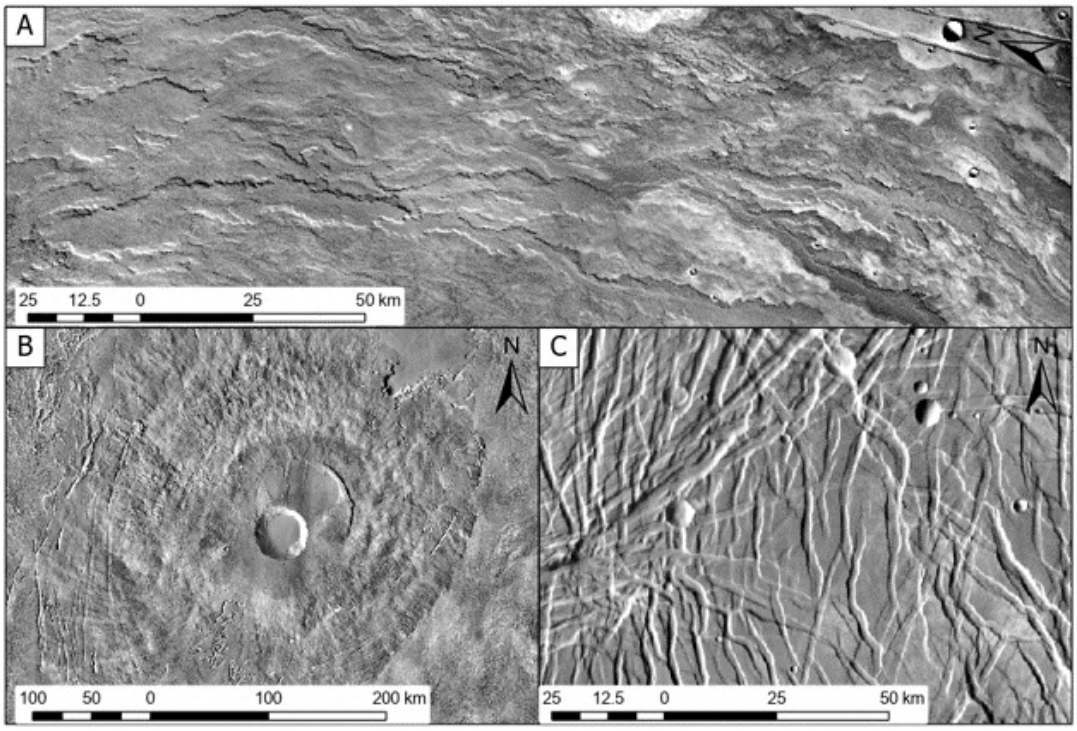


FIGURE 1.2: Examples of volcano-tectonic features found in the Tharsis Province. **A**: Elongated lobate lava flows south of Arsia Mons. **B**: Pavonis Mons, a 14 km-high giant shield volcano. **C**: Extensional tectonic faults and grabens south of Noctis Labyrinthus. Images: THEMIS Day-IR.

magma chambers, intense volcanism and the growth of the province.

### 1.1.2 Basaltic volcanism

The partial melting of the crust induced by the hot ascending mantle plume (Fig. 1.3) produced an important amount of magma, triggering intense volcanic activity at the surface. Geochemical analysis of the SNC (Shergottites – Nakhlites - Chassignites) Martian meteorites have revealed that they are of basaltic composition with a silica content ranging from 37.4 wt% to 51.3 wt% (Lodders, 1998). These findings combined with the analysis of Martian soils during Viking missions (Banin et al., 1992) confirmed the mafic to ultramafic nature of Martian lavas. The most notable shield volcanoes are the Tharsis Montes (i.e., Ascraeus, Pavonis and Arsia Mons) and Olympus Mons, although the latter is not strictly located on the Tharsis dome. Apart from their size (>21 km high for Olympus Mons), their gently-sloped shape was found to correspond to terrestrial Hawaiian volcanoes (Carr, 1973; Greeley and Spudis, 1981) which is consistent with the mafic composition of their lavas, characteristic of such eruptive style.

Although the large shields stand out on the surface, volcanic activity was far from being constrained to these edifices only. On Earth, flood basalts in Large Igneous Provinces (LIP) and their link to mass extinctions have been described and studied for as long as modern geology exists (Clapham and Renne, 2019; Rampino and

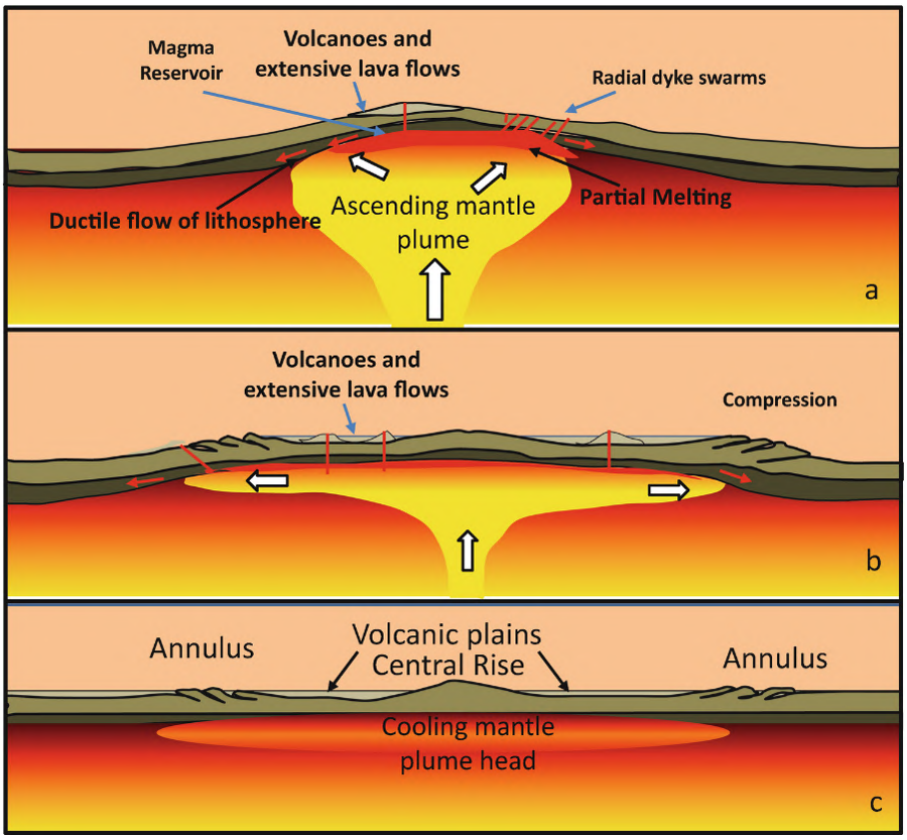


FIGURE 1.3: Mantle plume model proposed to explain the Tharsis dome formation. Extracted from (Stevenson, 2018)

Stothers, 1988; Washington, 1922). Flood basalts, or plateau basalts, refer to the wide emplacement of lava sheets over tens to hundreds of km$^2$, forming plateaus that, once eroded, leave a distinctive step pattern, hence giving them the name "traps", from the Swedish word for "steps". These lavas are thought to be related to an underlying mantle plume onset (White & McKenzie, 1995) and develop without any construction of an edifice, as opposed to central volcanism. Early studies of the surface of Mars revealed that at least 80% of the Martian volcanic terrains (themselves covering almost half of the global surface) are made of basaltic flood plains and plateaus (Greeley and Schneid, 1991; Greeley and Spudis, 1981; Keszthelyi and McEwen, 2007; Scott and Tanaka, 1986). The surface of flood plains is referred to in the literature as ridged plains as it frequently displays wrinkle ridges, similar to those found in lunar maria, which are also interpreted as lava plains (Spudis, 2015). The origin of ridged plains is still debated as some authors highlight the lack of distinctive flow features as opposed to the well-defined lobate flows of Tharsis, indicating long-term, low effusion rate and low viscosity eruptions (Mouginis-Mark et al., 2022).

In addition to the giant shields, smaller and lower shields were also identified in Tharsis with less than tens of kilometres in diameter and less than a few hundred metres high (Hauber et al., 2009; Hodges and Moore, 1994; Moore and Hodges, 1980). These low shields are associated with fissures and were often compared to

the volcanism found in the Snake River plains, in the United States (Greeley, 1982; Plescia, 1981). Such volcanism (referred as "plain-style volcanism" – Greeley, 1982) is thought to be of an intermediate style between basaltic flood plains and Hawaiian shield volcanism (Hauber et al., 2009) and was found on Mars to be associated with recent (few tens of million years) lava field emplacement in the Tharsis region (Hauber et al., 2011).

### 1.1.3 Explosive volcanism

Flood basalts, shield volcanoes and lobate lava flows correspond to the effusive style of volcanism. On Earth, volcanism is commonly classified on a spectrum from explosive to effusive activity (e.g. Adams et al., 2006; Cassidy et al., 2018; Kusanagi and Matsui, 2000). As mentioned previously, Martian volcanism is usually compared to the Hawaiian eruptive style, which is little to no explosive at all. Explosivity in volcanism is caused by the presence of volatile elements in the magma which, during magma ascent, expands due to the decrease of pressure. While Mars is known to have sustained a thick atmosphere at the beginning of its geological history, it is thought to have decreased significantly at the end of Hesperian. This, combined with the confirmed presence of volatiles at or near the surface (e.g. Boynton et al., 2002; Dundas et al., 2018; Vincendon et al., 2010) should therefore favour explosive eruptions on Mars (Brož et al., 2021; L. Wilson and Head, 1994).
Several surface features associated with the explosive style of volcanism have been identified on Mars, such as stratovolcanoes (e.g., Zephyria Tholus – Stewart and Head, 2001), cinder cones (e.g., Brož and Hauber, 2012) or tuff rings (e.g., Brož and Hauber, 2013). Some large-scale outcropping deposits have been interpreted to be pyroclastic emplacements related to catastrophic episodes of explosive volcanic activity (e.g., Mouginis-Mark, 2002; Orosei et al., 2017; Whelley et al., 2021) although a strict characterisation of such deposits relying only on remote sensing is a non-trivial exercise. Despite these examples, it appears at first glance that explosive activity was quite scarce throughout the geological history of Mars as opposed to effusive activity.

### 1.1.4 Tharsis growth: deformation and chronology

The stress induced on the lithosphere by the formation of Tharsis has left the surface of Mars scattered with contractional and extensional tectonic features that are visible today (Fig. 1.2C - e.g., Hartmann, 1973; Tanaka and Davis, 1988; Wise et al., 1979). From the study of their distribution and their cross-cutting relationships with dated geological units (through impact crater retention statistics), several authors have been able to reconstruct the chronology of Tharsis growth (Anderson et al., 2001; Bouley et al., 2018). It was formerly argued that Tharsis was already mostly emplaced at the end of Noachian (e.g., Anderson et al., 2001), however, Bouley et al. (2018) demonstrated that, although the growth had started during the Early

Noachian, it peaked during Late Noachian and Early Hesperian, and the deformation extended to the Amazonian period. This late Tharsis emplacement scenario is consistent with the orientation of valley networks of the same age (see the section below - Bouley et al., 2016).

## 1.2 The consequences of Tharsis formation on Mars

### 1.2.1 True Polar Wander (TPW)

Before Tharsis formation, numerical models have shown that the rotation axis position of the planet was controlled by the hemispheric dichotomy (i.e., the topographic difference between the northern and southern hemispheres – Smith et al., 1999; Zuber and Smith, 1997). The position of the current poles of Mars combined with orientation of Noachian/Early Hesperian valley networks has led many authors to believe the planet experienced a migration of its rotation axis (True Polar Wander - TPW) driven by the load of the Tharsis bulge (Bouley et al., 2016; Melosh, 1980; Roberts and Zhong, 2007). The TPW could explain the location of Tharsis at the equator nowadays and the alignment of valley networks along a paleo-equator nowadays (Bouley et al., 2016).

### 1.2.2 Consequences of intense volcanism on the atmosphere of Mars

The analysis of Martian soil carried out by the Viking landers revealed abundant sulphur deposition linked to volcanic activity output from the Tharsis region (Settle, 1979). Volcanic outgassing is thought to have been a major contribution to the evolution of the Martian atmosphere composition and pressure (e.g., Halevy and Head III, 2014). For instance, (Grott et al., 2011), estimated the total $CO_2$ contribution from volcanism was equivalent to 1 bar between 3.5 and 2.0 Ga. Such amount of volcanic output certainly had major consequences on the atmosphere of Mars, increasing the greenhouse effect and the atmospheric pressure, in turn allowing liquid water to be stable at the surface, as opposed to present-day conditions (Farmer, 1976; Hecht, 2002). However, as summarised by Mouginis-Mark et al. (2022), understanding the effective contribution of volcanism on Mars' climate highly depends on how well we can estimate the intensity, nature, and frequency of eruptive events throughout the geological history of Mars.

## 1.3 Outstanding questions

### 1.3.1 Magma production and eruption rate

As it was quickly understood that volcanism was prominent during the geological history of Mars, several attempts have been made to infer the magma production rate: i.e., the volume of magma produced by melting of the mantle or the crust that then migrates upward per unit of time. Greeley and Schneid (1991) estimated

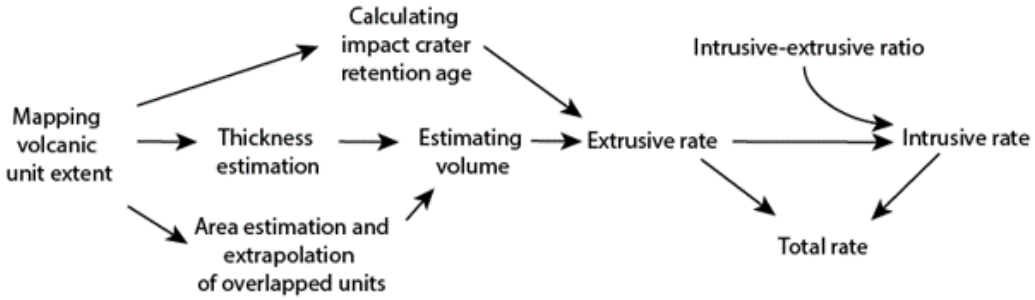


FIGURE 1.4: The method used by Greeley and Schneid (1991) to estimate the global magma production rate. The accuracy of the results highly depends on the intrusive-extrusive ratio choice, which is assumed to be close to the one measured on Earth.

that the total magma production rate in the last 3.8 billion years to be 0.17 $km^3.yr^{-1}$, compared to 26-34 $km^3.yr^{-1}$ on Earth. The method (Fig. 1.4) suffers from some limitations. For instance, as only the extruded material is visible, the intruded magma can only be inferred from an arbitrary ratio derived on Earth. Moreover, a significant part of the extruded material can be overlapped by younger eruptions, meaning that the older units' extent must be extrapolated to infer their volume accurately.
A similar approach can be carried out at a lower scale and provide a local estimation of the eruptive rate (e.g., J. A. Richardson et al., 2017). The rate of eruptions at a single edifice can therefore be compared with the predictions from magma cooling models within the plumbing system, which puts a constraint on the maximum time interval between two eruptive events (Mouginis-Mark et al., 2022; L. Wilson et al., 2001a). However, comparing results obtained from the chrono-stratigraphic analysis carried out with impact crater chronology with thermal models (e.g., Baratoux et al., 2011) can yield significantly different results (Mouginis-Mark et al., 2022). Such differences arise from the fact that impact crater size-frequency distribution (CSFD) cannot rely on absolute calibration from samples as it was done for the Moon thanks to the Apollo program (e.g., Hiesinger et al., 2012). Fortunately, the planned NASA Mars Sample Return mission (Muirhead et al., 2020) will allow for a better calibration of the absolute ages derived from impact crater counting.

### 1.3.2 Giant shield volcano internal structures

Shield volcanoes observed in the Tharsis region were quickly compared to basaltic low-shield edifices found in intraplate volcanic archipelagos like Hawaii. However, some differences exist between these and their Martian cousins. Apart from the obvious order of magnitude of difference in size between the giant Tharsis shields and their terrestrial counterparts, the giant shields of Tharsis Montes display a NE-SW trending rift zone indicating a link in their emplacement and evolution (Crumpler and Aubele, 1978). Remote sensing images also revealed elongated lava flows extending from the collapsed NE and SW flanks of the volcanoes associated with the rift zone, hence giving them the name "rift aprons" (Bleacher et al., 2007). As only

the surface is accessible, the study of the rift aprons and the chronology of their development can provide valuable insights into the internal structure of the volcanoes. This internal structure and the pathway of magma through the edifice to the surface are still poorly known as the source vents are difficult to identify despite the availability of high-resolution datasets (Mouginis-Mark et al., 2022).

### 1.3.3 Lava flow characteristics

From the early studies of the Martian surface, several attempts have been made to retrieve rheological characteristics of the lava from their flow morphometrics (e.g., Baloga, 2003; Hulme, 1976; Wiedeking et al., 2023). On Earth, basaltic lava flows are commonly classified into two types: rough and brecciated "ʻaʻā" and smooth glassy "pāhoehoe", which are words of Hawaiian origin (Harris et al., 2017). A third type named "blocky" lava also exists but refers to thick brecciated silicic lava (Macdonald, 1953). Whether a lava will flow into an ʻaʻā or a pāhoehoe flow, depends on its rheological proprieties as well as the velocity of emplacement, and can transition from one type to the other along the flow (Hon et al., 2003; Peterson & Tilling, 1980). Between these two types, a spectrum of different lava can exist such as toothpaste (Rowland & Walker, 1987), spiny (e.g. Pedersen et al., 2017), rubbly and slabby lavas (e.g. Kuntz et al., 1986). These types are also known as transitional types and usually are found among mafic lava flows (Schaefer et al., 2021).

From the remote sensing point of view, Martian lobate lava flows strike similarities with their terrestrial counterparts in terms of morphology, texture and surface (Wadge and Lopes, 1991). The striking difference is however in the extent of Martian lava flows, with some individual flows spanning hundreds of kilometres. The difference in gravity field and atmospheric pressure between Mars and the Earth implies that mechanisms of emplacement could vary between the two planetary bodies. For instance, processes like lava flow inflation can also add complexity to the retrieval of rheological parameters of the lava solely from the morphometrics (e.g. Giacomini et al., 2009). These challenges did not prevent many authors from proposing models of flow emplacement (e.g. Chevrel et al., 2013; Wiedeking et al., 2023; Zimbelman, 1998). Overall, the lava flows' morphology was found to be consistent with basaltic lavas, with both pāhoehoe and ʻaʻā flow types. (Crown and Ramsey, 2017), and emplaced during long-lived effusive eruptions, ranging from a few days to months (Hamilton et al., 2018).

A relative comparison of lava flows through time of emplacement however simplifies the equation by removing constant parameters (e.g., gravity and atmospheric pressure) and can reveal relative changes in viscosity. Registering such an evolution at an edifice and constraining it chronologically with impact crater retention age could provide valuable insights into understanding the evolution of the volcano itself. Mouginis-Mark et al. (2022) also pointed out that a method based on lava flow margin fractal dimension analysis that can allow the discrimination between

pāhoehoe and ‘a‘ā flows was developed on Earth (Bruno et al., 1992, 1994) but was never applied to Mars.

## 1.4 Arsia Mons: an evolved volcanic edifice

### 1.4.1 Tharsis Montes

Tharsis Montes is the name given to the three giant shield volcanoes sitting at the top of the Tharsis dome (Fig. 1.1): Ascraeus Mons, Pavonis Mons and Arsia Mons. Their sizes range from 350 to 500 km in diameter and from 8 to 15 km in height with respect to the surrounding plateaus, outmatching any shield volcano on Earth (Plescia, 2004b). The three aligned shield volcanoes are assumed to originate from a single magmatic source that was located under Arsia Mons and migrated northwards (Bleacher et al., 2007; Mège & Masson, 1996b)

### 1.4.2 Arsia Mons

Arsia Mons is the southernmost largest shield volcano of the three. It is composed of a 108 by 138 km caldera complex, significantly wider than the two other Tharsis Montes (Plescia, 2004a). The shield is bound to the northeast and southwest by younger and extensive lava aprons extruding from collapsed areas (Fig. 1.5 - Bleacher et al., 2007; Plescia, 2004a). The edifice is cross-cut by a series of concentric and linear grabens that extend from the caldera rim to the lava plains (Carr, 1974). To the west, fan-shaped glacial deposits can be found (Head & Marchant, 2003; Scanlon et al., 2015; Shean et al., 2007).
The construction of the main edifice is thought to have ended at 3.5 Ga but effusive activity in the form of lava flows was recorded at 2 Ga, 500 and 800 Ma on the shield flank (Werner, 2009). The age of the last effusive activity was found to be between 10-90 and 200-300 Ma in the caldera (J. A. Richardson et al., 2017).
Besides, evidence for explosive episodes was found by Ganesh et al. (2020) under the caldera floor using radar data. In addition, 40-50 m thick ash deposits were found by Mouginis-Mark (2002) around the rim of northeastern and southwestern collapses. The details of the Amazonian eruptive activity outside the Arsia central caldera, which led to the deposition of most rocks currently exposed on the southern Tharsis dome, remain poorly constrained. The available imagery demonstrates, however, a remarkable geological diversity and complexity. Unravelling the corresponding events is necessary to constrain the magmatic evolution of the edifice, of the Tharsis dome, and given its planet-long history and Tharsis geographical extent, the global thermal evolution of the Mars interior. Furthermore, ongoing volcanic activity would suggest ongoing hydrothermal systems providing energy and a solvent (water) and environmental parameters promoting the development of biotic processes (Hoehler et al., 2018; Westall et al., 2013). Investigating the form of the recent volcanic events at Arsia Mons is the topic of this work.

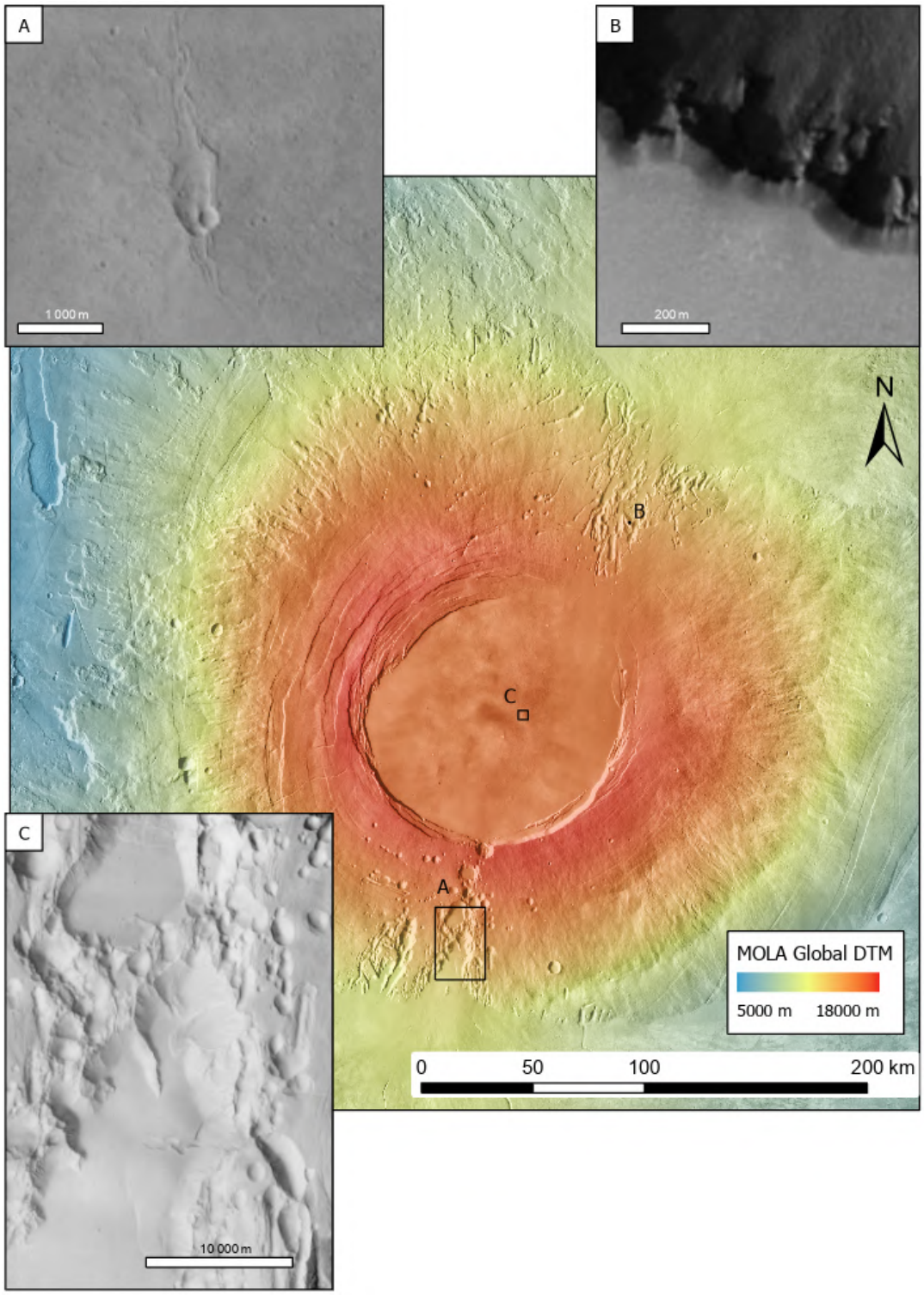


FIGURE 1.5: Arsia Mons volcano on a MOLA topography map superimposed onto a THEMIS Day image mosaic. Insets: **A**: Intra-caldera vent recorded by J. A. Richardson et al. (2017). **B**: Ash deposits around northern collapse pits in the northern rift zone identified by Mouginis-Mark (2002). **C**: Collapse depressions in the southern rift zone. CTX for close-up images and THEMIS Day-IR with coloured elevation from MOLA Global DTM for context.

## 1.5 Chrono-stratigraphic mapping

Investigation of a sample of the many lava flows that cover most of the southern Tharsis dome is the first part of this work. The extent of individual lava flows and an accurate reconstruction of their chronology of emplacement are obtained from stratigraphic relationships and/or crater size frequency distribution, where applicable. On Earth, maps of individual lava flow and chronology have been made in the context of risk assessment and predicting the location of future emplacements (e.g. Chevrel et al., 2021; Corradino et al., 2019; Smets et al., 2010). These works have in common that they focus on a set (or series of sets) of lava flows originating from the same source. This allows a study of the temporal evolution of their morphology, and in turn, their rheological properties, and could certainly be used on Mars.
Several chrono-stratigraphic geological maps of Mars have been constructed over the history of its exploration (e.g. Carr et al., 1973; Scott and Tanaka, 1986). As of 2023, Tanaka et al. (2014) remains the most up-to-date proposition of a global description of the stratigraphy of Mars (Fig. 1.1). However, large-scale maps suffer from a lack of spatial and temporal details. For instance, on the Tanaka et al. (2014) map, a single geological unit can be inferred as the "Amazonian-Hesperian Volcanic unit", which spans 3.7 billion years (Fig. 1.1). In addition, classical geological maps do not distinguish individual lava flows and usually combine them as one homogeneous unit.
More recent data provided by NASA *Mars Reconnaissance Orbiter* and its onboard cameras HiRISE (High Resolution Imaging System Experiment – McEwen et al., 2007) and CTX (Context Camera – Malin et al., 2007) have allowed for a more precise view of surface details. CTX and its near-global coverage have allowed for the creation of global mosaics at 6 m/px (Dickson et al., 2018). Such resolution therefore allows for a detailed mapping of individual lava flows similar to what is done on Earth.
In this thesis, a similar approach was used on Mars by attempting to reconstruct the chrono-stratigraphy of a set of lava flows at Arsia Mons, in Tharsis. A challenge has been to reconstruct the stratigraphy for hundreds of overlapping lava flows, which generates inextricable issues if a manual approach is used. Instead, I propose a streamlined approach to studying lava flows by combining classical geological mapping (see Chapter 2) and automatic procedures (see Chapter 3) to extract as much information as possible on the lava characteristics.

## 1.6 Morphometric analysis of small scale landforms

Although the chrono-stratigraphic map is adapted to the reconstruction of lava flow deposition, it is not adapted to the study of airfall deposits of explosive origin. Therefore, the landforms resulting from pyroclastic deposition, in particular aeolian bedforms, are studied following a different approach. Lava flows are extensive

and their study could be at the scale of the Arsia volcanic edifice; characterisation of pyroclastic features is best carried out at local scale. Regional scale investigations would face the issue of separating between airfall deposits of pyroclastic origin and sedimented dust, which is abundant at the surface throughout the Tharsis region (Ruff & Christensen, 2002). The pyroclastic deposits are studied at a local scale using high-resolution Digital Terrain Models (DTMs). The CTX and HiRISE cameras were not designed for stereoscopic image retrieval and processing; however, in some cases, the viewing parameters make it possible to identify stereo-pairs from different orbits and generate DTMs (see Chapter 2). CTX DTMs have a wider footprint at the surface but a lower vertical resolution than the HiRISE DTMs, which in turn have much higher precision but much smaller coverage. The *Colour and Stereo Surface Imaging System* (CaSSIS – Thomas et al., 2017) is an instrument launched on ESA *ExoMars Trace Gas Orbiter* (Vago et al., 2015) in 2016 and offers both colour images, with four filters, and stereo performances. CaSSIS images provide additional coverage with footprints intermediate between CTX and HiRISE. In this work, DTMs from the three cameras show that CaSSIS DTMs, although of pixel size an order larger than HiRISE pixel size, can yield similar vertical precision, making it possible to study the morphology and morphometry of the aeolian bedforms in great detail in much larger surface areas owing to their larger planetary surface coverage.

## 1.7 Objectives of this work

- Develop an integrated workflow to reconstruct the stratigraphy of lava flows and derive morphological parameters such as the length, width or the fractal dimension of their margins.
- Assess CaSSIS DTM performance and capability to study small-scale landforms and integrate this work into the analysis and interpretation of potential pyroclastic deposits.
- Apply these methods to lava flows and airfall (pyroclastic) deposits at Arsia Mons, a giant shield volcano of the Tharsis dome.

# Chapter 2

# Datasets and Methods

## Introduction

As of 2023, the only extraterrestrial planetary surface explored by humans is the Moon during the Apollo program (and hopefully soon followed by the Artemis program). For the rest, geological mapping and interpretation of the surface of an extraterrestrial planetary body can be achieved using remote sensing. Mars has been visited by more than 50 spacecraft since 1960, ranging from simple flybys to car-sized rovers operating for years at the surface and yielding terabytes of data. A plethora of dataset types exist and can used by planetary geologists to address scientific questions. In addition to the spectrum of different datasets from different missions, data can have several levels of processing stages. For instance, a high-resolution image of the surface at 25 cm per pixel was no more than compressed bits stored in the spacecraft memory before it was sent to Earth, reconstructed, calibrated, corrected and projected. Each of these steps requires time and not all datasets are available off-the-shelf, fully processed and ready to be used for science.

## 2.1 Datasets: visible and infrared imagery

### 2.1.1 CTX and HiRISE

Geological mapping and interpretation require images of the surface in order to identify the contacts between the various units, interpret the units and/or overall, understand how the landscape formed. Most of this work involves using data from NASA *Mars Reconnaissance Orbiter* (MRO – Zurek and Smrekar, 2007) launched in 2005, orbiting and imaging Mars since 2006. Onboard MRO, the *Context Camera* (CTX – Malin et al., 2007) can image the surface at 6 m/pixel and the *High-Resolution Imaging Science Experiment* (HiRISE – McEwen et al., 2007), down to 0.25 m/pixel.
The HiRISE finer resolution allows the description and study of smaller landforms. Calibrated HiRISE images can be downloaded directly from the HiRISE website in JP2 format and can be individually imported into a GIS software.
Whereas HiRISE has much better resolution, its footprint size is ultimately bottlenecked by data transfer rate and has therefore a limited coverage as opposed to

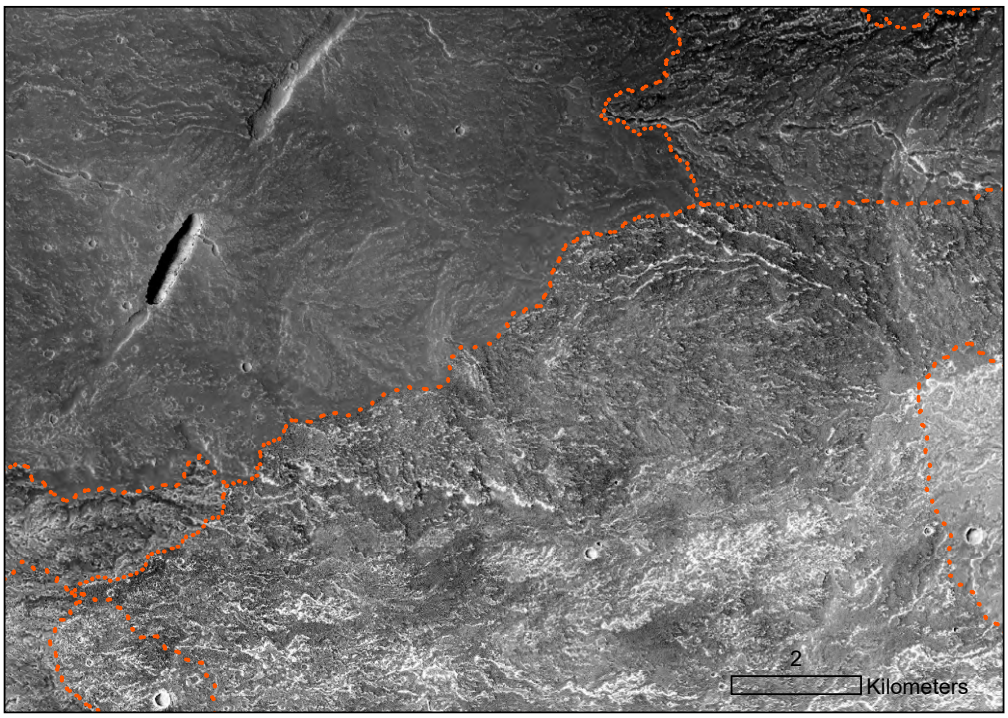


FIGURE 2.1: Example of seams between CTX images used for the Murray Lab Mosaic. The apparent change of albedo can be misleading for geological mapping.

CTX's nearly global coverage (below MRO latitude range of operation). For this reason, CTX images are often used as a base map e.g., geological mapping. With that in mind, Dickson et al. (2018) has constructed a seamless global CTX mosaic (referred to thereafter as the Murray Lab Mosaic) which can used by the community and is now available as a layer on the free planetary science-oriented GIS platform: JMARS (Christensen et al., 2009). The Murray Lab CTX mosaic is a convenient, fast and ready-to-use dataset. However, the seamless mosaicking method used is not perfect resulting in misleading apparent albedo variations which could be inferred as actual variations on the surface for an inadvertent user (Fig. 2.1). In addition, many observations display striping since each image is normalised along the columns to balance the tone laterally (Dickson et al., 2018).

For these reasons, I chose to generate CTX mosaics using the *Integrated Software for Imagers and Spectrometers* (ISIS – Gaddis et al., 1997; Sides et al., 2017) developed by the *United States Geological Survey* (USGS). ISIS offers a variety of tools to import, process and correct data from instruments flying on-board NASA and ESA missions. Almost all higher-level (i.e., already processed) datasets archived on NASA's *Planetary Data System* (PDS) or ESA's *Planetary Science Archive* (PSA) are processed using ISIS routines. ISIS also offers the possibility for any individual user to process manually low-level datasets into higher-level products for their specific use (e.g., creating mosaics).

CTX individual images were first selected using JMARS to check the overall coverage of the footprints as well as the quality of the images themselves. The Experimental Data Records (EDR) were downloaded from the NASA PDS Imaging Node and imported into ISIS to be converted into *.cub* format (cube - ISIS standard file type). The ancillary information related to the acquisition of an image, such as pointing, time, or position of the spacecraft, is stored in the SPICE (Spacecraft, Planet, Instrument, C-matrix, Events) kernels. This is a standard system used by all NASA and ESA missions which is used by ISIS to retrieve information about the observation and relate it to one data product. Once the SPICE kernels are retrieved, the individual CTX images can be calibrated the following way: first, the images are radiometrically calibrated using ISIS routine *ctxcal*. The *ctxevenodd* function is then called to remove detector stripping. At that stage, the images appear darker on the edges compared to the centre. This can be corrected by applying a column-wise normalisation on the cube using the *cubenorm* function. The normalisation, however, introduces a striping effect which in turn can be removed thanks to *dstripe* function. At this stage, the images are radiometrically calibrated, but they are not ready to be merged into a mosaic as they first need to be map-projected. As the geographic coordinates of the pixels are reconstructed solely from the pointing information stored in the SPICE kernels, misalignment issues can arise between images in overlapping areas. This can be improved by running a bundle adjustment between overlapping images to resolve the errors between the predicted image location and the actual location. In practice, this can be done with the *Ames Stereo Pipeline* (ASP - Beyer et al., 2018) tool called *bundle_ adjust* function, which is normally used on stereo pairs for Digital Terrain Model (DTM) generation (see section 2.1.4). In addition to pointing issues, co-registration issues can arise from different geometry of acquisition for each individual image, especially in regions of high topography variations. This can be mitigated by map projecting CTX images onto the global DTM derived from *Mars Orbiter Laser Altimeter* (MOLA - Smith et al., 2001), an instrument on NASA *Mars Global Surveyor* (Albee et al., 2001).

Once the data are radiometrically and geometrically calibrated, they are tone-matched using the ISIS *equalizer* function and seamlessly assembled using *noseam* function. Individual images are then merged into a single mosaic file and exported to tiff format.

### 2.1.2 CaSSIS

The *Colour and Stereo Surface Imaging System* (CaSSIS – Thomas et al., 2017) is an instrument launched on ESA *ExoMars Trace Gas Orbiter* (Vago et al., 2015) in 2016. The instrument can image the surface at 4.6 m/pixel and offer a higher signal-to-noise ratio than CTX. In addition, CaSSIS is equipped with four different filters that span different wavelength ranges: blue (BLU – 450 to 575 nm), panchromatic (PAN – 550 to 800 nm), red (RED – 775 to 900 nm) and near-infrared (NIR – 850 to 1100 nm)

filters. These allow CaSSIS images to highlight surface composition variations by combining the different colours (e.g. Tornabene et al., 2018).
During the completion of this work, I had the opportunity to participate in the CaSSIS acquisition of images cycle as a CaTL (CaSSIS Targeting Lead). CaSSIS target acquisition works by short-term planning periods (referred to as STP) corresponding to one week of imaging. Each CaTL usually plans 2 STPs in advance (more than a month). The potential targets are proposed by team members as well as other people in the scientific community. Those suggestions are uploaded on the *CaSSIS Suggestion Targeting* platform (CaST) and prioritised on a scale from 1 to 10 by a Science Theme Lead. Based on these suggestions and the orbiter trajectory, the CaTL can plan observations and adjust the parameters depending on the acquisition conditions and the data volume available.

### 2.1.3 Other Datasets

#### THEMIS

The *Thermal Emission Imaging System* (THEMIS - Christensen et al., 2004) is an instrument onboard the NASA *Mars Odyssey* mission. It can image in thermal infrared at 100 m/pixel and global mosaics from the day or the night side are available. Additionally, THEMIS-derived thermal inertia maps of the surface were created (Fergason et al., 2006) and can be used to distinguish between massive (i.e. rocky) and loose material.

#### HRSC

The *High Resolution Stereo Camera* (HRSC - Neukum and Jaumann, 2004) is an imaging system onboard the ESA *Mars Express* (Chicarro et al., 2004) that was launched in 2003. The instrument can image the surface of Mars with a stereo camera that provides up to 5 panchromatic multi-angle observations of the surface during each Mars orbit at a nominal ground resolution of up to 10 m/pixel. It can also acquire multi-spectral imagery using four CCD lines equipped with spectral filters (near-infrared, red, green, and blue). The stereo-capability allows for DTM reconstruction at 100 m/pixels.

### 2.1.4 Digital Terrain Models

#### CTX and HiRISE

Geomorphological characteristics of landforms can be efficiently derived with accurate elevation information provided by Digital Terrain Models (DTM, sometimes called Digital Elevation Models or DEM). On Mars, a global DTM was constructed using MOLA data at 463 m/pixel and ±3 m of vertical resolution (Smith et al., 2001). Despite its accurate vertical resolution, the study of small-scale features is limited by the horizontal resolution. Such study can however be achieved thanks to other

DTMs derived from stereo-pairs using photogrammetry methods (e.g. Muller et al., 2021; Putri et al., 2019). When two CTX or HiRISE images taken from different angles overlap each other, they can be used to create a high-resolution DTM. With *Ames Stereo Pipeline* (ASP – Beyer et al., 2018), I created CTX and HiRISE DTMs that were used for this work. The workflow used to produce DTMs is derived from the proposed integrated workflow from (Mayer & Kite, 2016).
The images are first imported into ISIS and calibrated following the same pipeline as described in section 2.1.1. A bundle adjustment is then run onto the stereo pair to adjust the pointing and improve the correlation during the next steps. To refine the result of the stereo correlation even further, the images can be mapped and projected onto an existing DTM such as HRSC DTMs. Alternatively, the images can be map projected using the *cam2map4stereo.py* routine of ASP. The map projected products can be parsed through *parallel_ stereo* to create a 3D mesh that can be converted into a DTM. To improve the final result, (Mayer & Kite, 2016) proposed that this first generated DTM can be used to map project the stereo pair images onto itself to create a final high-resolution DTM. This can be done by using a different stereo algorithm that increases the matching in relatively flat and smooth areas but produces coarser results. The 3D mesh is aligned to MOLA data before being converted to a DTM in tiff format.

#### CaSSIS

The CaSSIS DTMs used during this work were first produced at the Italian National Institute for Astrophysics (INAF), in Padua, using the 3DPD pipeline described by Re et al. (2022). They were further refined by Dr. Sylvain Douté (IPAG, CNRS-Université Grenoble Alpes, France) using the photoclinometry method "HDEM" (Doute and Jiang, 2020; Jiang et al., 2017). HDEM adds fine-scale 3D information on the photogrammetrically generated initial CaSSIS DTMs at an effective resolution of 13.8 m/pixel from the corresponding ortho-image at 4.6m/pixel. HDEM SfS takes the two products and iteratively refines the coarse input DTM via minimisation of a total cost function that integrates an intensity model of the image based on a novel radiative transfer scheme and two regularisation terms. The image model is built according to the geometrical acquisition conditions of the orthoimage and assumes a homogeneous bidirectional reflectance throughout the scene taken as the Martian standard photometric function of Vincendon (2013). The HDEM algorithm operates at horizontal scales of meters to hectometres. The vertical relative accuracy has been estimated to lower than 1 m, based on the level of morphological detail achieved and previous numerical tests (Doute & Jiang, 2020).

## 2.2 Impact Crater Retention Ages

Apart from meteorites, we do not have any samples coming from Mars. Therefore, inferring the absolute age of formation of a given terrain is virtually impossible.

Fortunately, during the Apollo missions, hundreds of kilograms of rock samples were collected. The radio-isotopic ages of these samples were matched to the impact crater density visible at the surface of the Moon. From there, impact crater density models were built and it is now possible to infer the absolute age of the surface of a planetary body with a certain degree of certainty. Thus, the Crater Counting Analysis (also known as Crater Size Frequency Distribution – CSFD) method is the most common technique to retrieve absolute chronological information in planetary geology mapping with remote sensing.

In this thesis, CSFD are used on several occasions to date the surfaces. As impact crater retention age requires a precise definition of the area that one wants to date, the geological mapping of individual lava flows as discrete and homogeneous surfaces of potentially different ages is used. To obtain accurate results, this method requires the area to be large enough in order to retain enough impact craters to have a statistically realistic CSFD. The craters were mapped as circles and stored in a single shapefile. I then imported the shapefiles containing the impact craters as well as the lava flows into *CSFD Tool* (Riedel et al., 2018), and generated a *.scc* file containing statistics for each selected area. This file can be imported into the *CraterStats 2.0* software developed by Michael and Neukum (2010) in order to plot the crater density against diameter. All plots were represented in differential crater density, fitted with a Poisson distribution and used the (Hartmann & Daubar, 2017a) production function.

# Chapter 3

# Automatic Reconstruction Of Morphometry and Stratigraphy (AROMAS)

## Introduction

The mapping and interpretation of hundreds of individual lava flows can be a time and energy-consuming effort. As of 2023, the use of neural networks and deep learning methods to detect geomorphological features on planetary surfaces thanks to high-resolution datasets have shown promising results (e.g. Bickel et al., 2020, Lee, 2019, Silburt et al., 2019). While these recent efforts have been successful at detecting features such as impact craters or rockfalls, or in land classification (e.g. Kussul et al., 2017), automated mapping of geological units and geological map reconstruction appears to be still a distant goal.
AROMAS is an automated workflow developed in Python 3 that can be used to produce a geological map of any number of individual lava flows from digitised contacts, and infer their morphological characteristics such as length, width and even thickness if elevation data is provided. The philosophy of AROMAS is to propose a flexible, efficient and harmonised method to map lava flows on planetary surfaces and produce a stratigraphic map. The overall workflow uses a shapefile containing digitised contacts between the different lava flows as input and produces a new shapefile with a polygon corresponding to the extent of individual lava flows. The attribute table of this output contains information about the stratigraphy, the apparent and inferred length and width, the average thickness of the flow (if a DTM is available) as well as the fractal dimensions of its margin if applicable.

## 3.1 Pre-requirements: Lava flow contact mapping

In order for AROMAS to determine the stratigraphy of the different units, the contact lines have to be digitised in a particular way. Once the area is selected, the data are prepared and the scale of the map is chosen, the user can start mapping the contact between the different lava flows. When a contact between two lava flows is

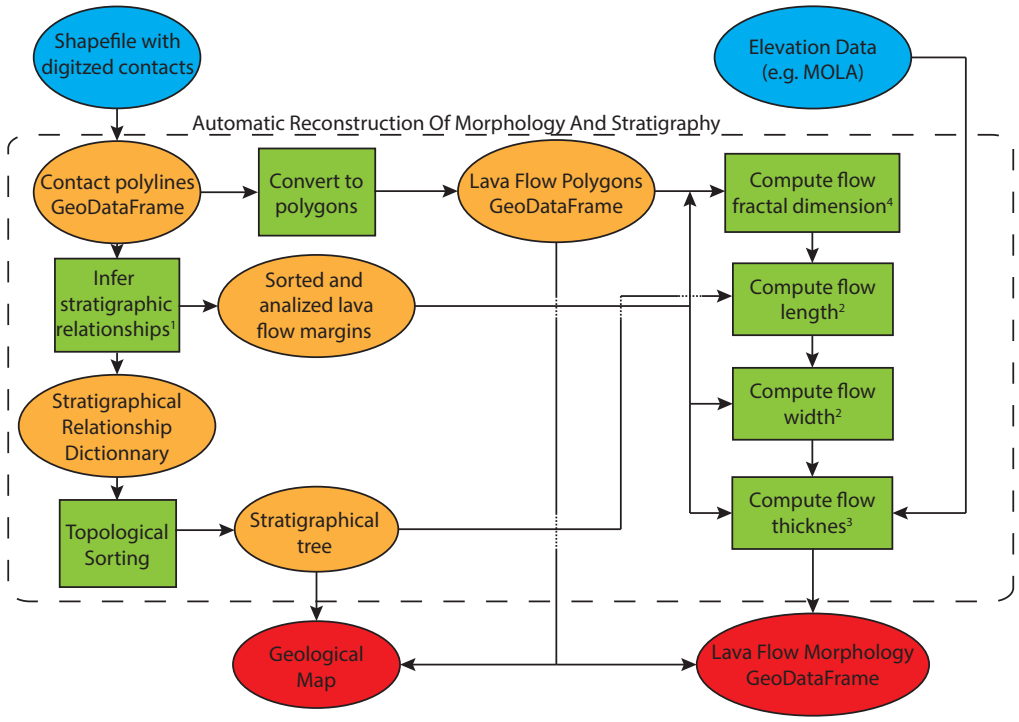


FIGURE 3.1: General workflow of the AROMAS routine with reference to other subroutines. **1**: see section 3.3 and Fig. 3.2. **2**: see section 3.4.2 and 3.4.4, and Fig. 3.6. **3**: see section 3.4.5 and Fig. 3.8. **4**: see section 3.5.2 and Fig. 3.9. Key: Blue ellipse: input; Orange ellipse: Temporary variable; Green rectangle: function; Green polygon: condition; Red ellipse: output.

identified, the overlapping relationship between the two units is interpreted by the user.

When broken down, a polyline is essentially a list of vertices with coordinates. AROMAS uses the order of vertices in this list (i.e. a first and a last vertex), which depends on which order the user was digitising the polyline. Since there are only two possible line orientations, the overlapping or overlapped information can be stored using this polyline property. In practice, the user can either map a lava flow boundary clockwise or anti-clockwise with respect to the flow centre. Each boundary is therefore mapped one way or the other depending on the interpreted overlapping relationship with the lava flow neighbours. This is the most important step of the whole workflow, from the mapper's point of view, since any interpretation done at this step has consequences on almost every automated process further down.

## 3.2 AROMAS: General workflow

The general structure of the AROMAS workflow is summarised in Fig. 3.1. The code was written in Python 3 and mainly uses the *GeoPandas* library (Jordahl et al., 2020) to import and store shapefiles. A GeoPandas Data Frame (or GeoDataFrame) is a variable that stores geometry objects using the *Shapely* library (Gillies et al., 2023)

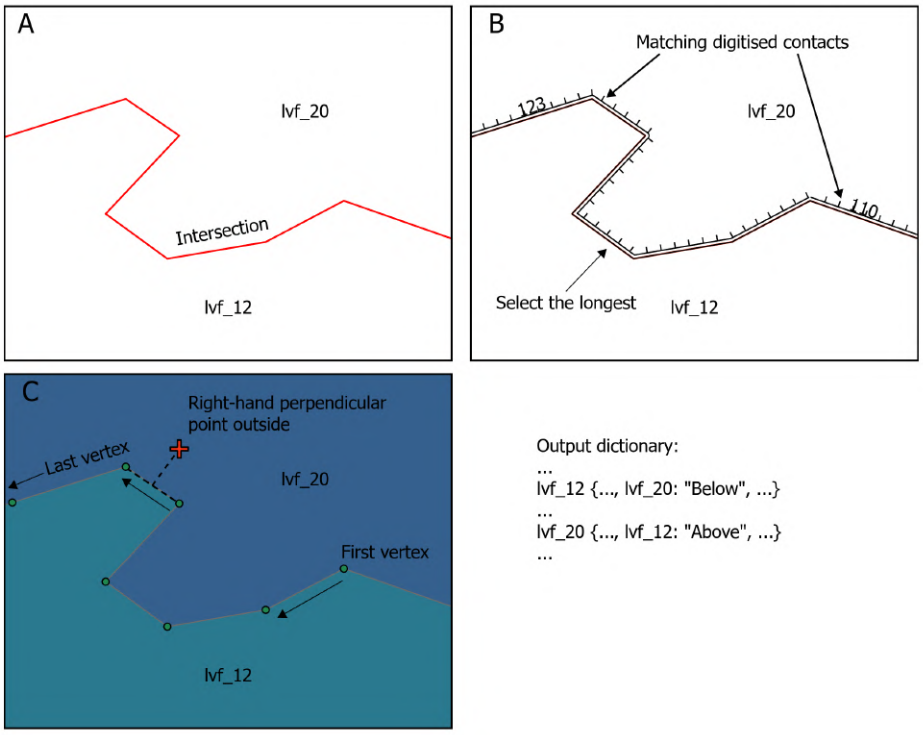


FIGURE 3.2: Illustration on how AROMAS infers the stratigraphic relationship between two units based on the digitised contact polylines. **A**: The intersection between the current lava flow and a neighbour is generated. **B**: The corresponding contact lines are selected. Here two contacts match the intersection line (nr. 123 and 110). 123 is retained as it is the longest one and thus the most representative. **C**: Vertices of contact line 123 are extracted and the right-hand perpendicular point is generated around the middle of the polyline. This point is located outside lvf_12 meaning the latter overlaps lvf_20. Lastly, the information is stored in the relationship dictionary.

alongside attribute information similar to a shapefile. The *Shapely* also allows manipulation of polylines, polygons and points, and is used frequently in AROMAS to perform operations on geometry objects. The main code is available in the Appendix A.

The polylines in ESRI shapefile format ("ESRI Shapefile Technical Description", 1998) are first imported into a GeoDataFrame variable and polygons are generated from it using the *ArcPy* function *Feature to Polygon*. The *ArcPy* library is not open-source and requires an ArcGIS license. Future versions of AROMAS will aim to replace this step with functions from an open-source package such as *Shapely*. The newly created polygons corresponding to individual lava flows are stored in another GeoDataFrame with a dedicated label for each of them.

## 3.3 Stratigraphic reconstruction

### 3.3.1 Contact analysis

The first major step of the workflow consists of inferring the stratigraphic relationship between a lava flow and its direct neighbours. For each polygon (i.e. lava flow),

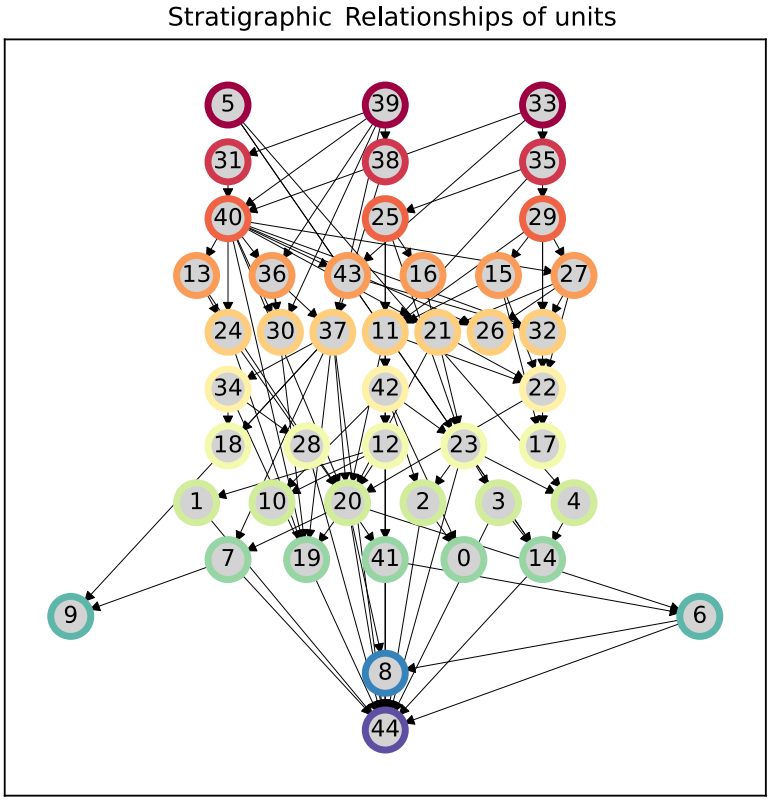


FIGURE 3.3: Output example of stratigraphic tree automatically generated by AROMAS. Nodes at the top represent the stratigraphically youngest units.

the neighbouring units are first selected and iterated. For each of these neighbouring polygons, an intersection polyline is generated and used to select the corresponding digitised contact that matches this intersection (Fig. 3.2). If several contact polylines match the intersection, the longest one is kept (i.e. the most representative contact). With this contact, starting from its first vertex, a new point is generated at 90 degrees to the right of the polyline. If that point falls into the main polygon, it means the contact was drawn anticlockwise with respect to the unit, therefore its neighbouring unit is overlapping it. On the contrary, if the main unit is a lava flow overlapping its surroundings, the contact line was drawn clockwise and this test will generate a point that falls within the neighbouring unit (Fig. 3.2). Once this test is performed, the new overlapping information is stored in a dictionary which contains one entry per polygon which contains a list of its neighbouring units and their respective relationships (Fig. 3.2). Functions related to stratigraphic relationships are provided in Appendix B.

### 3.3.2 Output: Stratigraphic tree and map

From the dictionary, a directed graph (digraph) is generated using the *NetworkX* package (Ladd et al., 2017). In this digraph, each node corresponds to a lava flow.

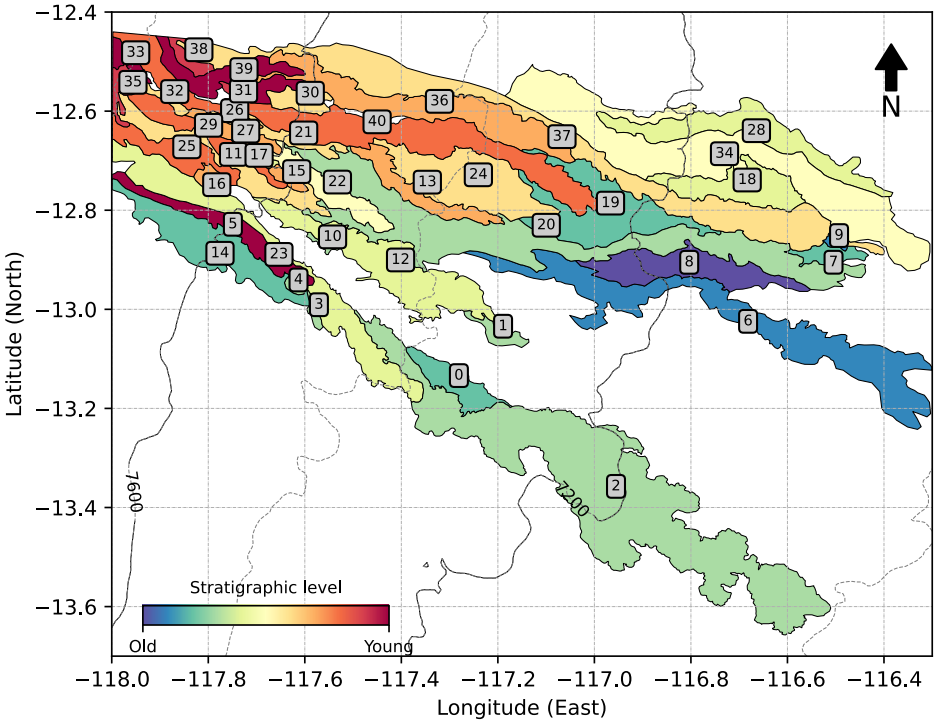


FIGURE 3.4: Output example of geological map automatically generated by AROMAS.

The digraph is parsed through a test that assesses if it is cyclic or acyclic. Cycles indicate that there are nodes connected with each other, forming a loop and indicating an error of interpretation during the mapping. For instance, a unit A which overlaps a unit B, which in turn overlaps unit C, which overlaps unit A, is a loop and the resulting digraph is cyclic. The user is then invited to either fix the contacts stored in the input shapefile and recreate a new dictionary, or to edit the dictionary manually. The acyclic digraph is then stratified and converted into a topological generation node collection. During the conversion, the number of stratigraphic layers is retained and, for each node, the corresponding layer number is stored in a new dictionary. The final network with the corresponding colour for each layer can be plotted (Fig. 3.3). The layer dictionary and the original GeoDataFrame containing polygons are merged and exported into a single shapefile which contains a column with the stratigraphic level. Alternatively, the GeoDataFrame can be plotted to display a geological map with colours corresponding to the stratigraphic level (Fig. 3.4). If a DTM is provided as an input (e.g. MOLA Global DTM), the topographic contours can be generated and included on the map.

## 3.4 Morphometrics of Lava Flows

### 3.4.1 Introduction

Once the stratigraphic relationships between lava flows are inferred, AROMAS can compute their morphological characteristics, i.e. their length, width and thickness.

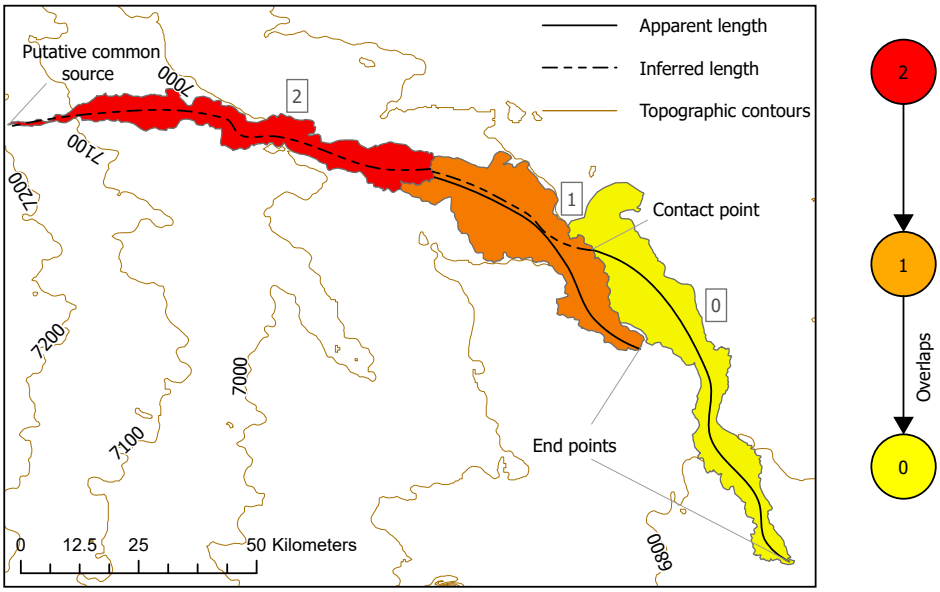


FIGURE 3.5: Example of a set of lava flows with a common source and their computed apparent and inferred length.

Here, lava flow length is considered to be the distance along the flow between the potential source and the tip of the lobe. An issue arising from such a definition is that lava flows are often covered by more recent ones. In that case, only a portion of the flow is visible, and the length measure does not correspond to reality anymore. The issue of overlapping flows does not only affect flow length, but also width. For instance, a flow margin could be exposed on one side but not the other, therefore the total width extent cannot be measured. In practice, while performing lava flow measurements manually, a trained eye would only attempt to retrieve flow morphometrics on exposed parts. Here, the stratigraphic tree generated by AROMAS is used to automatically compute, where applicable, the flow apparent length, and average width. Additionally, using the relationships between the different units, the so-called "inferred length" is reconstructed by merging the apparent length with a path to a potential source automatically. All the functions developed for length and width are provided in Appendix C.

### 3.4.2 Apparent and inferred length

Fig. 3.5 shows an example of three lava flows where their stratigraphy was reconstructed following the previous steps. A stratigraphic tree was also generated showing the relationships between these units. Their apparent and inferred length were generated following the workflow described in Fig. 3.6. For each flow, a path to the highest node (i.e. the uppermost flow, therefore the one directly connected to the potential source) is first constructed using the stratigraphic tree generated prior. Since several paths to several highest nodes can exist, the shortest path only is retained

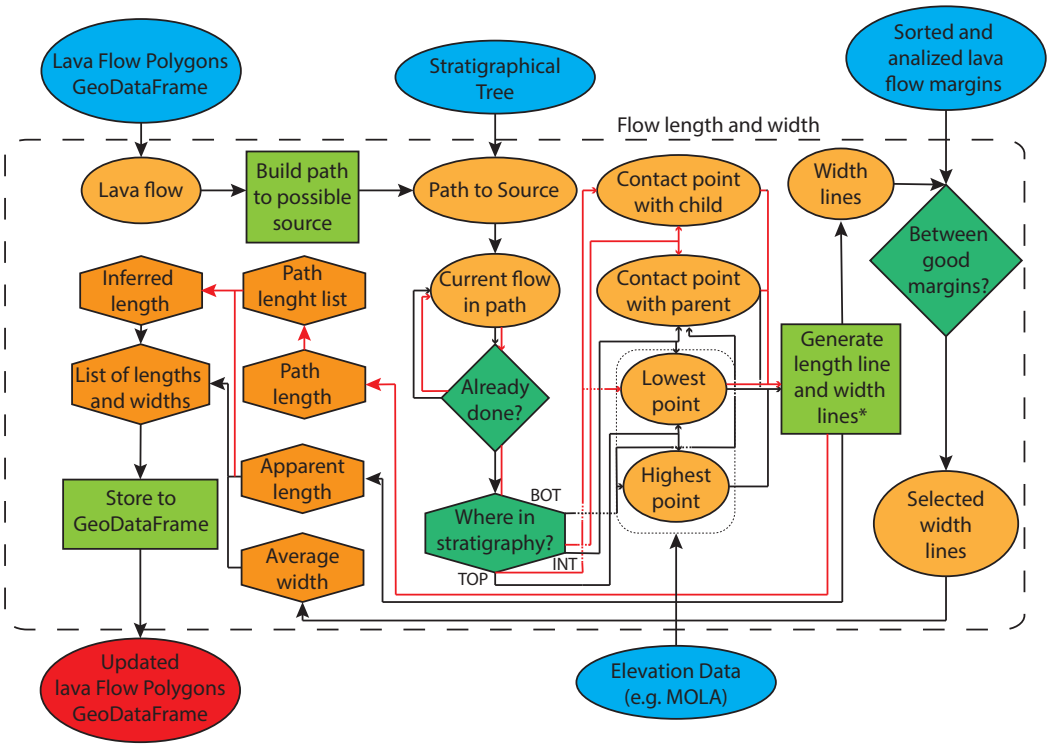


FIGURE 3.6: Workflow to compute the apparent and inferred length.*See 3.7. Key: Blue ellipse: input; Orange ellipse: Temporary variable; Orange polygon: temporary numerical variable; Green rectangle: function; Green polygon: condition; Red ellipse: output. The black arrows show the workflow to compute the apparent length whereas the red arrows show specific workflow to calculate the inferred length.

with *shortest_ path* function from the *NetworkX* package (see Ladd et al., 2017). In practice, it connects the current flow to the closest highest flow and, most likely, the source.

From here, each flow in the newly generated path is iterated twice in a subroutine which computes the apparent and the inferred length. The flow's label is first compared to a variable containing the list of flows for which either apparent or inferred length was already measured, to avoid computing twice the same value for one flow. Now, depending on whether the flow is located at the top, the bottom or at an intermediate level in the stratigraphy, the calculation of its apparent length will vary. The function that computes length and width needs two points as input. For instance, the apparent length of a flow located at the top is measured between its highest and lowest vertex, whereas the length of a flow located at the bottom is measured between the contact point between the current flow and its direct parent flow (in the path) and its lowest vertex. Selecting the lowest point thus measures the length of the longest path of a multi-branched flow. The so-called "height" of a vertex is measured by interpolating the elevation from a DTM with the polygon vertices.

Computing the inferred length requires first calculating the apparent length and adding it to the sum of the "path lengths" of each flow above it in the path. The path length corresponds to the distance between the contact point of the current

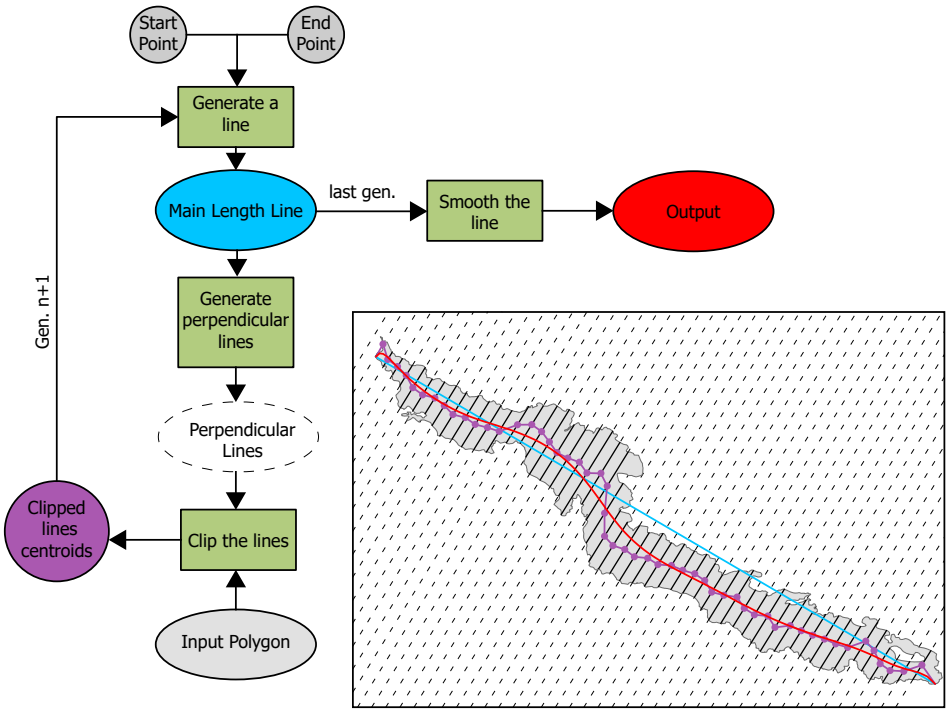


FIGURE 3.7: Workflow of the function measuring the length and width of a polygon between two points.

flow with its child and the contact with its parent. For a flow located at the top, the path length then corresponds to the distance between the highest vertex (i.e. the source) and the contact with its child. A flow located at the bottom has no child, therefore computing its path length is not necessary.

### 3.4.3 Polygon length and width function

The function used to calculate the length uses a *Shapely* polygon corresponding to the lava flow, a start and an endpoint. Before applying the function, the start and end points need to be selected among the polygon vertices (see section 3.4.2). The selected points can be parsed into a function that will first generate a straight line between these two points (Fig. 3.7). Along the main line, evenly spaced perpendicular lines are generated every 100 m from the start to the end of the main line. These perpendicular lines extend beyond the polygon on each side and are then clipped to match its extent. Using the centroids of these perpendicular lines, a new main line is generated that connects the start point, the centroids and the endpoint. The function can be called over several iterations to obtain improved results, however, experience showed that a maximum of 2 or 3 iterations, depending on the complexity of the lava shape is usually enough to obtain a satisfying result. In order to, obtain a smooth line, a subroutine is called to simplify the line creating Bézier curves using De Casteljau's algorithm (Boehm and Müller, 1999). The function then outputs

a Shapely geometry object corresponding to the length line and a list of geometry objects corresponding to the width lines.

### 3.4.4 Average width

So far, it has been seen that computation of the flow length requires the generation of perpendicular lines along it. At first glance, these lines may correspond to the flow width but as was discussed in the introduction, lava flows often overlap. A correct measurement of width therefore corresponds to the distance between non-overlapped margins. One of the initial steps of AROMAS consists of building a dictionary of relationships between lava flows. The dictionary can then be used to create a list of "good" margins (i.e. non-overlapped) for each lava flow and use this list to measure the width of these flows.
To create such a list, we iterate the flows in the dictionary and create a margin where the relationship with a neighbour is "below" for a given flow. The list is then simplified by merging the good margins end-to-end. These margins are stored in the GeoDataFrame to associate each flow with its list of good margins. Flows that are completely overlapped therefore have no margins, and the width cannot be computed.
Using this list of good margins for each flow, once the length is computed, we can retain only the width lines that are located between two good margins (Fig. 3.6). From here, individual width lines can be stored as geometry objects in the DataFrame and the average width (i.e. the average length of the width lines) as well as the standard deviation can be calculated.

### 3.4.5 Average thickness

Measuring the thickness of a lava flow faces the same challenges as the width and length measurements: it can be performed only where the margins are exposed. Using the same list of "good" margins generated for the lava flow width one can attempt to retrieve the thickness of a flow at that margin.
On Mars, MOLA data are also available as shots corresponding to measurement points of elevation along MGS orbits. Using these points as input and selecting the ones around each margin, the flow local thickness can be calculated for each crossing orbit (Fig. 3.8). The local thickness is inferred by calculating the elevation difference between the highest and the lowest MOLA point within 500 m of the margin.
Similarly to lava flow width, each thickness measurement can be retained and/or the average thickness can be calculated for each lava flow and stored into the GeoDataFrame. The function used to prepare the MOLA data and calculate the average thickness is provided in Appendix D.

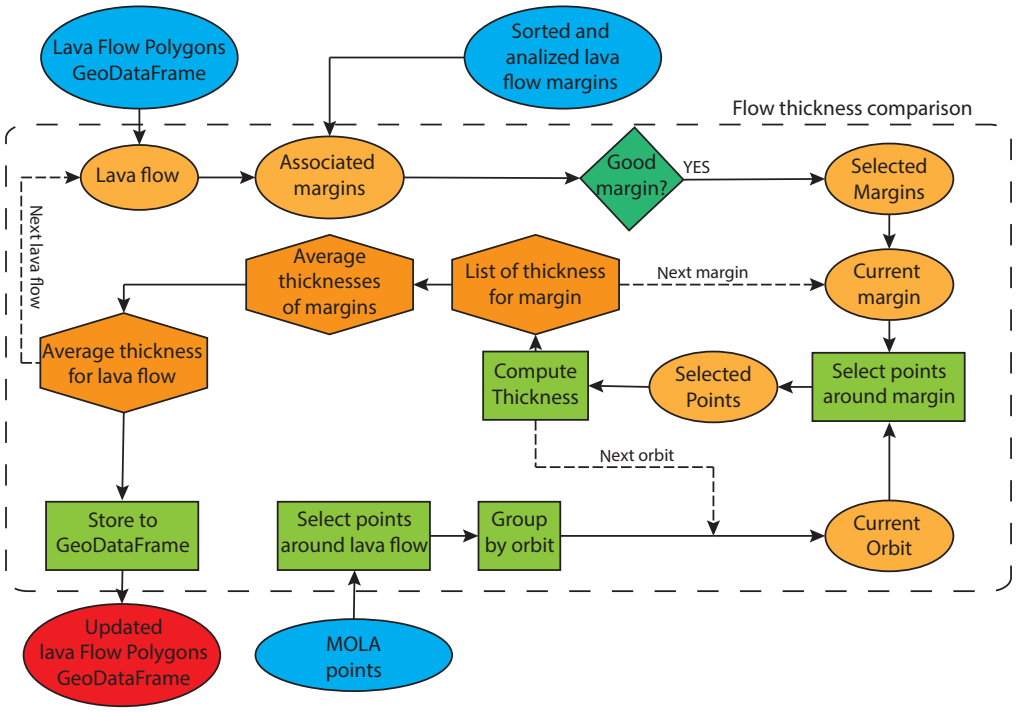


FIGURE 3.8: Workflow to compute the average thickness. Key: Blue ellipse: input; Orange ellipse: Temporary variable; Orange polygon: temporary numerical variable; Green rectangle: function; Green polygon: condition; Red ellipse: output.

## 3.5 Fractal dimension of margins

### 3.5.1 Terrestrial lava flows and field method

In addition to length, width and thickness, AROMAS is also used to compute the fractal dimension of lava flow margins. As pointed out by Bruno et al. (1992), lava flows are fractal and their fractal dimension (i.e. their index of complexity) can be used to discriminate between ‘a‘ā and pāhoehoe flows (Bruno et al., 1992, 1994). The original method consisted of using rods of different lengths ($r$) and performing a so-called "structured walk" along the flow margin to infer how many rods of each length ($N$) are necessary to approximate the total margin length $L = Nr$ (Bruno et al., 1992). $L$ can then be plotted against $r$ in a log-log plot, known as a Richardson plot from (L. F. Richardson, 1961). A linear fit on the Richardson plot can then be used to assess whether the margins are fractal and their fractal dimension $D$. The fractal dimension corresponds to $1 - m$, where $m$ is the slope of the linear fit inferred in the previous step.

### 3.5.2 Remote sensing workflow

Similar to width and thickness computations, the list of good margins can be used to calculate, where applicable, the flow fractal dimension. For each margin, the field

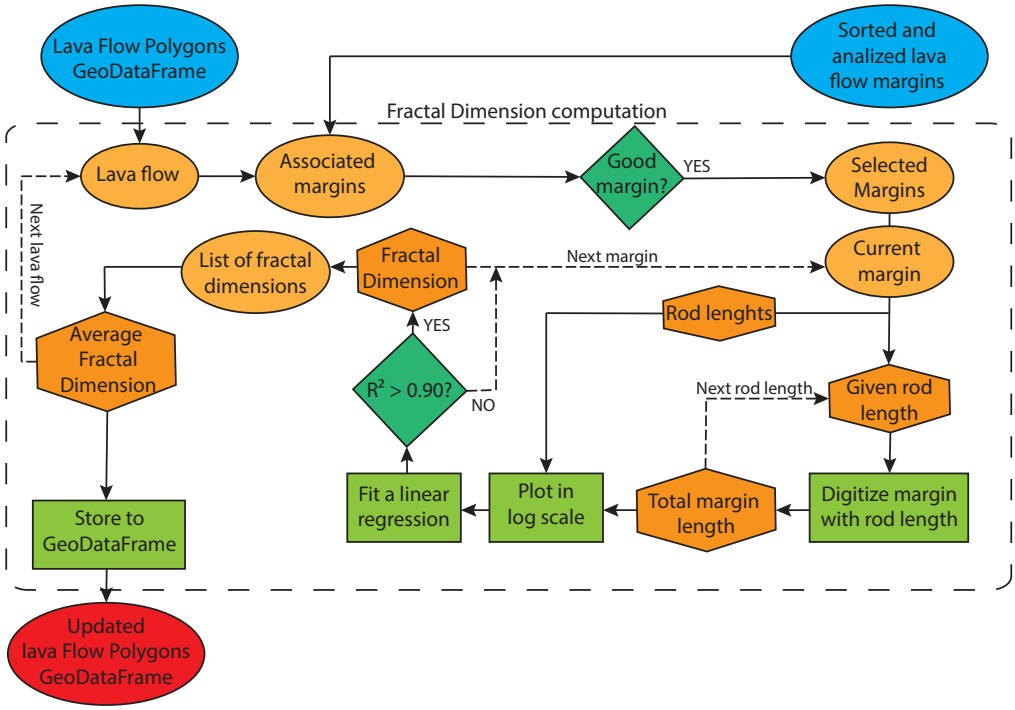


FIGURE 3.9: Workflow to compute the average fractal dimension. Key: Blue ellipse: input; Orange ellipse: Temporary variable; Orange polygon: temporary numerical variable; Green rectangle: function; Green polygon: condition; Red ellipse: output.

technique can be replicated by automatically re-digitising the margin using a specific rod length (Fig. 3.9). The number and value of rod lengths can be specified by the user. Starting from the first vertex, the script searches the closest next vertex located $x$ metres away, where $x$ is a given rod length. The operation is repeated from the newly found vertex, and so on, until the end of the margin is reached. These vertices are stored and used to create a "lower resolution" margin related to a specific rod length. The total length of each new margin is then computed. From here, the Richardson plot can be created and linear regression is performed on the plot. If the correlation coefficient is above 0.9, then the margin is considered fractal and the fractal dimension is calculated (i.e. $1 - m$). If a lava flow has several "good" margins, the average fractal dimension is calculated. The list of functions used for fractal dimension computation is provided in Appendix E.

## 3.6 Manual vs Automated

### 3.6.1 Introduction

To compare the results obtained through the AROMAS workflow and manually obtained results, a test was performed on a lava flow sample located in the Tharsis region south of Arsia Mons (Fig. X). The lava flow contacts were mapped using the workflow described in section 3.1. The mapping was done over a CTX mosaic at

a 1:50,000 scale. Lava flow apparent and inferred length were measured manually by digitising polylines following the approach described in section 3.7. Flow width was measured the same way on a sub-sample where applicable. The lava flow thickness and fractal dimension were not retrieved manually as the method used would strictly follow the workflow that AROMAS uses. Strictly similar results would be expected.

### 3.6.2 Results

Comparison between manual measurements and results obtained by AROMAS are reported in Fig. 3.10. Apparent lengths yielded by AROMAS are on average 1.46 km shorter than lengths measured manually. Similarly, inferred lengths are 4.72 km shorter when computed automatically compared to manually. The width of lava flows calculated by AROMAS is on average 0.26 km shorter than the widths measured manually. Overall, the mean difference between automatic and manual measurements is around 10%.

### 3.6.3 Discussion

Automatic measurements of lava flow morphometrics are, on average, shorter than classical manual measurements. For the length, this main difference could be explained by the lack of the "smoothing" step done by AROMAS in the manually digitised polylines (see section 3.4.3). A curved line would, on average, decrease the total length of the line by drawing a shorter path along the flow. This difference, however, would not explain the lower values obtained for width measurements. Another explanation may come from how these width lines are generated with both approaches. In AROMAS, width lines are constructed alongside length lines, perpendicular to the flow direction. In contrast, manual width lines are digitised independent of the length and may have a slightly different angle with respect to the flow direction. As sections of the flow drawn not perpendicularly with respect to the flow axis have higher lengths than perpendicular ones, this may explain the differences observed in average width between manual and automatic approaches.
The differences obtained by manual and automatic methods cannot be considered as errors, which would imply that either the manual or the automatic measurements represent the true morphometric characteristics of the lava flows. The two measuring approaches rather reflect different definitions of length and width, which as discussed above, are not unique in the case of complex surface areas such as lava flows. The 10% average difference between the two methods is therefore an acceptable result to confidently use AROMAS to retrieve lava flow morphometrics.

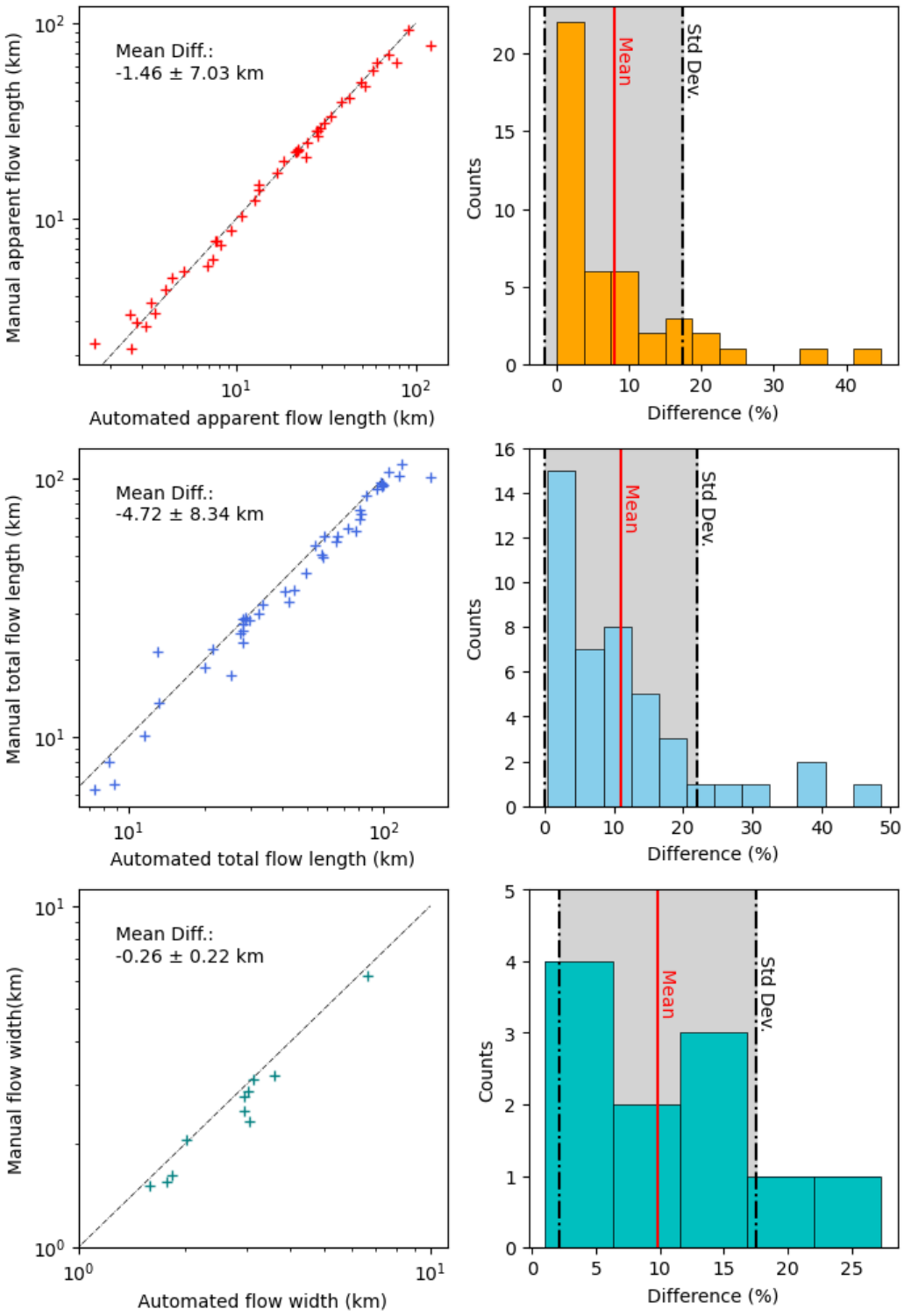


FIGURE 3.10: Comparison of results obtained through manual and automatic measurement of apparent length, inferred length and width. Left: Direct comparison in logarithmic scale. Right: Absolute difference between the two measurements is divided by the average of both, in percent.

# Chapter 4

# Lava flows south-east of Arsia Mons

## 4.1 Introduction and context

The goal is now to apply AROMAS on a set of lava flows southwest of Arsia Mons well visible in the THEMIS Day IR imagery and that appears to originate from the southern lava apron, located to the west of the area (Fig. 4.1). Other sets could be suitable but, more to the north, may be interfered with by other emplacements coming from Pavonis Mons, and, to the west, glacier deposits (Head & Marchant, 2003; Scanlon et al., 2015) overlap any recent lava flows. Therefore, the southeast of Arsia is an ideal place to study a set of recent lava flows. The area selected for geological mapping is located southeast of Arsia Mons and extends over a 250 by 450 km surface area.

## 4.2 Mapping

### 4.2.1 Data and methods

The datasets and methods used to carry out geological mapping are described in Chapter 2. Custom CTX mosaics were built to cover the full extent of the investigated area and imported into ArcGIS Pro. Lava flow contacts were digitised following the workflow described in Chapter 3 to allow implementation into the AROMAS pipeline. All the shapefiles were projected in an Equirectangular projection given the proximity to the equator, to avoid distortion on distance measurements. All the contacts were mapped quadrangle by quadrangle of 1x1 degree of size, with special care on ensuring continuity between two quadrangles. In addition to lava flows, other features were mapped such as channels, faults, and collapse pit rims.
In the areas that were selected for impact crater counting, craters were counted until the minimum diameter of 50 m.

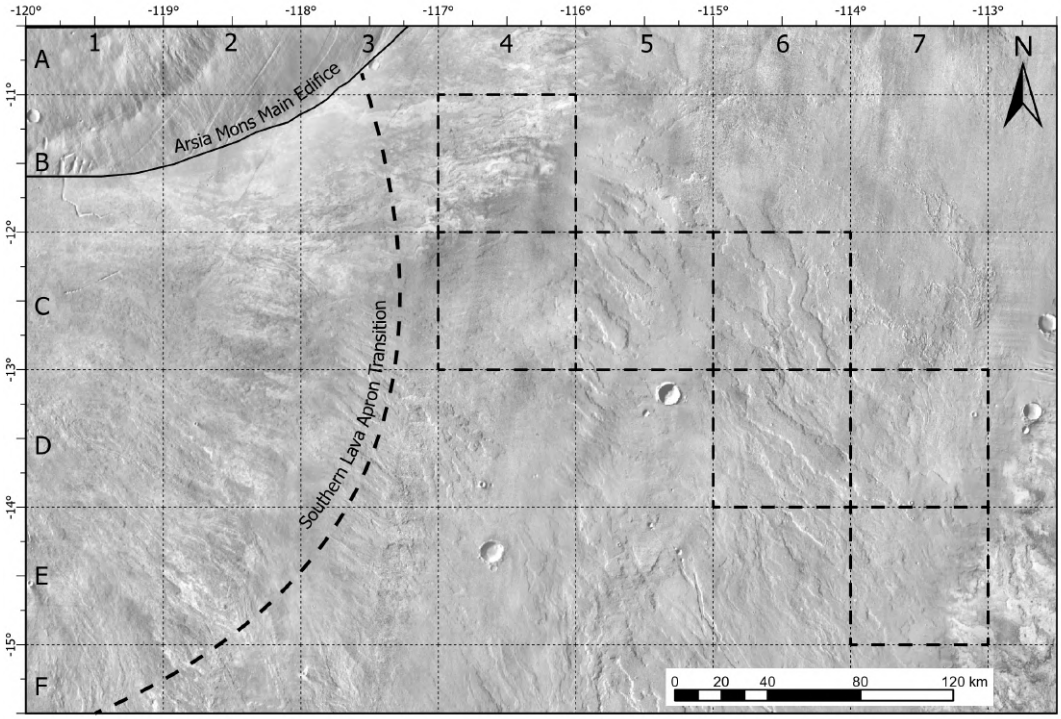


FIGURE 4.1: Location of the set of lava flows mapped, southeast of Arsia Mons, at the foot of the main edifice and the southern lava apron. The flows are well-visible on THEMIS Day-IR data (100 m/ ppx. A 1x1 grid was constructed and used for mapping. Quadrangles with bold dash-lines received the main focus and individual maps can be found in Fig. 4.4 to Fig. 4.10)

### 4.2.2 Symbology

Since the focus of this work is to attempt a chronological reconstruction of different lava flow emplacement episodes, the geological mapping of individual flows needs to include the stratigraphic relationships of the different flows. Conventional geological mapping of lava flow contacts includes making distinct geologic contacts which are either observed, masked or inferred. In order for the maps to report the horizontal relationships between the different units and provide a vertical dimension, a specific symbology was used to indicate the flow's overlapping relationship with its surroundings. In tectonics, mapping symbols often indicate fault scarp orientation with a perpendicular stroke along the line symbol. A similar logic was adopted for mapping the Arsia Mons lava flow contacts. A double-stroke line was drawn at lava flow contacts, combined with a perpendicular stroke that points to the lava flow scarp direction. This symbology emphasises the overlapping relationships between lava flows and their surroundings. In order to ensure that the symbols are correctly oriented, the polylines are drawn clockwise with respect to the overlapping unit. This makes it possible for AROMAS to reconstruct the comprehensive lava flow stratigraphy (see chapter 3). The contact between two units sometimes does not display a scarp as their margins may be bounded or even overlapped by another flow. Such contacts are mapped using a single-stroke line. Unclear contacts

are mapped with their dashed equivalent of sharp contacts and inferred contacts have a question mark between the dash lines. There is no symbol for "inferred lava scarp" as the scarp is an observation and not an interpretation. Therefore, such a symbol would not make sense.

## 4.3 Results

### 4.3.1 Geological Maps

Fig. 4.2 provides a comprehensive map of lava flow contacts and flow linear patterns. The selected quadrangles are those displaying the largest number of contacts. The lava flow contacts were parsed through the AROMAS pipeline to generate units and classify them based on their inferred stratigraphic relationships. In total, 424 individual lava flows were identified and classified by AROMAS. These units are reported in Fig. 4.3 or for each 1 degree quadrangle in Fig. 4.4, 4.5, 4.6, 4.7, 4.8, 4.9. and 4.10.

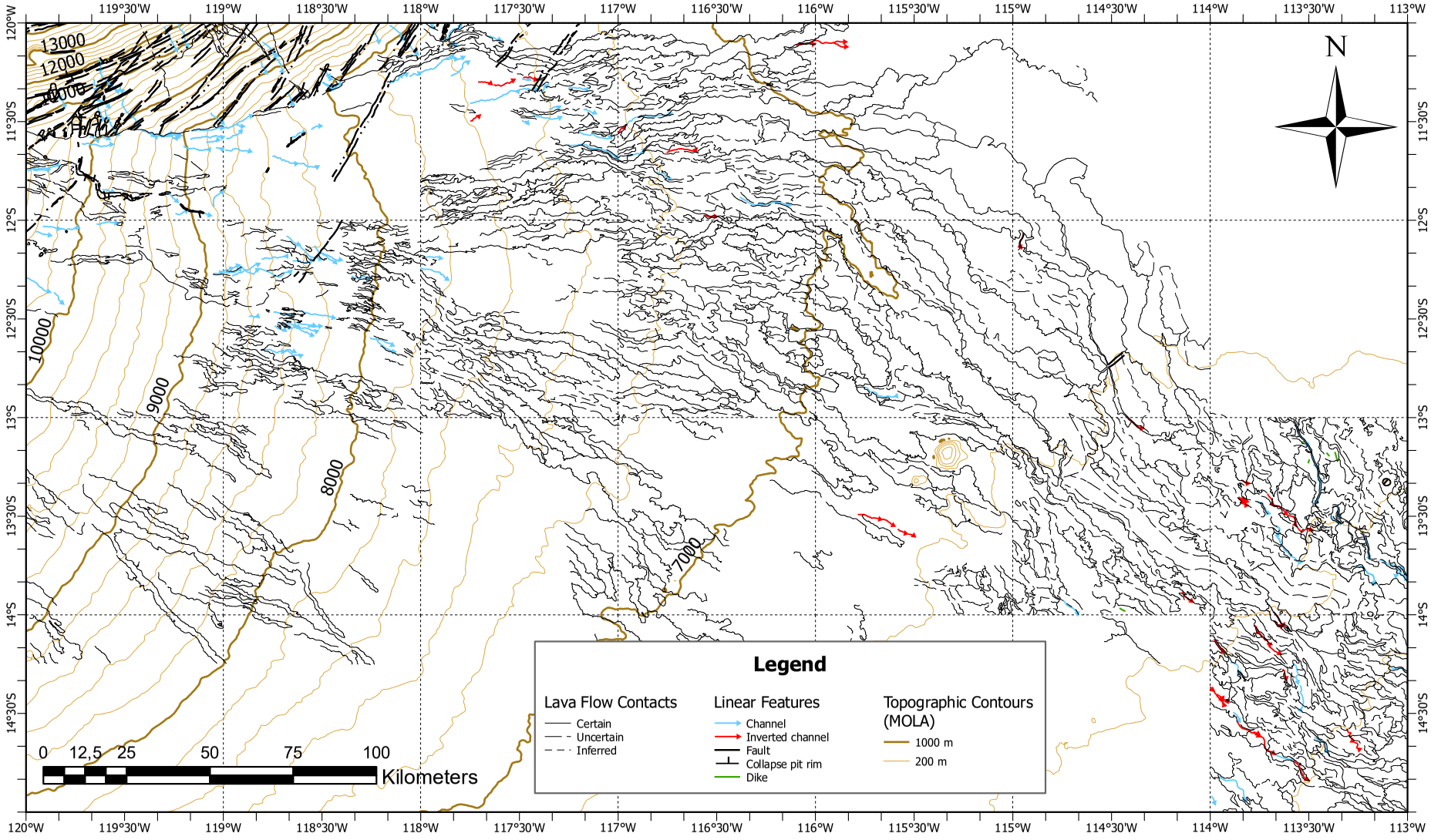


FIGURE 4.2: General map of lava flow contacts and other linear patterns which were manually digitised during this work. Here, a lighter symbology is used to simplify the map visualisation. Close-up maps reported in Fig. 4.4 to Fig. 4.10 use the specific symbology described in section 4.2.2.

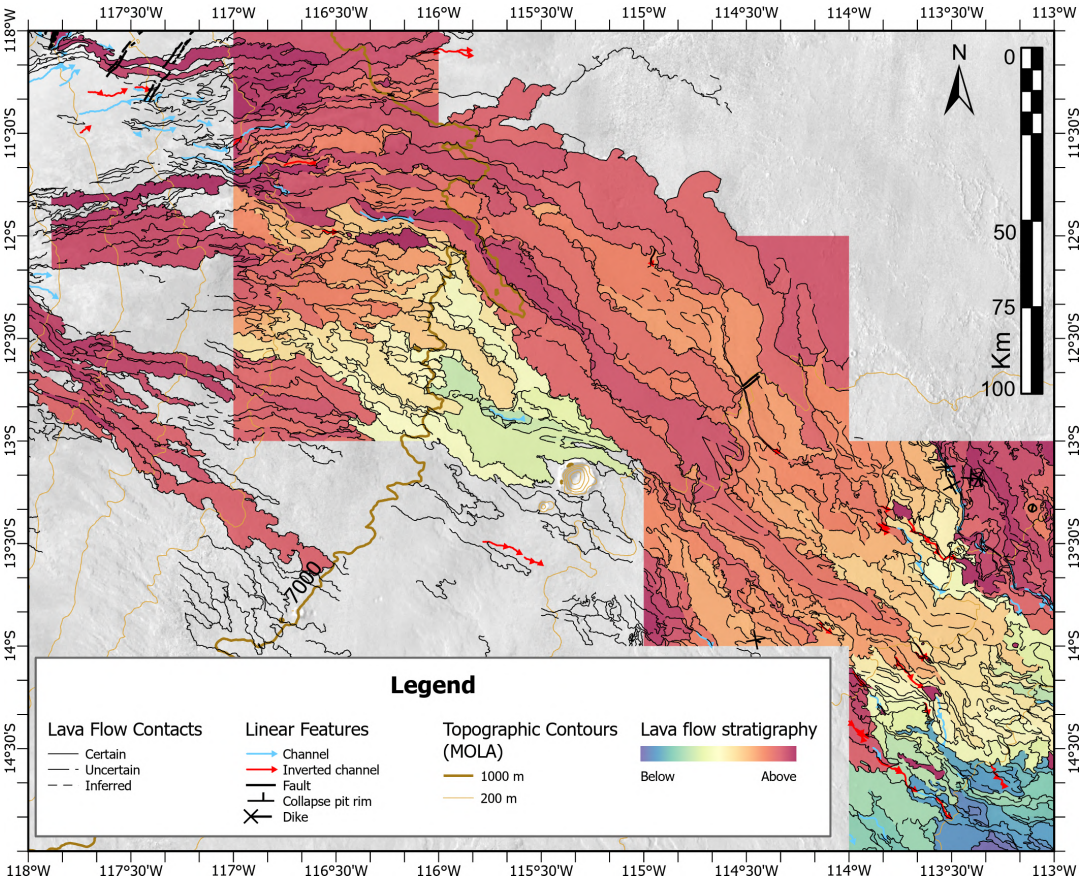


FIGURE 4.3: Lava flow stratigraphy inferred by AROMAS over THEMIS Day-IR.

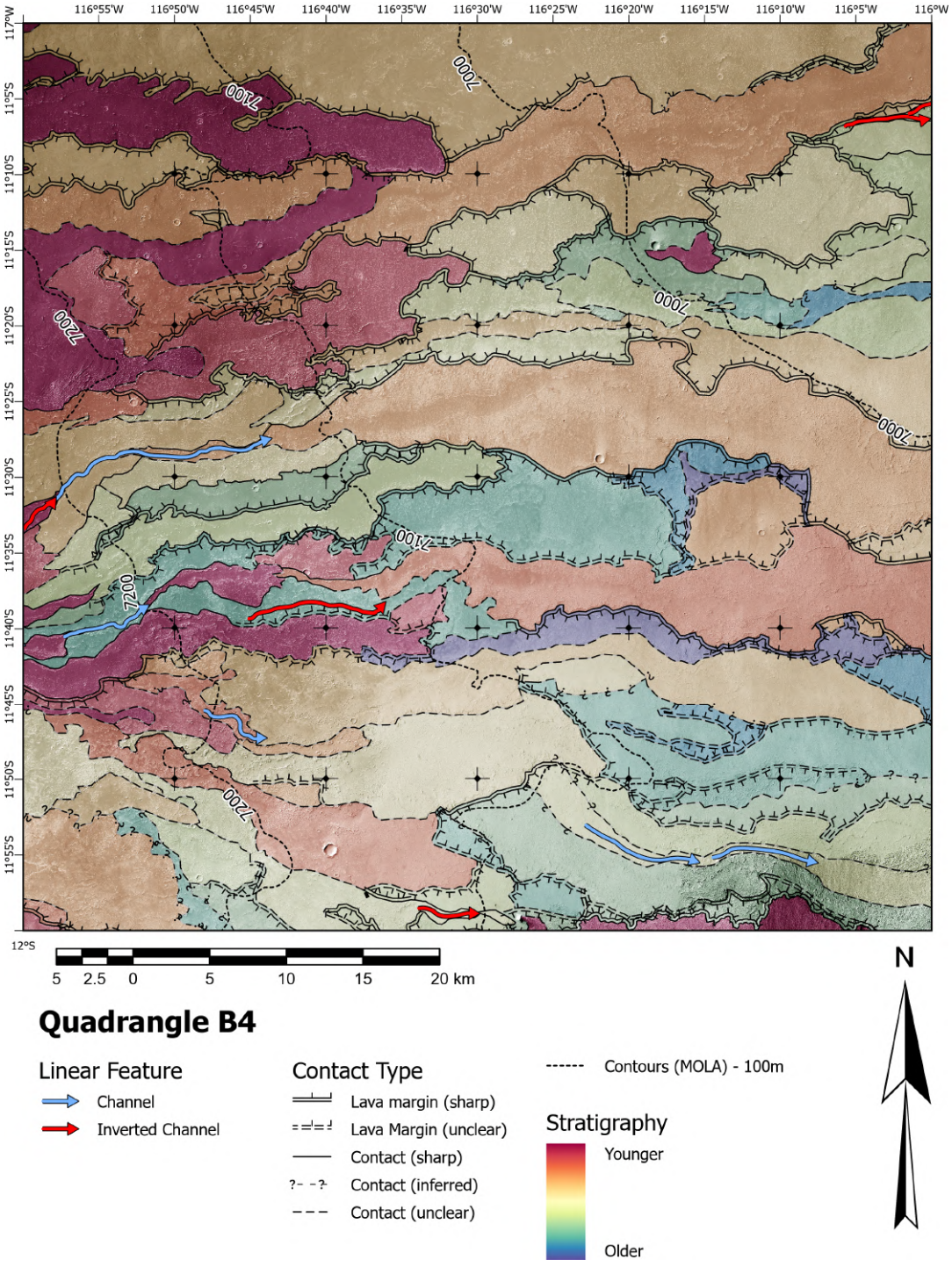


FIGURE 4.4: Stratigraphic map of Quadrangle B4

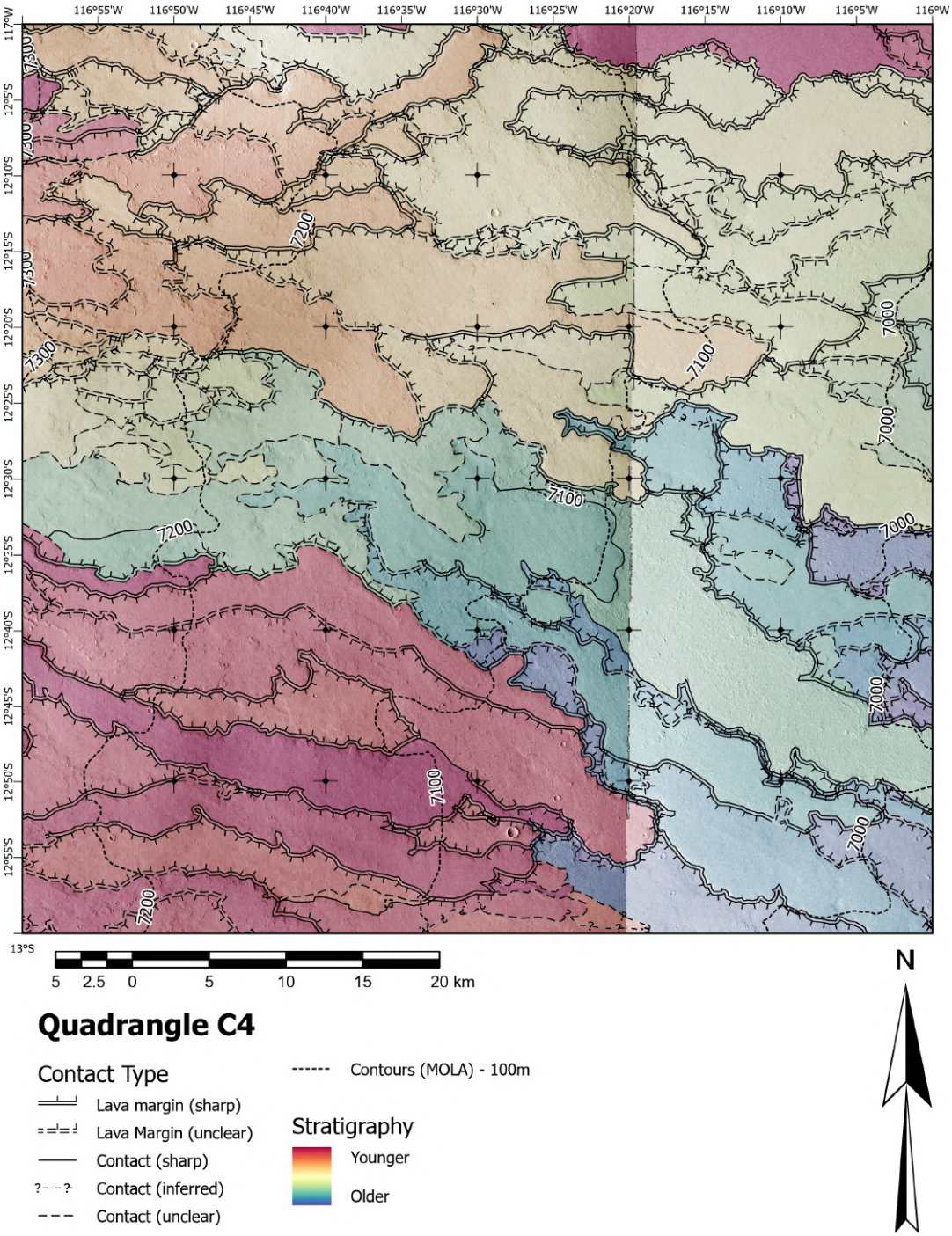


FIGURE 4.5: Stratigraphic map of Quadrangle C4

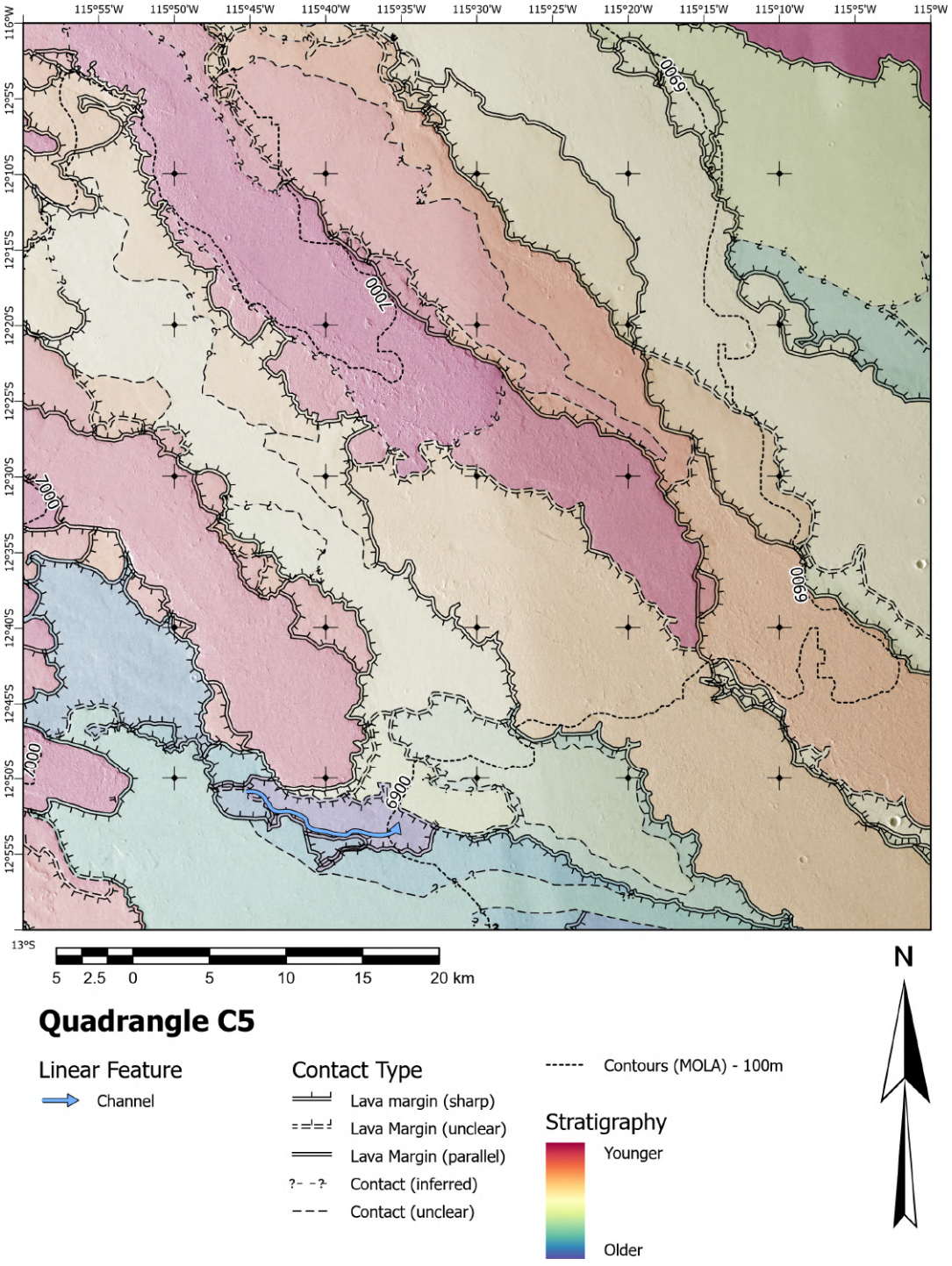


FIGURE 4.6: Stratigraphic map of Quadrangle C5

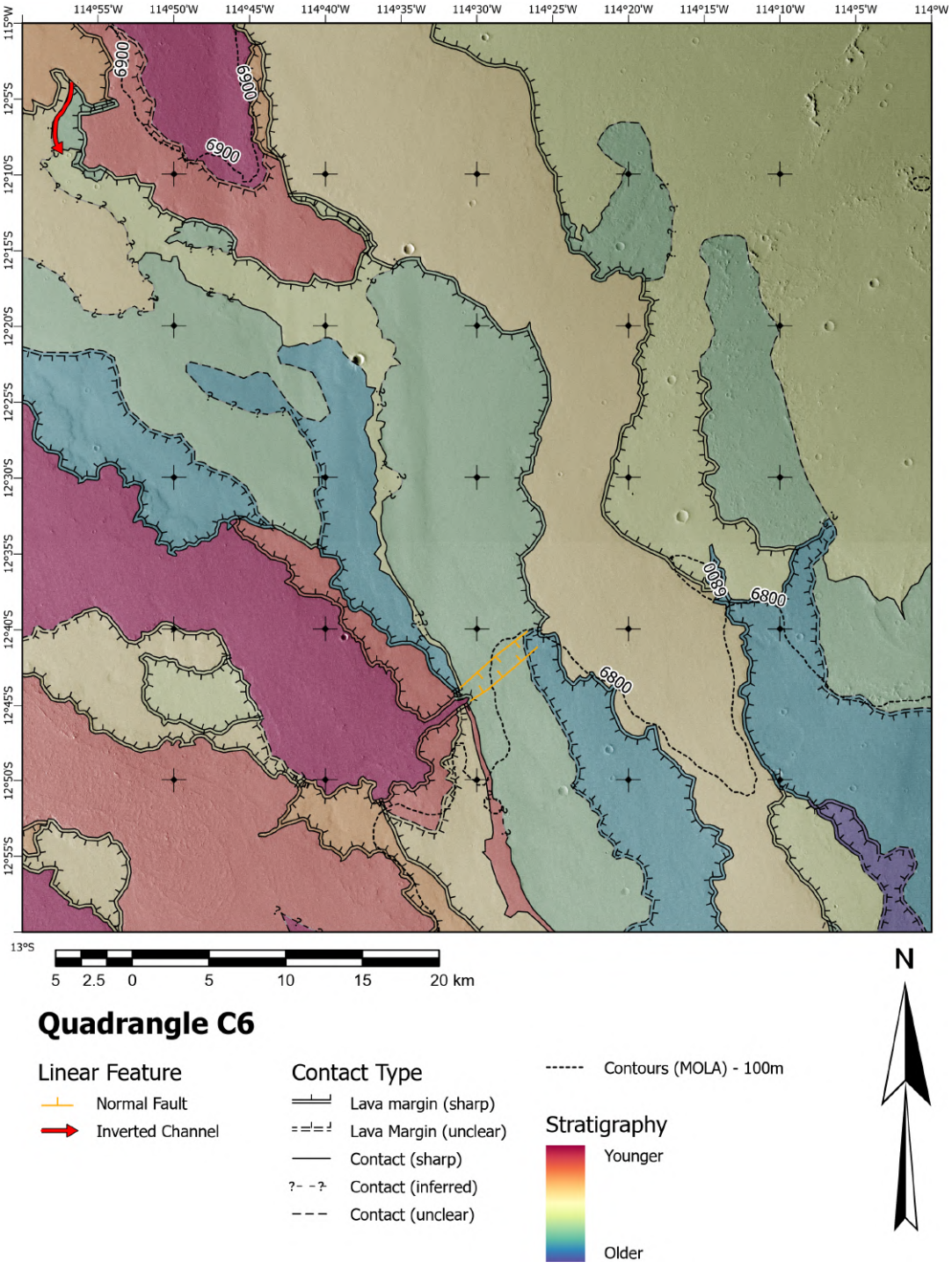


FIGURE 4.7: Stratigraphic map of Quadrangle C6

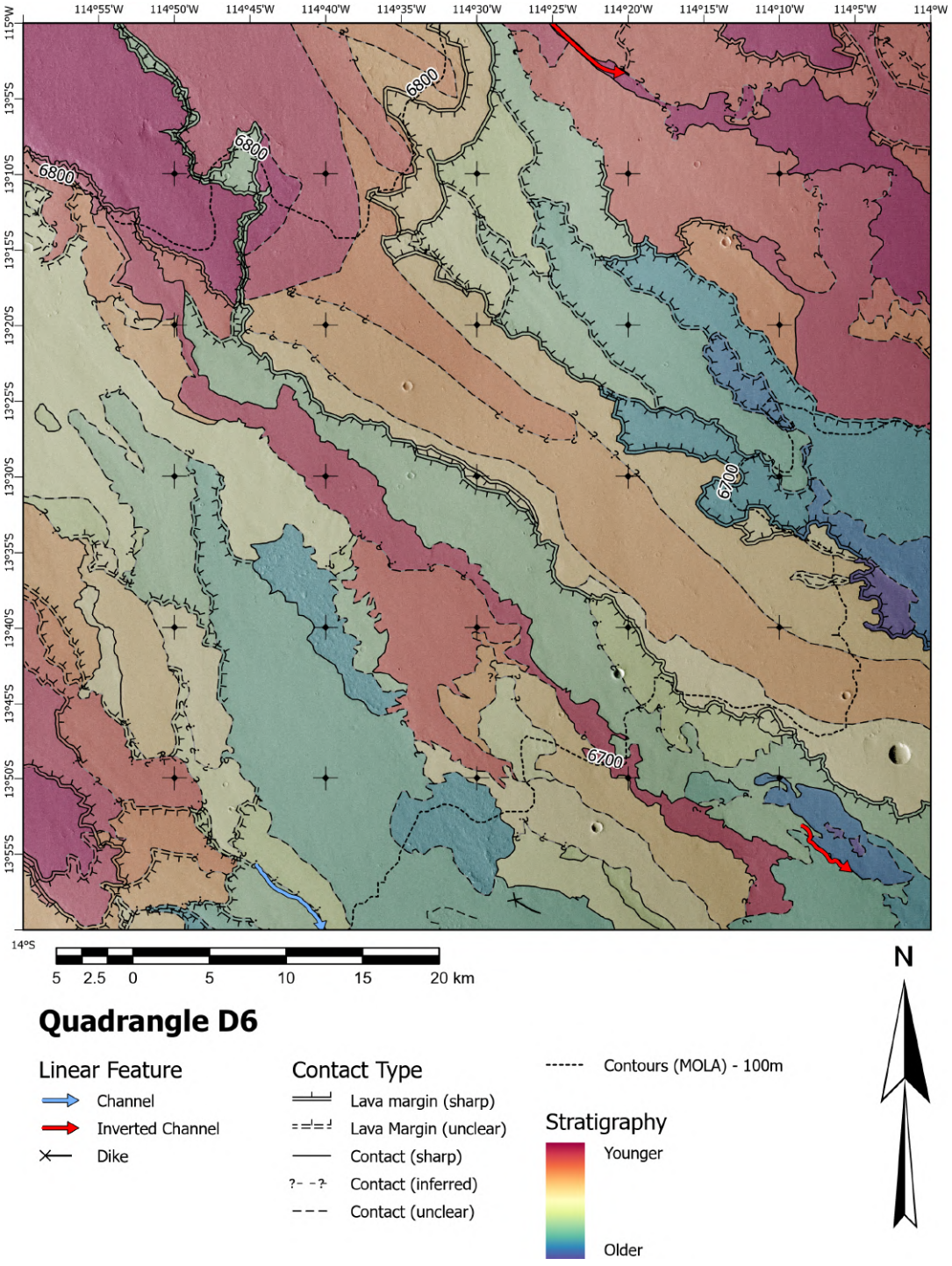


FIGURE 4.8: Stratigraphic map of Quadrangle D6

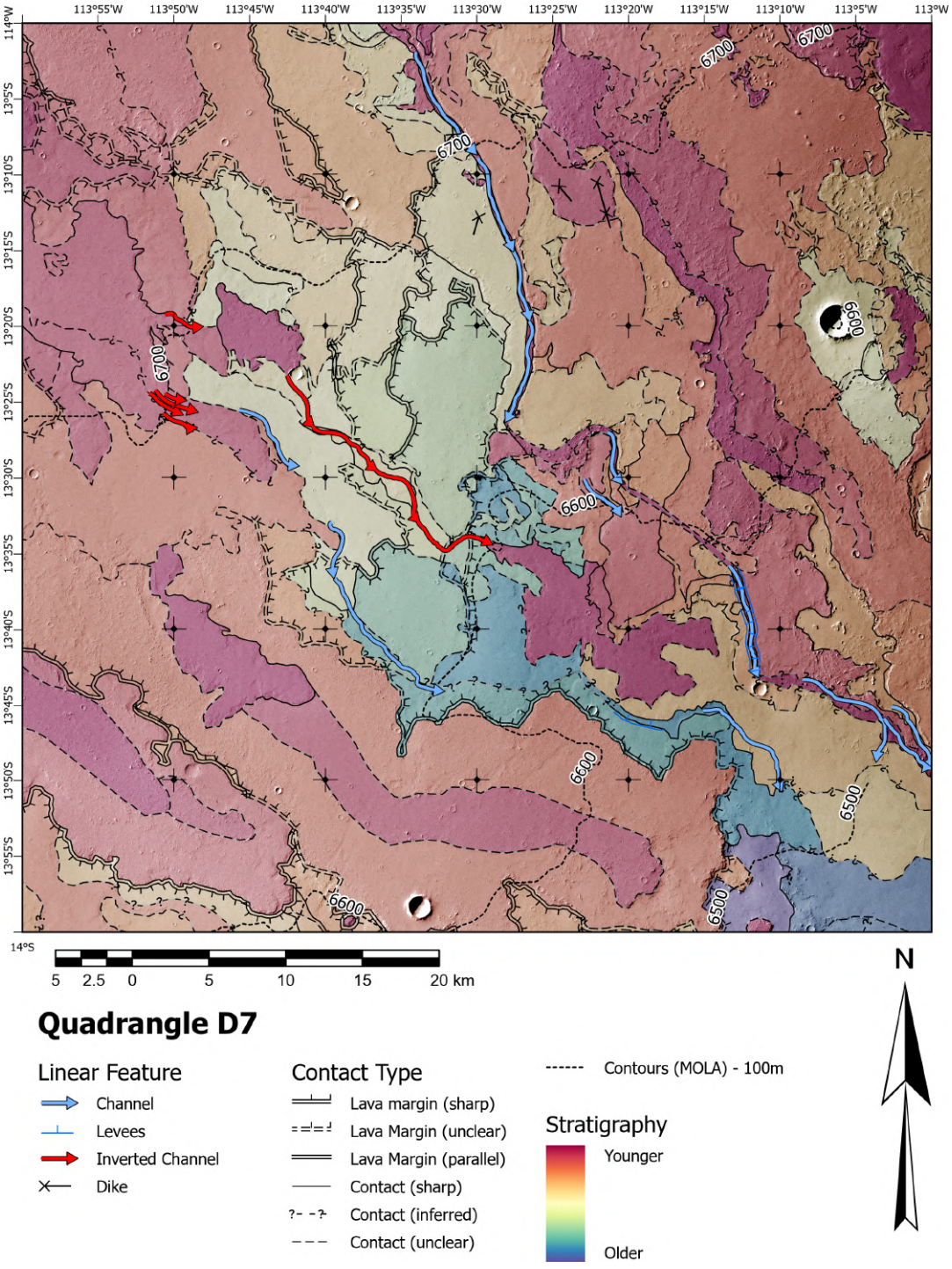


FIGURE 4.9: Stratigraphic map of Quadrangle D7

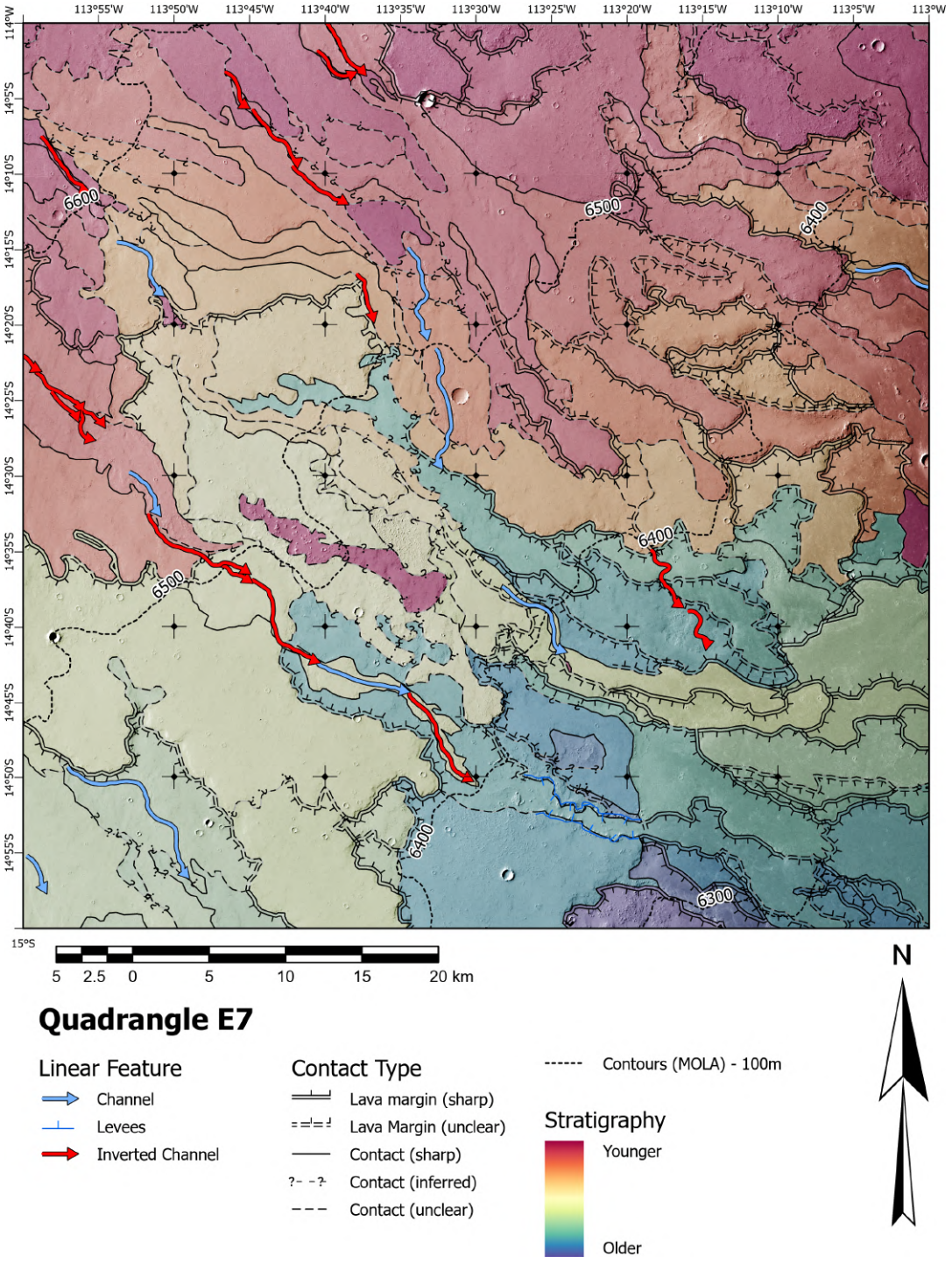


FIGURE 4.10: Stratigraphic map of Quadrangle E7

### 4.3.2 Lava flow description

Several flow types are identified in the mapped area: A-type are elongated and lobate lava flows (Fig. 4.11A). They display a rough texture and a bright albedo on CTX imagery. A smoother channel is often visible on the central part of the flow, bounded by rough-texture flow surface and channel levees. These flows are commonly found in quadrangles C5 to D6. On quadrangle, B4 and C4, smaller A-type flows are found more commonly. B-type flows are smaller and smoother compared to A-type and form undifferentiated lava fields with a high density of flows with dendritic margins (Fig. 4.11B). B-type lava fields cover the surface to the NW of the area of study, close to the edifice.
C-type lava flows are wide and smooth lava flows with higher dust cover than the two previous types (Fig. 4.11C). These lava flows are usually overlapped by A-type flows on central and SE quadrangles. C-type lava flows are frequently associated with inverted and classical channels (Fig. 4.12)

### 4.3.3 Tectonics

The Arsia Mons edifice is cross-cut by an array of concentric grabens well visible at THEMIS scale. In the study area, most of these grabens are overlapped by recent volcanic flows propagated from the southern apron (Fig. 4.13A). However, several other grabens cross-cut these recent flows. These grabens display a NE-SW trend (from N27°to N39°), similar to the set of grabens on the Arsia shield. Their width varies from several hundred meters to 2 km, and is bounded by two main normal faults with variable vertical offset, from a few meters to a few tens of meters (Fig. 4.13B). The relationships between the lava flow and the grabens vary from one location to the other, and a single flow can overlap an already emplaced fault scarp and be crosscut by another further down, which suggests a non-trivial chronology of emplacement (Fig.4.13C).

### 4.3.4 Potential source vents

Tracking the path of lava flows from their emplacement area to their potential source is no trivial task because flows cannot be discriminated in the area close to the edifice. However, in the lack of additional information, extrapolation of a flow direction upstream from the exposed flow part is a reasonable way to identify the location of the main vent among potentially observed candidates.

#### Collapse pits and lava tubes

Following the foot of the Arsia volcanic edifice to the west, a group of 4 km-scale collapse pit chains is well visible on THEMIS and CTX imagery (Fig. 4.14A). A 45km long and 400-1800 m wide depression extends from the westernmost pit in an overall eastward direction. Near the vent, the depression is wider and displays secondary channels and bounding normal faults (Fig. 4.14B). Further downstream,

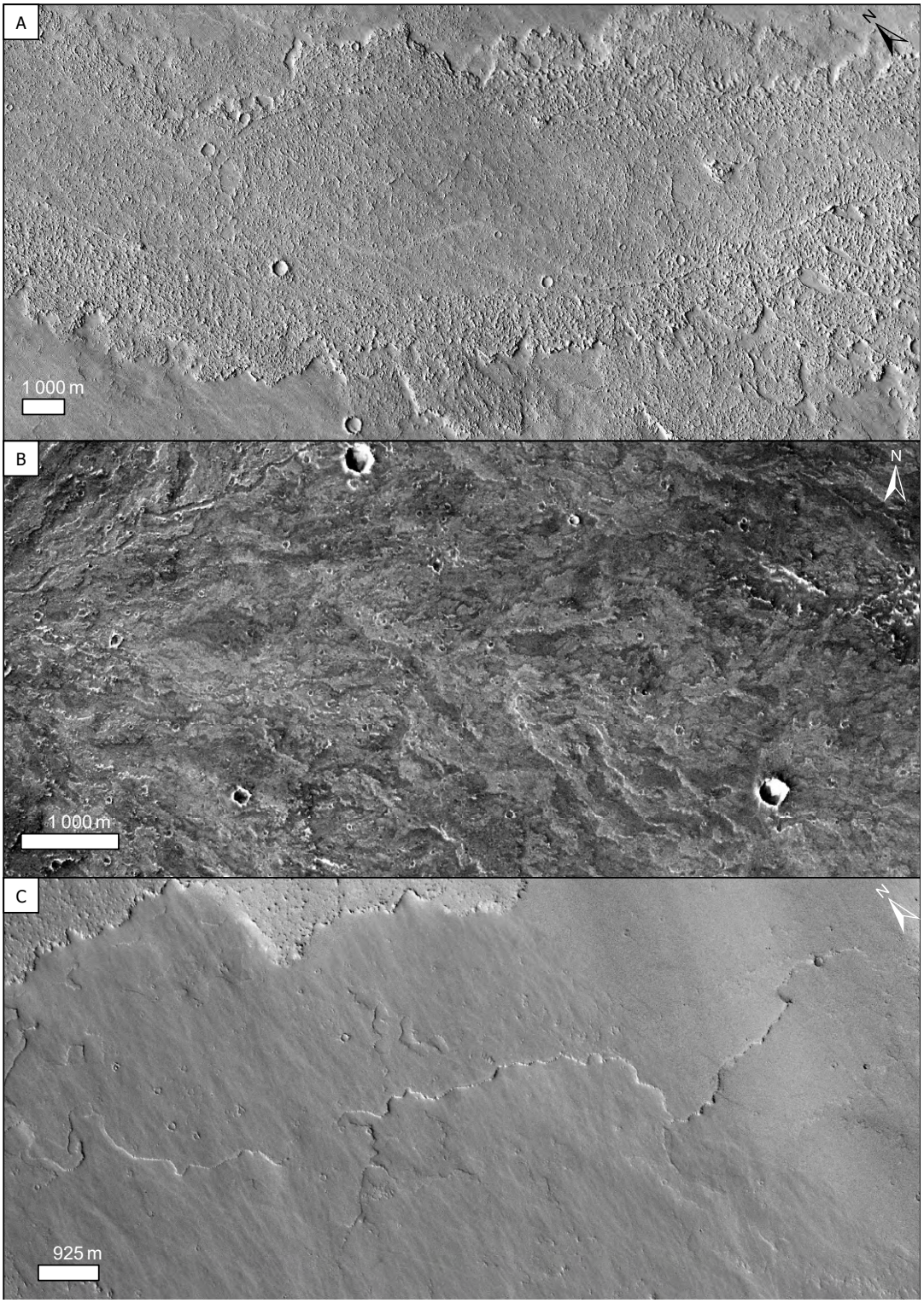


FIGURE 4.11: Close-up views of lava flows (CTX). **A**: Elongated and wide lava flow type with rough texture and light albedo commonly found in the central quadrangles. **B**: Small lava flows with a smoother texture characteristic of lava fields located close to the putative vent area. **C**: Older and smooth lava flow overlapped by an A-type lava flow.

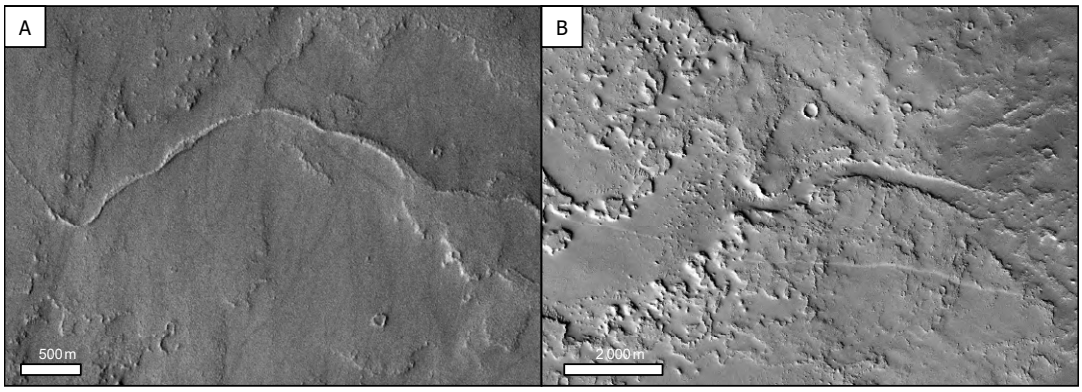


FIGURE 4.12: Inverted (**A**) and non-inverted (**B**) channels associated with C-type lava flows on CTX images.

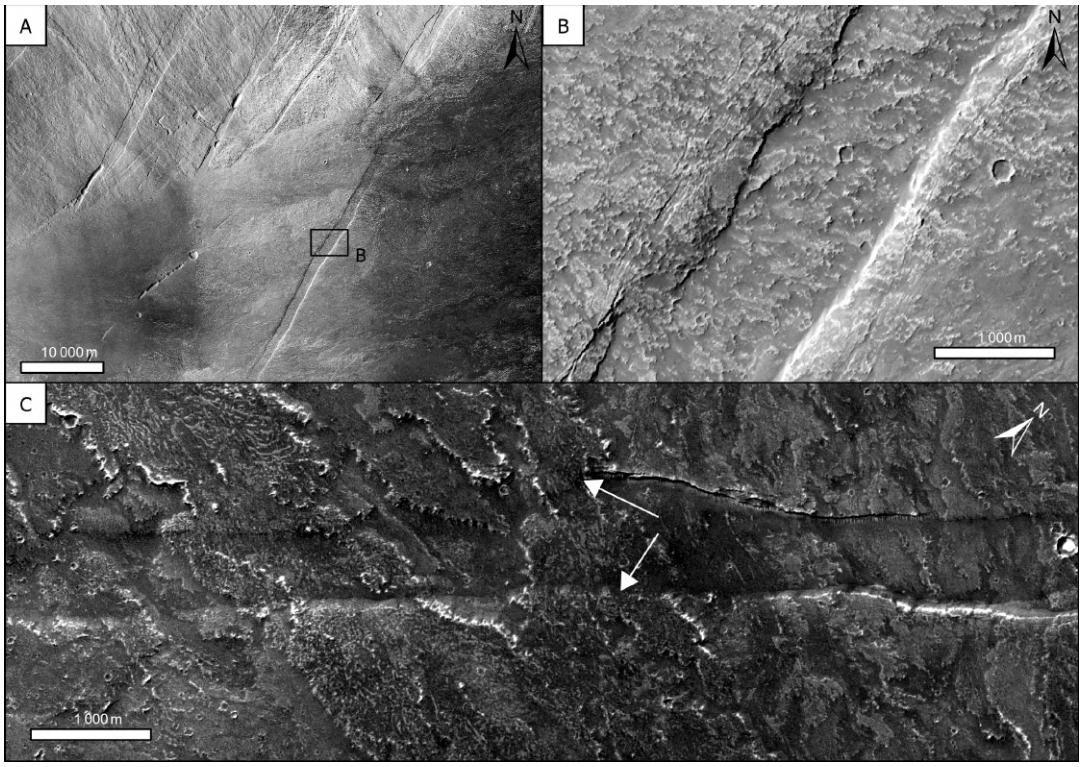


FIGURE 4.13: NE-SW trending grabens cross-cutting lava flows (CTX). **A**: A set of grabens cross-cutting the main edifice in the north, and overlapped by recent lava flowing eastwards. A more recent graben crosscuts these younger flows in the middle of the image. **B**: Close-up view of the recent graben composed of two main normal faults bounded by a set of parallel faults with a lower vertical offset. **C**: Recent lava flows partially overlapping and cross-cutting. White arrows show an example of lava flowing over the western normal fault and being cross-cut by the eastern fault, with a visible vertical offset, indicating a coeval emplacement between the flow and the tectonics.

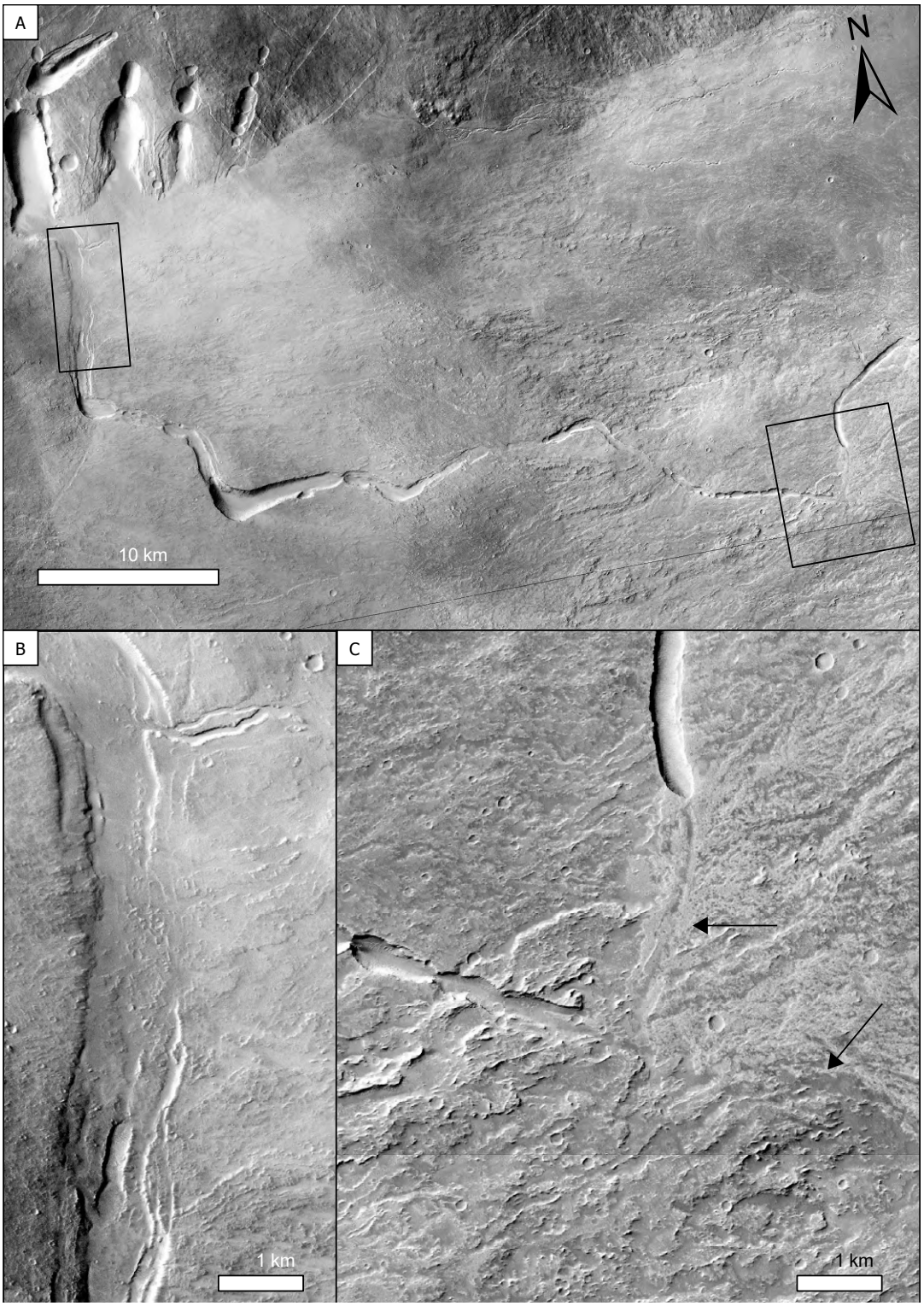


FIGURE 4.14: **A**: Potential source vent of lava flows in this study with insets of B and C. **B**: Close-up of the proximal part of the lava channel extruding from the westernmost collapse pit with bounding faults and eastward-flowing secondary channels. **C**: Collapse tube/channel with split surface expression of the lava path, to the north and the east (black arrows).

the feature is narrower and transitions from channel-like morphology to collapse-pit chains morphology. In Fig. 4.14C), the surface expression of the lava path is fading eastwards but does not completely disappear. Additionally, a secondary path appears to connect the main collapse pit chain and a similar northeastward depression (Fig. 4.16).

#### Small channels and rilles

A 100 m wide channel located 15 km north of the large collapse pits on the main edifice flanks (Fig. 4.14A),was extruded from a 1.2 km wide depression (Fig. 4.15A). This channel strikes similarities to volcanic sinuous rilles Lopez et al., 2012. Downslope, at the foot of the edifice, the sinuous rille-like channel transitions to braided channels following the slope break of the shield and the plains, in an eastward direction (Fig.4.15B). Further downstream, channel-fed elongated A-type lava flows are visible and fading under more recent emplacements (Fig. 4.15C and D), 50 km from the lava flows mapped in this study.

#### Fissure vent and low shields

Further to the east, 15 km west of the graben visible on Fig. 4.13A, an alignment of collapse pits linked to the features described in Fig. 4.14C extends over 40 km in a N40°direction. This collapse pit chain strongly resembles pit chains associated with terrestrial fissure eruptions found in Iceland or Hawaii (Fig. 4.16A and B). East of the putative fissure vent, an alignment of 5 km wide and up to 60 m high low volcanic shields extends over 18 km with a N75° direction. B-type lava flows were erupted from these shields and cross-cut to the east by the graben described in section 4.3.3.

### 4.3.5 Impact crater retention age models

Fig. 4.17 shows the results of modelled ages of a sample of lava flows where impact craters were counted. I selected lava flows with a minimum extent value, as small lava flows display few to no impact craters. The results show that the lava flow emplacement occurred between 330 ±60 Ma and 60 ±20 Ma. In addition to this sample, the age of three surrounding context surfaces was inferred in order to further refine the chronological bounds of lava flow emplacement. Two areas, named *ctxt_1* and *ctxt_3*, correspond to the substratum to the east and the south on which the lava was flowing. The third area, *ctxt_2*, corresponds to an undifferentiated lava field located northwest of the study area, which stratigraphically overlaps the flows located to the NW (i.e. the most recent ones here). The basement units were found to be 470 ± 70, and 660 ± 100 Myrs old respectively, whereas the context unit to the NW was found to be 140 ± 30 Myrs old (Fig. 4.18).
Comparison between the absolute ages derived from crater counting and the stratigraphic relationships shows consistency between the two methods for all but two units (Fig. 4.19.)

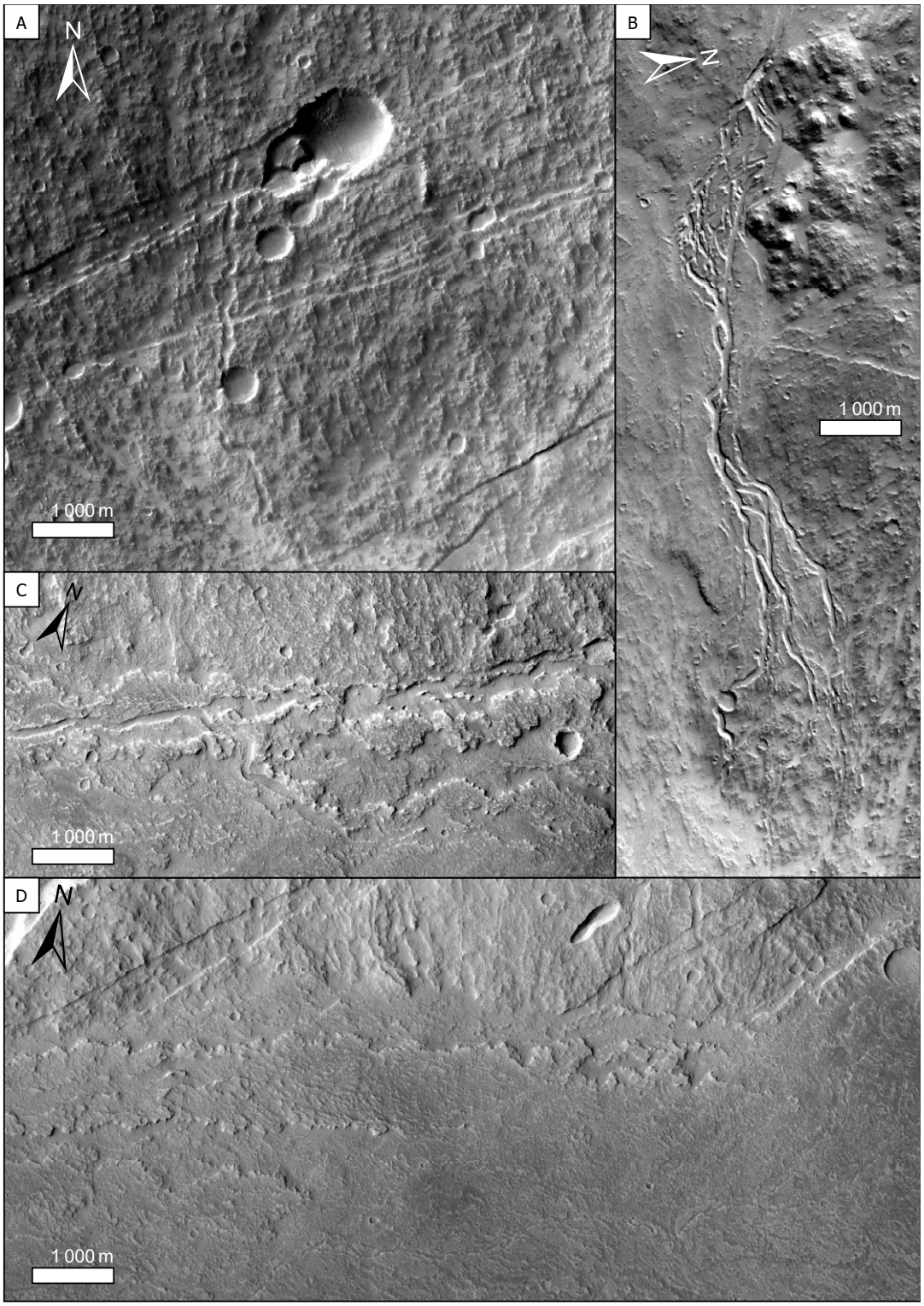


FIGURE 4.15: **A**: Source vent of the sinuous rille-like channel on the main edifice flank. **B**: Braided channels at the foot of Arsia Mons (on the right). **C**: Channel-fed lava flows extruding from the channel network on A and B. **D**: A-type lava overlapped by more recent B-type flows.

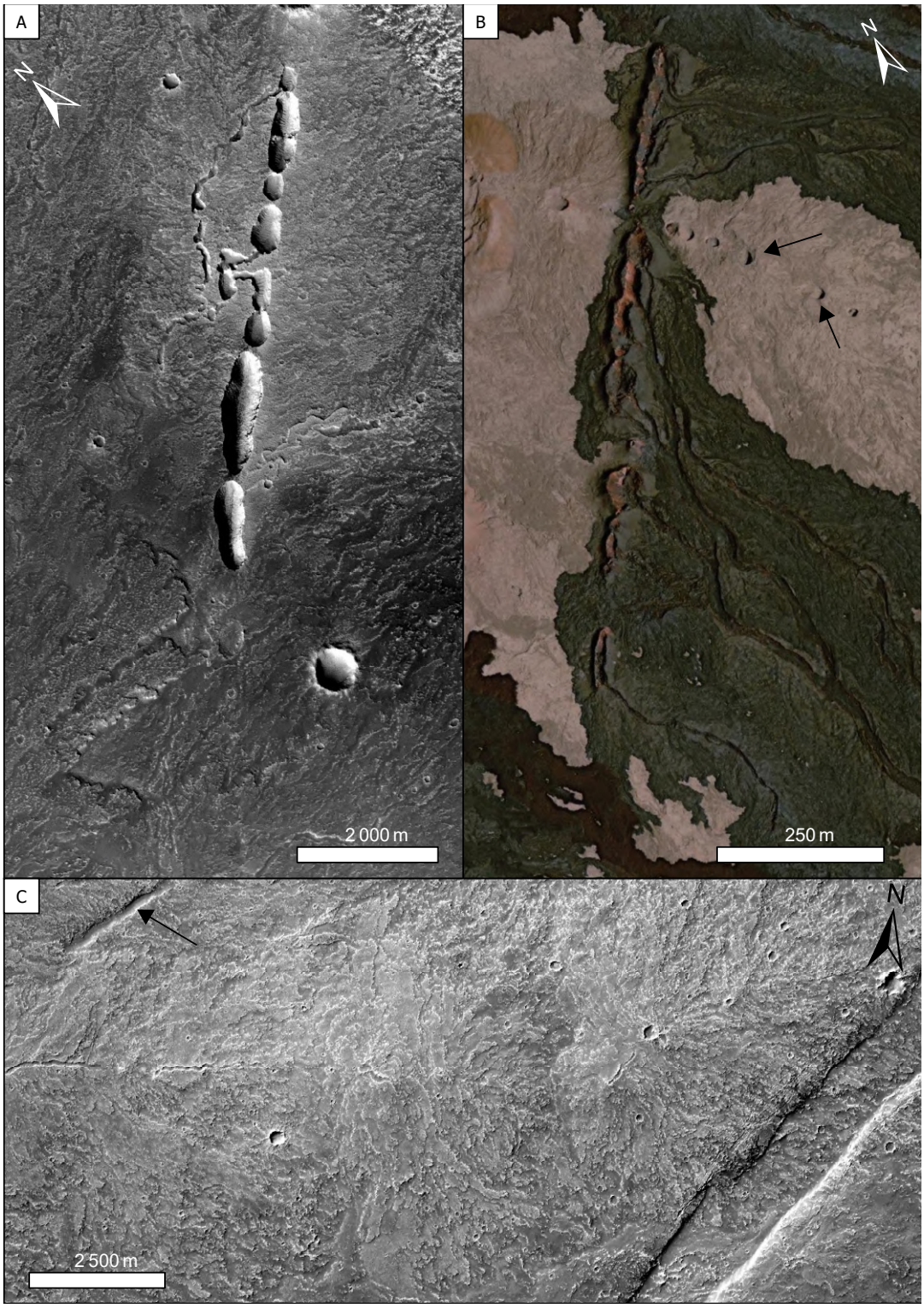


FIGURE 4.16: **A**: Collapse pit chain associated to a fissure vent at Arsia Mons. **B**: Fissure vent with basaltic flows on SW flank of Manua Loa, Hawaii. Black arrows indicate collapses from a lava tube (pukas), which have different shapes and depth than pits associated with the fissure. **C**: E-W Low shield alignment with B-type lavas. The black arrow indicates the northeastern tip of the fissure vent on A.

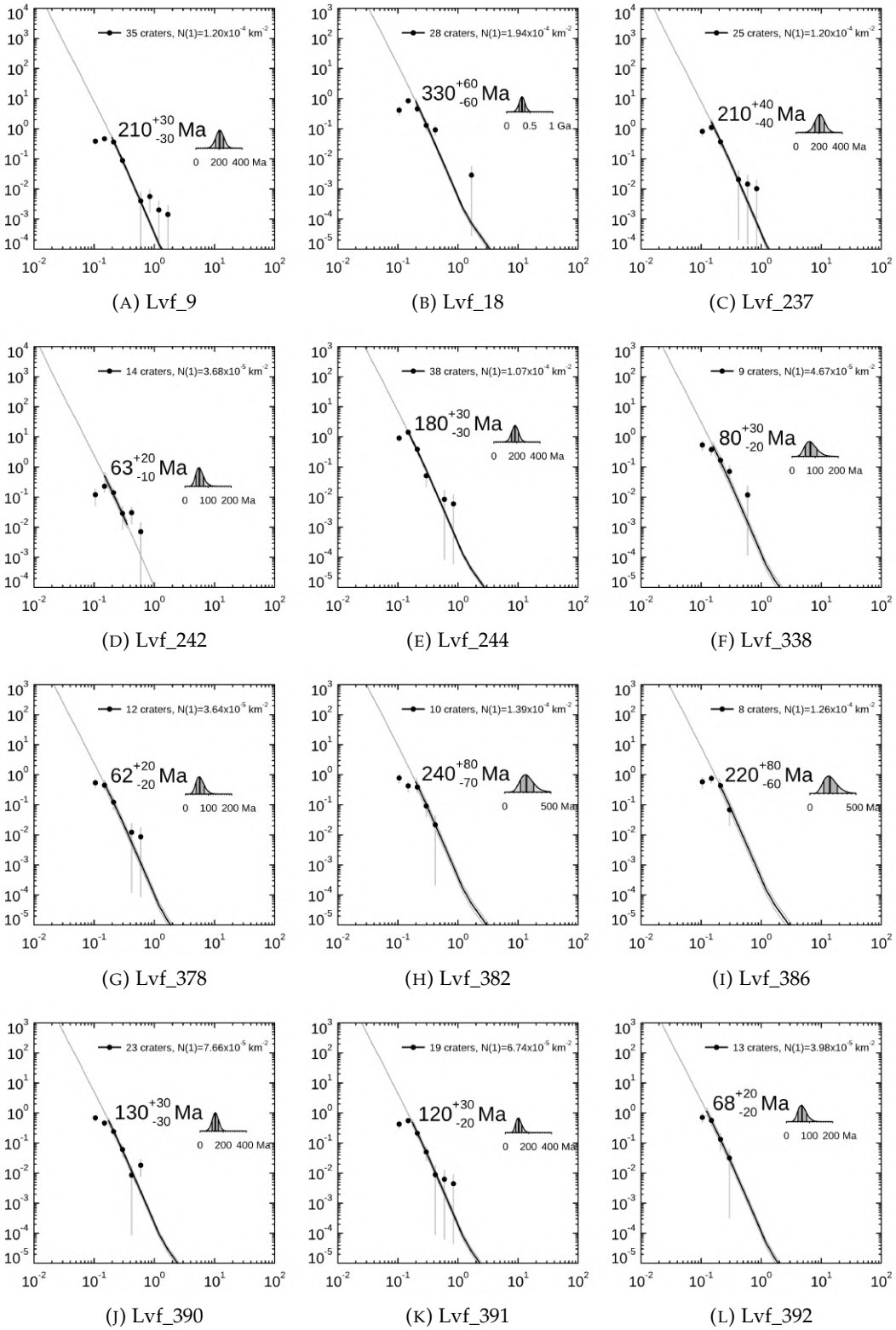


(A) Lvf_9 (B) Lvf_18 (C) Lvf_237

(D) Lvf_242 (E) Lvf_244 (F) Lvf_338

(G) Lvf_378 (H) Lvf_382 (I) Lvf_386

(J) Lvf_390 (K) Lvf_391 (L) Lvf_392

FIGURE 4.17: Modelled ages of selected lava flows from impact crater counting method. Each plot represents the differential crater density in $km^{-3}$ in the vertical axis and the crater diameter in km in the horizontal axis. Ages were inferred by fitting a Poisson Distribution Function on the data using the Hartmann and Daubar, 2017b's production function and the Hartmann, 2005's chronology function.

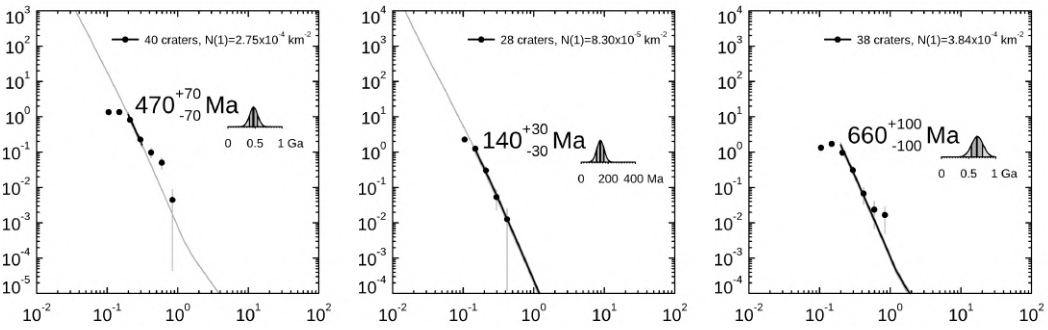


(A) Context Area nr.1 (B) Context Area nr.2 (C) Context Area nr.3

FIGURE 4.18: Modelled ages of selected context area from impact crater counting method. See Fig. 4.17 for plot description.

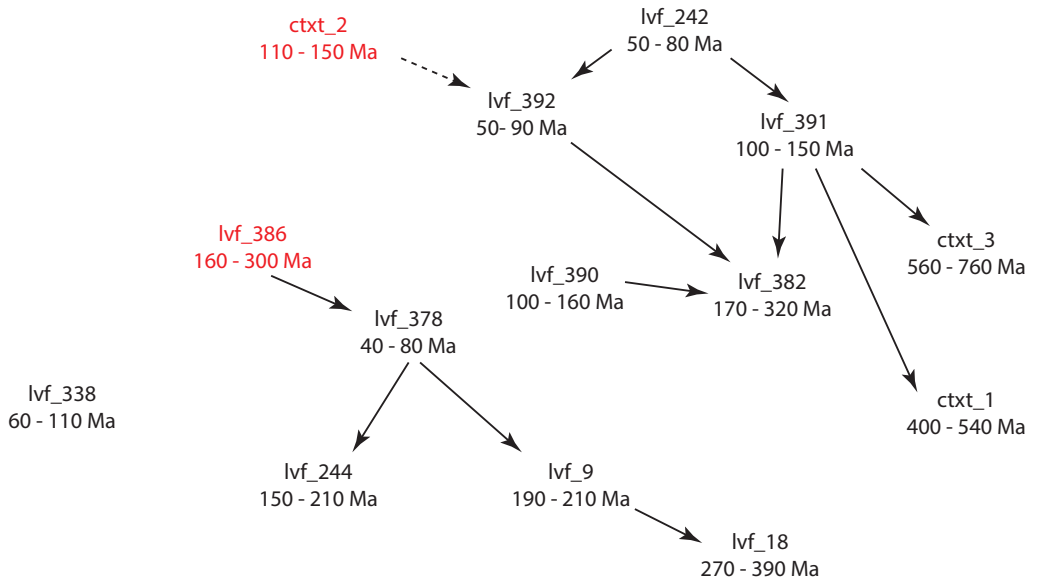


FIGURE 4.19: Stratigraphic relationship of lava flows where crater counting ages were calculated. Arrows represent the overlapping relationships. In red are the ages derived where pollution from secondary craters is likely.

### 4.3.6 Morphometrics

Lava flow morphometrics is presented in Fig. 4.20. The apparent length of the flows, where visible (i.e., not overlapped by a younger unit), ranges from 48 m to 188 km, with an average of 15.9 km. To represent more accurately the real length (i.e. from the source to the tip), flows were connected to an artificial polygon that connects the potential vent (Fig. 4.14) to the proximal part of the highest flows in the stratigraphy. The total length of the lava flows inferred by AROMAS ranges from 48 m to 574 km and averages 208 km. The average width of lava flows at Arsia Mons ranges from 5 m to 12.2 km. The mean width of the lava flows over the entire dataset is 2.90 km. On exposed margin scarps, the average thickness of the flows ranges from 1 to 51 m. Overall, the mean thickness of the whole set of flows is 13 m.
Lava flows with a smaller apparent and total length, and width are found more commonly in the NW and SE bounds of the dataset (Fig. 4.21). Longer and wider flows on the other hand are found more commonly in the middle area. Thicker flows are more commonly found on the proximal part of the lava flow set, in the NW.

### 4.3.7 Fractal Dimension

The fractal dimension of lava flow margins at Arsia Mons ranges from 1.04 to 1.45 (Fig. 4.22). The distribution of fractal dimension values does not follow a single Gaussian trend but displays five domains with maxima at 1.06, 1.11, 1.17, 1.26, and 1.35. Although no simple correlation between flow size and fractal dimension exists in this dataset, higher fractal dimension values (> 1.3) appear to be associated more commonly with smaller flows, notably in the SE quadrangles of the area of study, where C-type lavas are found. Lava flow margins with fractal dimensions lower than 1.1 are more frequently found on the NW regions and appear more associated with A-type lavas.
In addition, lava flows with higher pixel variety on THEMIS Day and Night-IR (i.e., the number of different pixel values) have margins with lower fractal dimensions than flows with lower pixel variety (P-value < 5% - Fig. 4.23). However, on the same dataset, no similar invert correlation exists between pixel standard deviation value and fractal dimension. Lava flows with a higher variation and standard deviation of quantitative thermal inertia have margins with higher fractal dimensions than flows with lower thermal dimension variety and standard deviation (P-value < 5%). Lava flows with higher average thickness are more frequently associated with higher pixel variety and lower fractal dimension (Fig. 4.23).

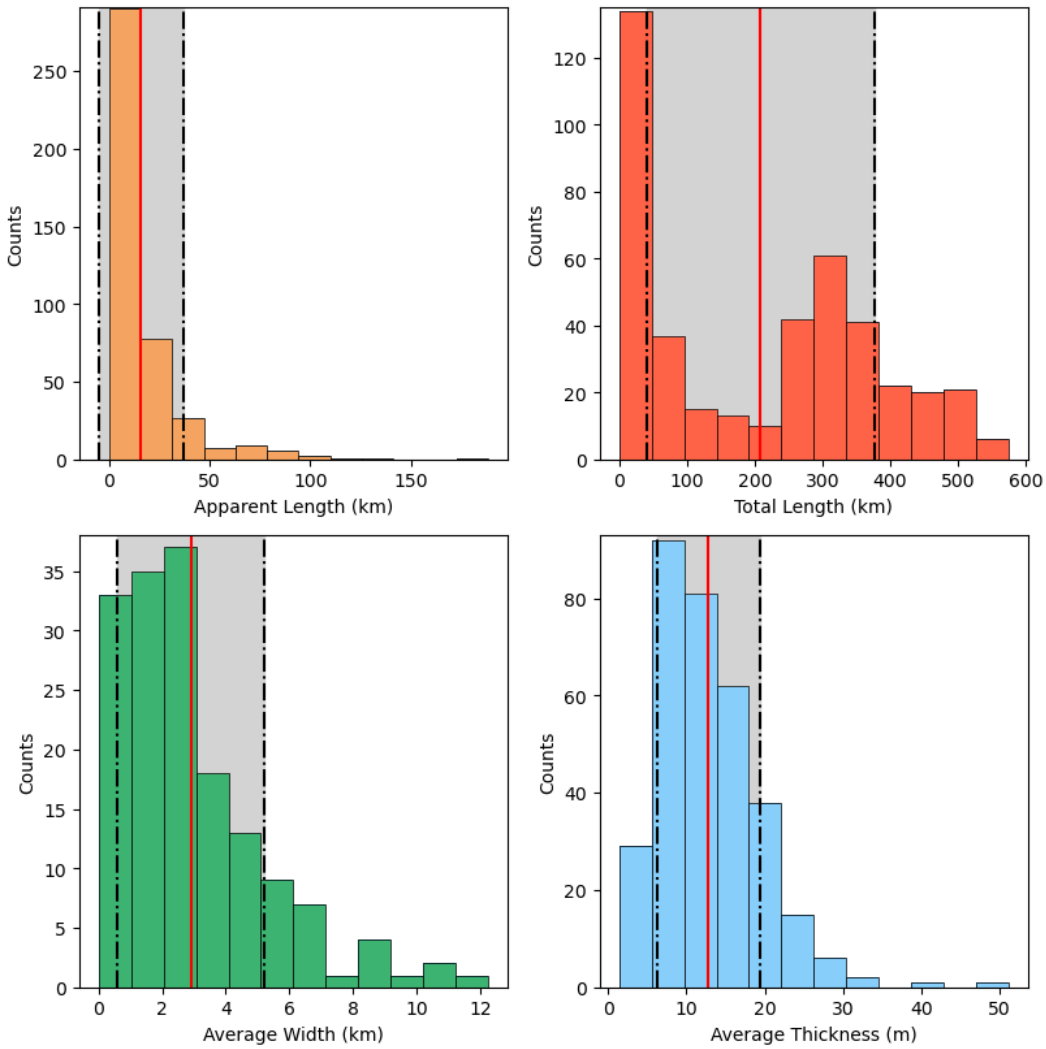


FIGURE 4.20: Histogram of lava flow morphometrics. The apparent length corresponds to the length of the visible part of the flow. The total length corresponds to the apparent combined with the inferred length (see methods). The width of the flows corresponds to the average width measurements in places where the flows are fully visible. The average thickness is computed only where the margins of the flows are exposed, and not overlapped by another flow. On each histogram, the red line indicates the average value for the whole distribution and the grey area, represents the standard deviation from the average.

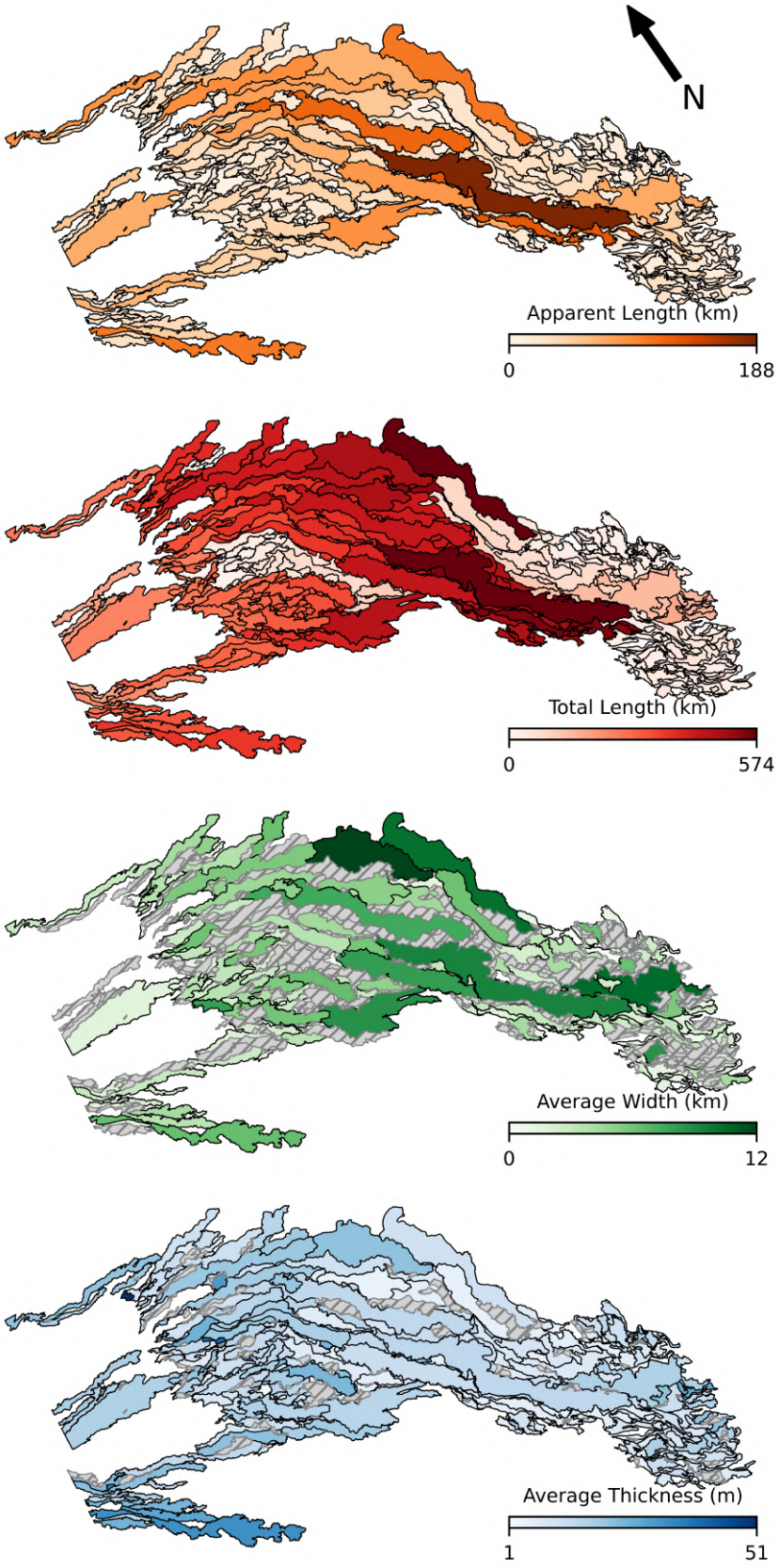


FIGURE 4.21: Map distribution of lava flows with respect to their morphometric characteristics. See Fig. 4.20. Missing values are represented with hatched grey lines.

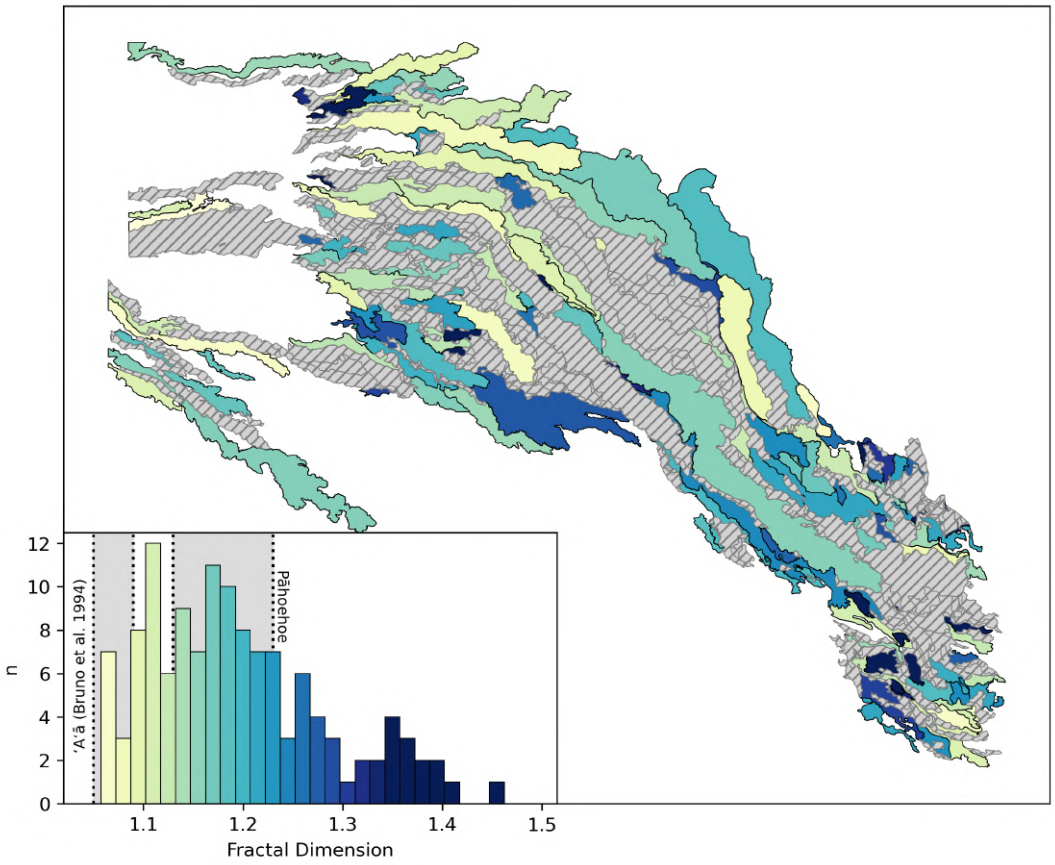


FIGURE 4.22: Distribution of fractal dimension values and geographical distribution of associated lava flows. Missing data are represented by hatched grey lines.

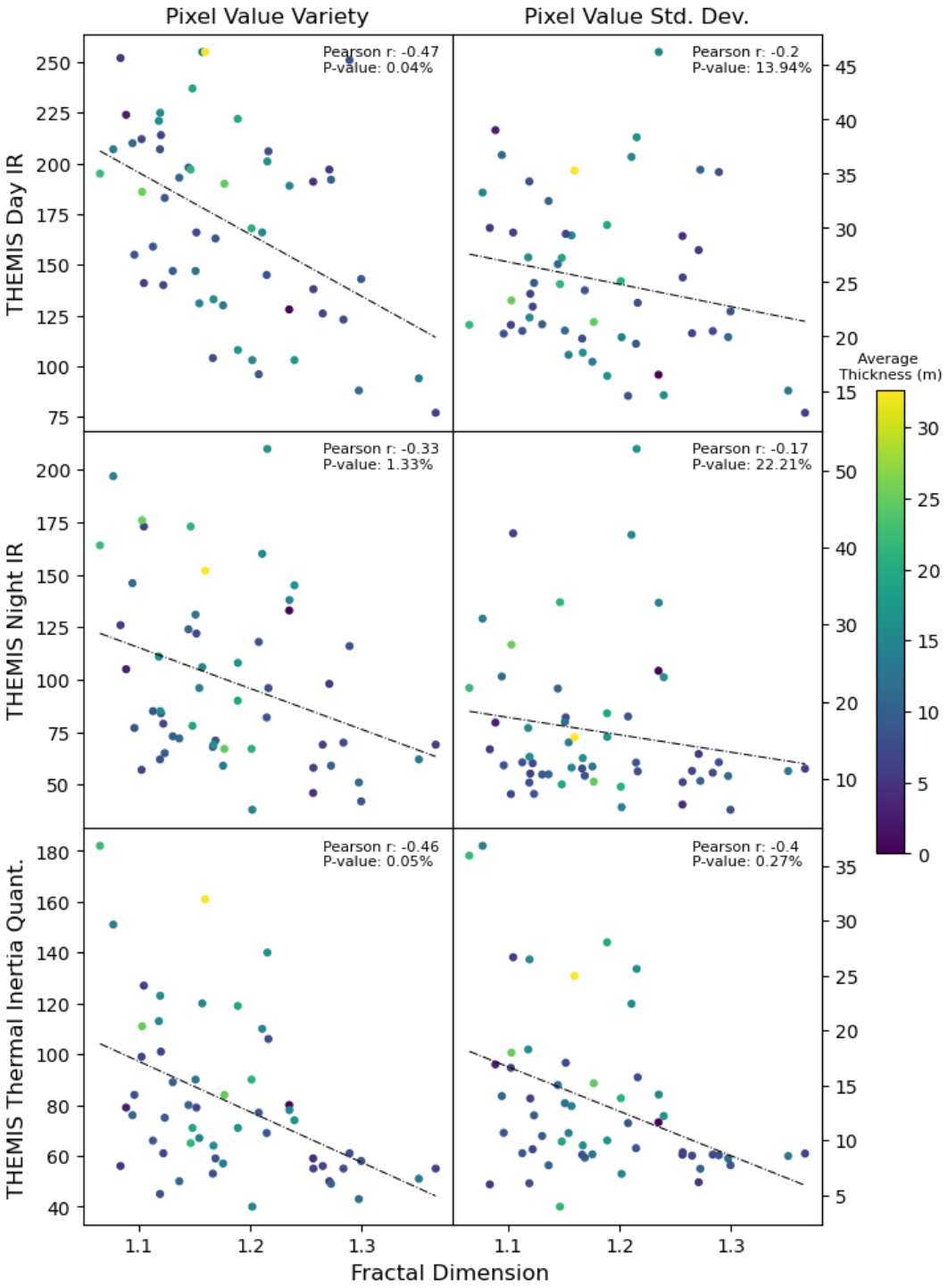


FIGURE 4.23: Comparison of fractal dimension and pixel value variation in each lava flow for THEMIS Day-IR, Night-IR and THEMIS-derived quantitative Thermal Inertia. The colour of each point represents the average thickness of the flow.

## 4.4 Discussion

### 4.4.1 AROMAS output

#### Stratigraphy and topological sorting

At first glance, the proposed reconstructed stratigraphy by the algorithm is consistent with the emplacement of lava flows and the known chronology of volcanic activity. The youngest flows are more frequently found closer to the edifice (i.e. the source), whereas the older units are more commonly found far away from the Arsia edifice to the southeast. As volcanic activity is thought to have waned over the geological times at Arsia Mons (and on Mars in general), older flows should be longer, extending further away from the source and therefore be more visible to the southeast. However stratigraphic levels of flows located in the SE quadrangles are high with some of them labelled as located at the top, stratigraphically (e.g. Fig. 4.10).
AROMAS uses a topological sorting function that can create a hierarchical-directed graph from a dictionary of relationships between different units. Flows which are not overlapped by another unit are classified "on top" by the current function. This particularity has two consequences on the output. First, units located at the boundaries which are not in contact with little units anything tend to be "overranked" in the stratigraphy. Consequently, the stratigraphy can appear inconsistent between two distant quadrangles because existing units exist connecting the flows which are exposed only between these quadrangles are not considered. One way around this is to ensure a continuum between the two distant quadrangles, across the intervening area. Another way is to generate an artificial polygon that serves as a "bridge" between a section of bounding units from the two distant quadrangles, providing a reference to the algorithm for correct flow unit classification.
The second consequence of the topological sorting function used by AROMAS is that a unit lying directly above all its neighbours is also classified as “at the top”. For instance, in the quadrangle E7, at 14°35’S, 113°40’W (Fig. 4.10), there is an example of such a unit. While the neighbouring units were ranked as being located between levels 10 to 13, the central unit, which is above its neighbours, was ranked at level 0 (i.e., at the top) instead of being attributed the level 9, for instance.
Further improvements on AROMAS should aim to correct these shortcomings and provide a stratigraphy closer to reality.

#### Length and width

In the test sample presented in chapter 3, the apparent length and average width measured manually in ArcGIS and the values computed by AROMAS were consistent within < 10% (Fig. 3.10). Visual comparison between the numerical values and the extent of the flows on the map shows that they are also consistent with the observations for the set of lava flows studied here (Fig. 4.21). However, the total length inferred by AROMAS shows some inconsistencies for the lava flows located

in the southeastern quadrangles. As these lava flows are located further away from the vent, their total length should be higher than the ones located in the northwest. AROMAS uses the stratigraphic tree built in the previous step to infer the total distance of the flow from the putative source, following the path of lava flows located above it. From the algorithm point of view, the potential source is interpreted as the proximal part of the lava flows located stratigraphically at the top (see chapter 3). Therefore, an error in the stratigraphic classification of the units will drastically change the total length computation. For instance, if a lava flow is wrongly classified at the top, the distance to such flow is much lower than the real distance to the lava flows located further northwest, at the top of the stratigraphic sequence. Improvements in the topological sorting and stratigraphic classification discussed above should thus improve the total length of the flow.

#### Thickness

The current version of AROMAS allows us to estimate the thickness of a flow at the margin using MOLA data. In reality, lava flows often undergo inflation during their emplacement, meaning that their thickness could vary not only along their length but also their width (e.g. Bleacher et al., 2017; Kolzenburg et al., 2018). One could argue that thickness along the profile could be measured by extending the MOLA elevation profiles from several hundreds of metres to the whole width of the flow. As the lava flows are located on a generally sloping surface, with other topographic variations created by underlying flows, extending the elevation profile away from the margin can increase the contribution of larger-scale topographic variations and therefore yield non-reliable thickness measurements. Future improvement of AROMAS could use higher-resolution DTMs (where available) to first model the underlying topography and remove its contribution from the thickness measurements.

### 4.4.2 Fractal Dimension and pāhoehoe/‘a‘ā discrimination

Three types of lava flows were identified in this study: Large, bright and rugged lava flows (A-type), darker and smoother lava flows (C-type), and lastly smaller and smoother lava flows in high density close to the low shields in the NW (B-type). The characteristics of A and C-types strongly match the two types of lava flows identified by (Crown & Ramsey, 2017) located SW of Arsia Mons interpreted as ‘a‘ā and pāhoehoe lava flows respectively. In this study, the author used visual comparison with terrestrial analogues as well as thermal characteristics of the flows.
Bruno et al., 1992 and Bruno et al., 1994 showed that the fractal dimension of lava margins can be matched with the flow type. At first glance, fractal dimension values for lava flow margins in this study do not show a similar bi-normal distribution corresponding to ‘a‘ā and pāhoehoe lava-type end-members (Fig. 4.22. A-type flows display rugged textures with regions of higher elevation corresponding to more massive parts of flows where topographic lows are filled by loose material

deposits. C-type flows on the other hand have a smooth surface, and are therefore mantled uniformly by dust or ash. Therefore, the variety of pixel values (i.e. albedo) is stronger for A-type than for C-type flows. Following the same logic, A-type flows also have a higher variety of thermal inertia than C-type flows. Fig.4.23 shows that flows with a higher variety of albedo and thermal inertia have margins with lower fractal dimensions.
On Earth, 'a'ā flows have a lower fractal dimension than pāhoehoe flows (Bruno et al. (1994)). The results found here are consistent with this observation made on terrestrial lava flows and confirm the interpretation made by Crown and Ramsey, 2017 on Arsia Mons' lava flows. The higher thickness of A-type rugged flows is also consistent with the observations made by Crown and Ramsey, 2017 SW of Arsia Mons.
The absolute values of fractal dimension found in this study do not match the values found on Earth. This discrepancy could be related to the nature of the flows themselves or the method used. It could also be due to the scarcity of available fractal dimension measurement data at terrestrial lava flows, which may prevent from understanding the logic of fractal dimension distribution behind the measured values. Using AROMAS on more terrestrial datasets could provide insights into the representativeness of the existing data and the accuracy of the method when it comes to fractal dimension (see chapter 5).

### 4.4.3 Chronology of emplacement

The lava flows studied here are plausibly connected to the vent located east of the southern apron, at the foot of the edifice. While most of the flows may originate from this source, observations show that the lava may have followed different paths at different stages of the volcanic activity (Fig. 4.14). A first set of lava may have first emplaced following an eastward path from the main channel (Fig. 4.14). The activity could have then migrated northwards and originated from the NE-SW fissure vent. The lava path would then have been mechanically constrained by the syn-tectonic activity observed around the various grabens cross-cutting the several sets of lava flows (Fig. 4.13. This hypothesis is supported by the grossly similar trend of the fissure (N40-N75°) and the grabens (N27-N39°) direction.
Such an interpretation is challenged by the inferred absolute ages, which show lava flow emplacement as recent as 40 Ma in the set of flows located between the main path and the secondary path (group A2 - Fig. 4.24) of older age (> 110 Ma, group A1bis and A2bis - Fig. 4.24). However, lava flows located in the NW display a higher contamination by secondary craters, which could affect the modelled age.
Stratigraphically, the group A2bis, consisting of relatively smaller A-type flows, overlaps the area right south of it, where low shields and B-type lava flows are present. Extrapolating paths are consistent with a source corresponding to the fissure vent (Fig. 4.16) or the braided rille-like channels flowing down the flank of the edifice (Fig. 4.15). The context area with non-discriminated B-type flows overlaps the proximal part of group A2 flows, indicating a more recent emplacement. Group

A2 and A1bis consist mostly of relatively large A-type flows. Group A1 consists of relatively smaller A-type flows. In the SW, this set is bounded by a group of similar flows which can be connected to another vent located more to the W, on the southern apron.
Combining the results from impact crater age modelling, stratigraphic relationships and image observations, the following chronology of emplacement can be proposed:

- At around 330 ± 60 Ma, the activity started and A-type lava flows, interpreted as ‘a‘ā flows overlapped older, smoother and darker flows (C-types) interpreted as pāhoehoe which were emplaced during older volcanic episodes (> 400 Ma).
- Coeval tectonic activity opened NE-SW trending grabens close to the edifice and cross-cut already emplaced flows.
- Source migrated from the foot of the edifice to a fissure vent and an E-W alignment of low shields associated with dense and relatively small B-type lava flows.
- A last set of lava flows related to the fissure eruption or another vent located on the flank over (group A2bis).
- In parallel a set of A-type lava flows deposited to the W related to another vent located on the southern apron.

Overall, the recent activity spans a period of over 190-350 Myrs. Absolute ages and lava flow sizes of groups A1bis and A2 are consistent with a peak in the effusive rate at Arsia Mons’ southern rift apron at 150 Ma, coeval with an episode of intra-caldera activity reported by J. A. Richardson et al. (2017). The activity then waned, to stop between 40-80 Ma.

### 4.4.4 Evidence for explosive activity

The lava flows studied so far indicate an intense effusive activity at Arsia Mons between 270-390 to 40-80 Ma. Although episodes of older, and more explosive activity could have occurred before this, their records are masked by the younger lava flows. At the tip of group A1bis, one can observe lava flowing around the rim of an older impact crater (Fig. 4.25). The crater floor is mantled by what appears to be a loose material deposit with bedform-like features visible on the western slope. This deposit could correspond to deposits related to previous volcanic episodes and then be reworked by the wind into bedforms.
To test this hypothesis, one should confirm that the features on the western crater wall are indeed aeolian bedforms, indicating they are made from a loose material such as volcanic ash. However, DTM cannot be generated here because no stereo imagery covering this crater is available. To the east, other similar-looking deposits and bedform-like features were sought on older terrains and found in the Noctis Labyrinthus region (see Chapter 6).

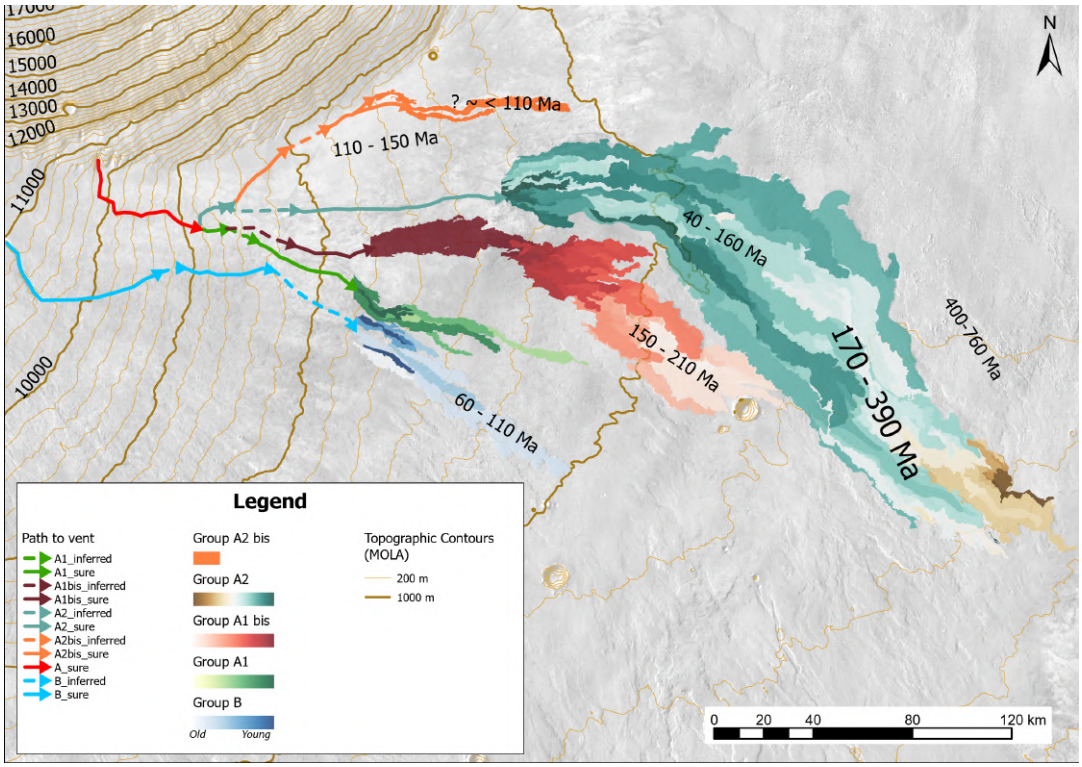


FIGURE 4.24: Proposed interpretation of the different sets of lava flows emplacement with the path to their respective potential vents and where impact crater retention ages were derived.

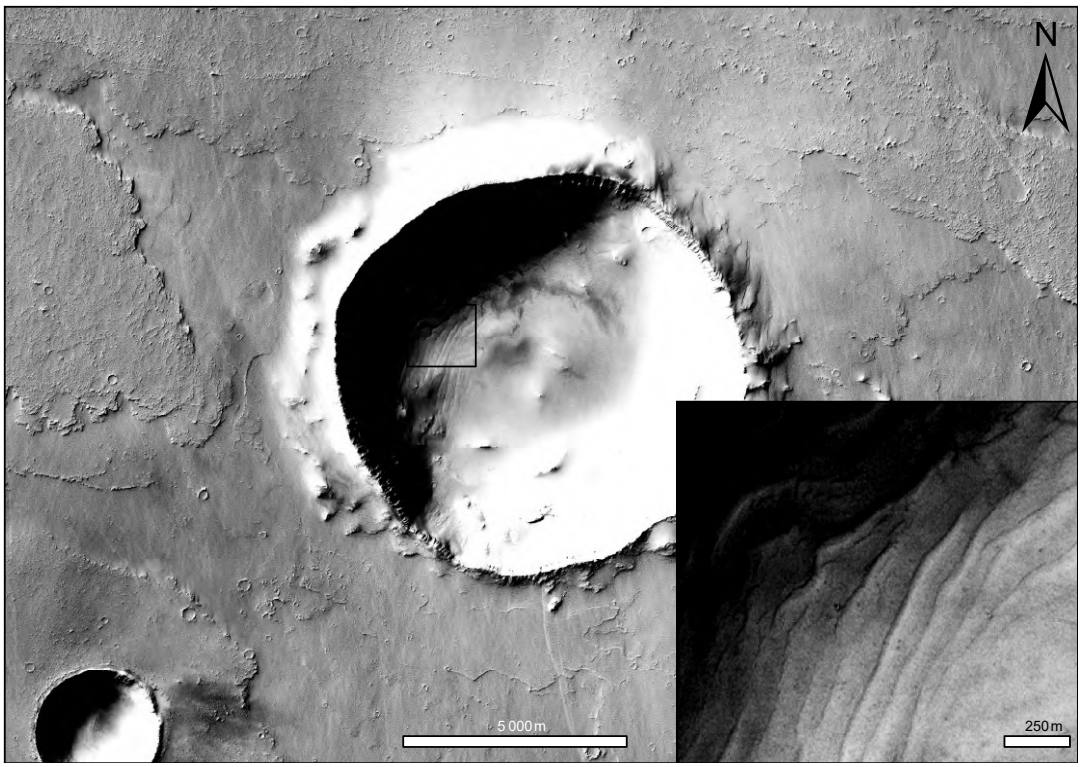


FIGURE 4.25: Lava flowing around an older impact crater. The crater floor is mantled by a loose material deposit

# Chapter 5

# A terrestrial lava field analogue: Lanzarote - La Corona

## Introduction

The AROMAS workflow developed for this work was first used to reconstruct the stratigraphy of individual lava flows on Mars and derive morphological parameters. In essence, such workflow can be applied on any planetary body where lava flows exist and where images are available. To demonstrate this, AROMAS was applied to a set of terrestrial lava flows. Thus, using the same methodology to study similar geomorphological processes on Earth and on Mars also allows for comparative planetary geology, and is often yielding valuable results in understanding the processes on both planetary bodies.
During the completion of this thesis, I contributed to updating the geological map of northern Lanzarote, Spain (Fig. 5.1, 5.2) in collaboration with colleagues at the University of Padua, Italy, within the framework of the Europlanet 2024 - GMAP project. Using this opportunity, lava flow contacts that I digitised during this work were parsed into the AROMAS workflow. The geological map was published by Dr. Ilaria Tomasi in *Journal of Maps*, in 2023 (Fig. 5.3 - Tomasi et al., 2023).

## 5.1 Geological Context - Lanzarote, Canary Islands

### 5.1.1 Canary Islands

Lanzarote is a Spanish island located 150 km northwest off the coast of Morocco (Fig. 5.1), and is part of the Canary Islands archipelago. The chain of islands is thought to have formed through sustained volcanic activity related to a hotspot (referred to as the Canary hotspot) and consists of seamounts that overgrown on the 180 to 150 Myrs Jurassic ocean crust (Hoernle and Carracedo, 2009). The volcanic activity recorded at each island spans almost 70 Myrs, with the oldest samples found on Tropic Seamount, located at the northeastern tip of the archipelago whereas the youngest island is thought to be the island of Hierro, at the southwest (e.g. Geldmacher et al., 2001). Overall, the age of formation of each island is decreasing from northeast to southwest, which is consistent with the movement of

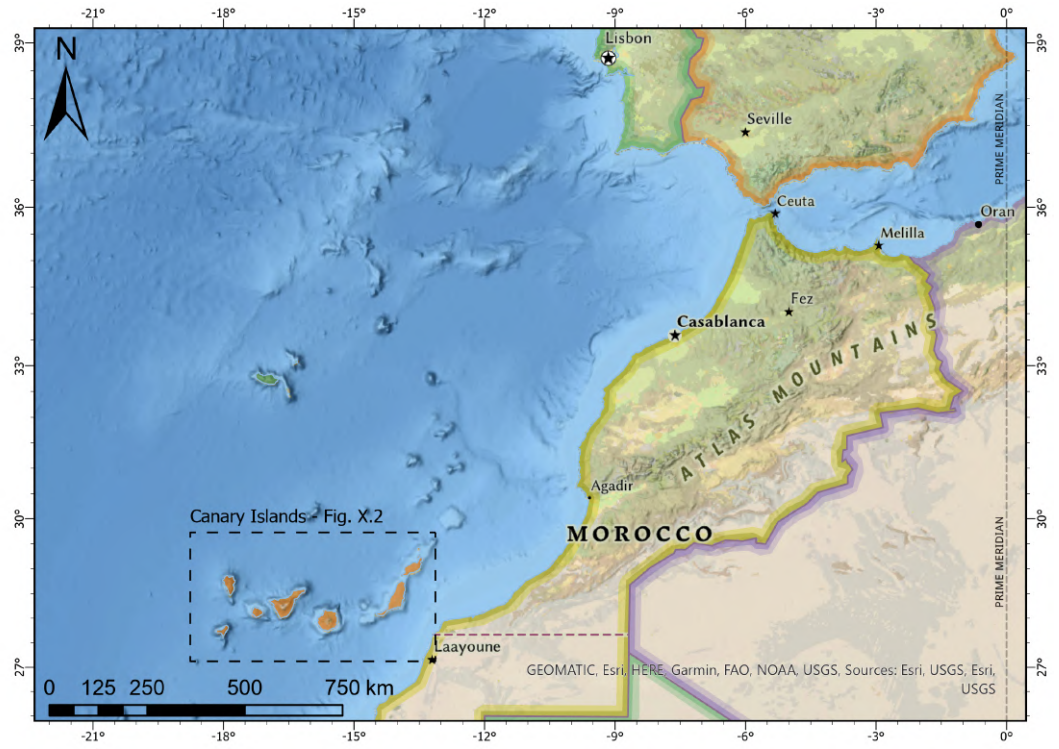


FIGURE 5.1: Location of the Canary Islands archipelago off the coast of Morocco and Western Africa, more than 1200 km away from mainland Spain.

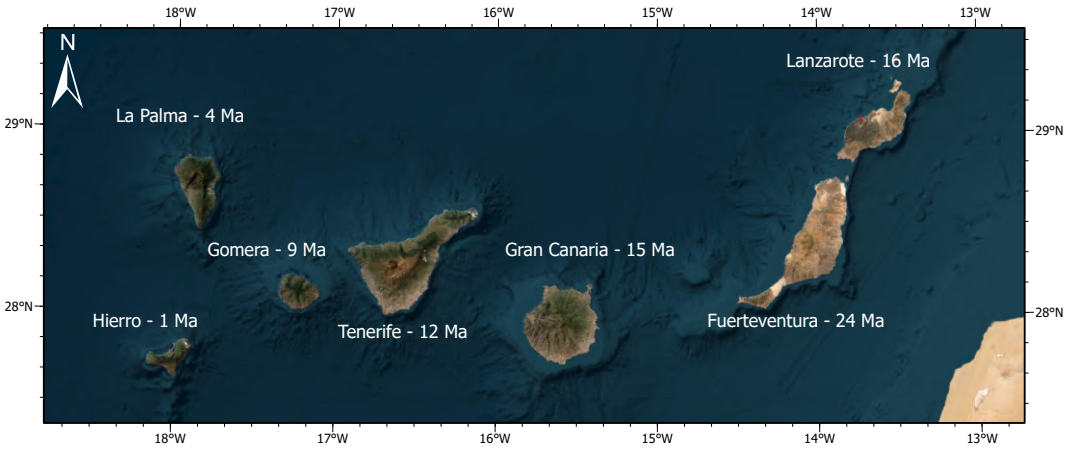


FIGURE 5.2: The Canary Islands with the age of formation of each main island. The age variations testify to the motion of the African plate over the Canary hotspot.

the African tectonic plate over the Canary hotspot (Fig. 5.2). Volcanism is still active nowadays with eruptions occurring sporadically, the latest being on September 2021 at *La Cumbre Vieja*, on La Palma island (Carracedo et al., 2022). While the plate movement has constrained most of the historic eruptions on southwestern islands, several Holocene eruptions were recorded on Tenerife and Lanzarote (Hoernle and Carracedo, 2009).

### 5.1.2 Lanzarote and La Corona volcano

Lanzarote is thought to have emerged 15 million years ago in the form of two shield volcanoes which are now partially eroded (Hoernle and Carracedo, 2009). This shield-forming activity extended until 6 Ma and was followed by a 5 Myrs hiatus before activity restarted, forming 4 distinct volcanic fields, from 1.2 Ma until the XVIIIth century. The northeast of the island is mainly covered by basaltic lava flows related to the volcanic episodes surrounding Los Helechos-La Corona edifices (91-21 ka). The volcano of La Corona is a 269 m high tephra-cone with a 400 m wide crater that sits on La Famara shield volcano units of Miocene age (Tomasi et al., 2023). It is most famous for its associated 8 km long lava tube, that extends from the flank of the edifice down to the coast where it is now partly flooded (Tomasi et al., 2022). Covering an area of 32 $km^2$, basaltic flows related to La Corona volcano form a lava field locally called *malpais de la Corona*.

## 5.2 Datasets and methods

A hillshade product derived from LiDAR data at 2m of horizontal precision from the Spanish National Centre of Geographical Information (CNIG) was used to identify lava flow geological contacts from remote sensing. Unclear contacts were further refined during the fieldwork carried out for the completion of the geological map. Data were imported into ArcGIS Pro and contacts were digitised in REGCAN95 projection at 1:5000. Mapping workflow followed the steps and requirements by AROMAS used on Arsia Mons lava flows (see chapter 3).

## 5.3 Results

#### Geological Map

101 individual lava flows were mapped and classified by AROMAS. Output stratigraphic reconstruction shows shorter and younger lava flows closer to the cone whereas older flows are found further away, close to the coastline (Fig. 5.5).

#### Morphometrics and fractal dimension

Morphometric results show that the lava flows of La Corona have an apparent and total length of 732 m and 3550 m on average, respectively (Fig. 5.6). Flows have an

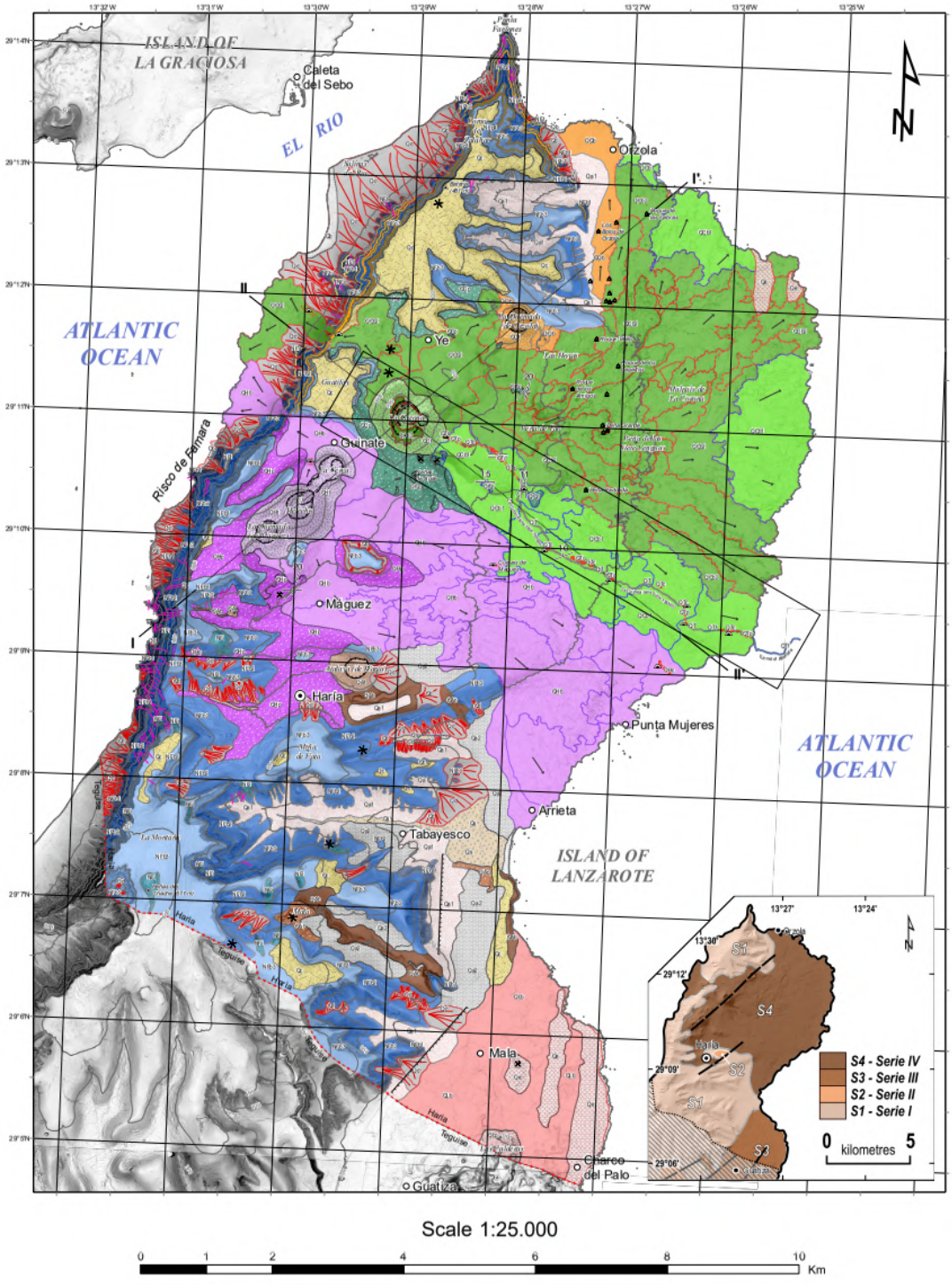


FIGURE 5.3: Geological map from Tomasi et al. (2023)

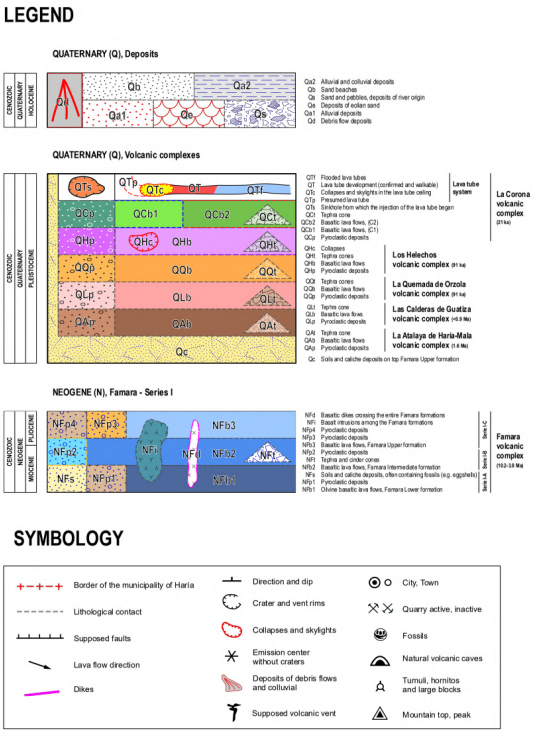


FIGURE 5.4: Legend from the Geological map of Tomasi et al. (2023) (Fig. 5.3

average width of 118 m and an average thickness of 4.9 m.
Geographical distribution of lava flows for different morphological dimensions that lava flows extending further away from the source have an automatically calculated length longer than flows located closer to the cone (Fig. 5.7). Lava flows located to the edges of the lava field, in the north and the south have on average higher widths than those located to the east, in the middle of the set. Thicker flows are located more frequently on the edges, in the north and the south, as well as close to the source, to the west. Overall, lava flows to the east, away from the vent and near the coastline are smaller and more numerous (Fig. 5.7).
The fractal dimensions of lava flow margins at La Corona range from 1.06 to 1.47 and average 1.23 (Fig. 5.8). Lava flows with higher fractal dimension (> 1.2) are located close to the vent or in the middle of the set whereas flows with margins with lower fractal dimension are found on the edges, to the north and the south.

## 5.4 AROMAS output on terrestrial example

The stratigraphic and morphometric output of AROMAS on a terrestrial set shows consistency between expected and automatically obtained results. Contrary to what was observed on Tharsis' lava flows, the topological sorting has yielded realistic results with the top units correctly located closer to the source. Consequently, the total length inferred through the path along the stratigraphic tree is correctly calculated. The difference in the number of flows (101 vs 424) and the overall lower complexity

of this set of lava flows yielded reliable results. Here, no quadrangles are used to map the different contacts, therefore, issues discussed in 4.4.1 do not arise. Overall, AROMAS displays strong performances on a terrestrial example and demonstrates its flexibility.

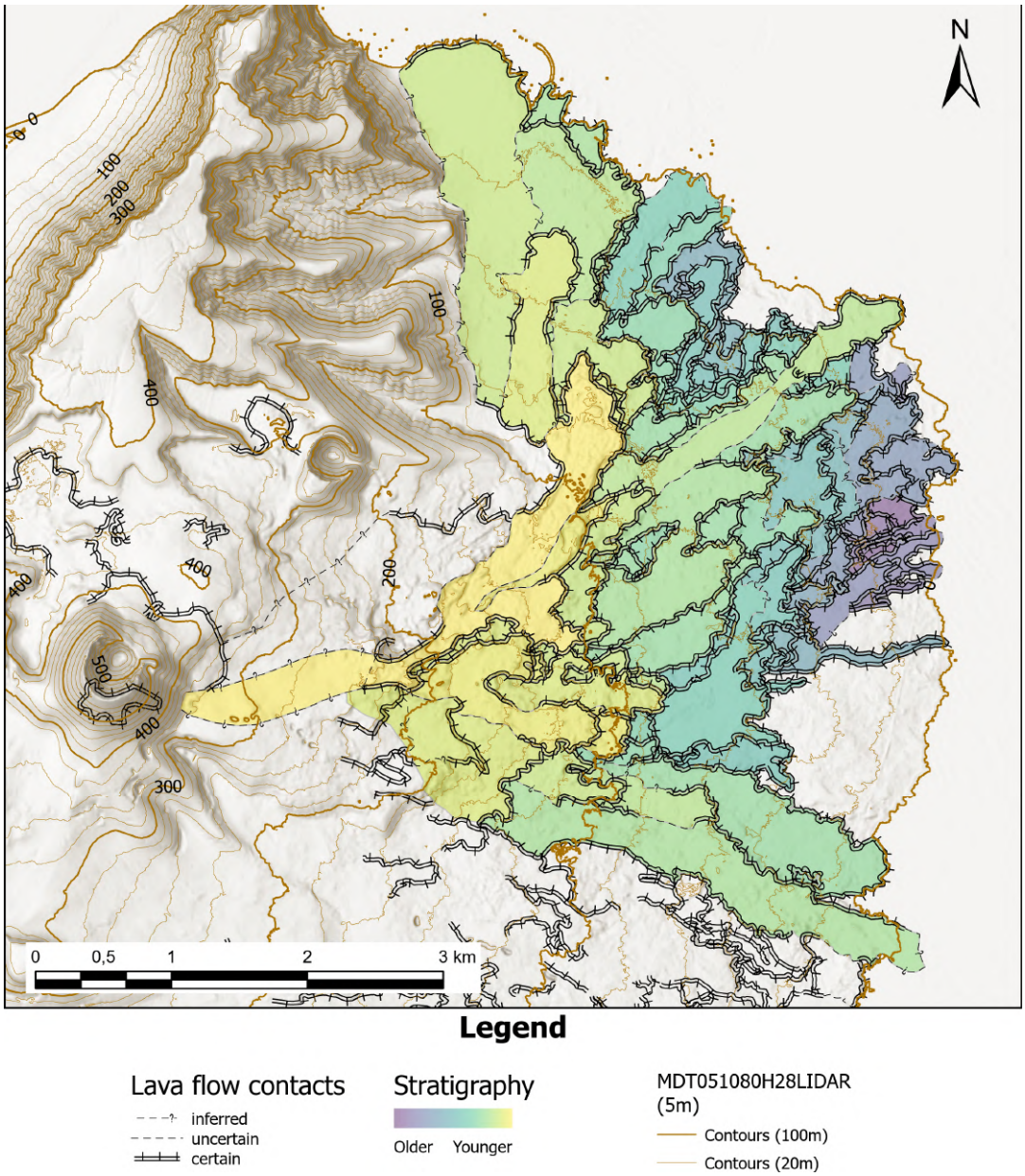


FIGURE 5.5: Stratigraphic map of la Corona lava flows over a 5m LiDAR derived hillshade.

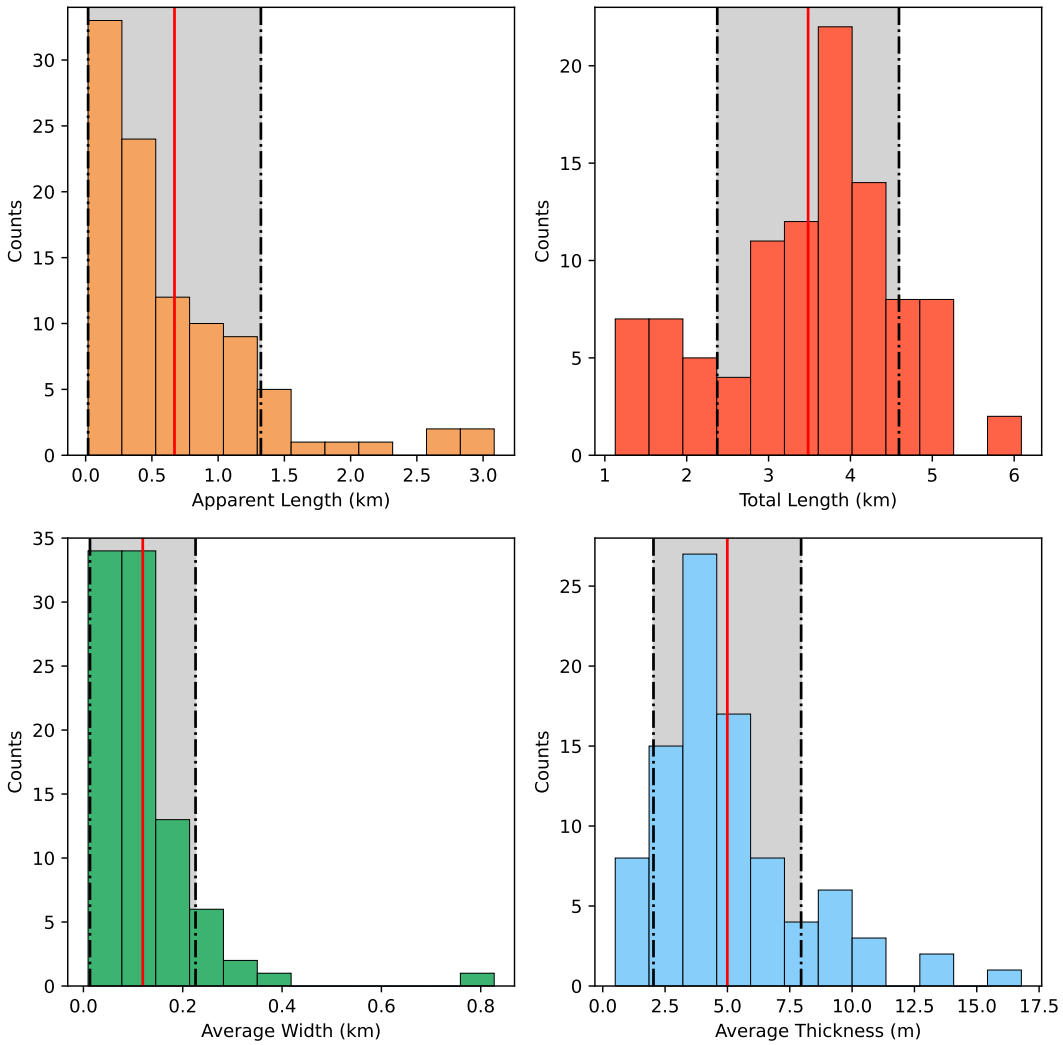


FIGURE 5.6: Histogram of morphometric results obtained through AROMAS on Lanzarote lava flows.

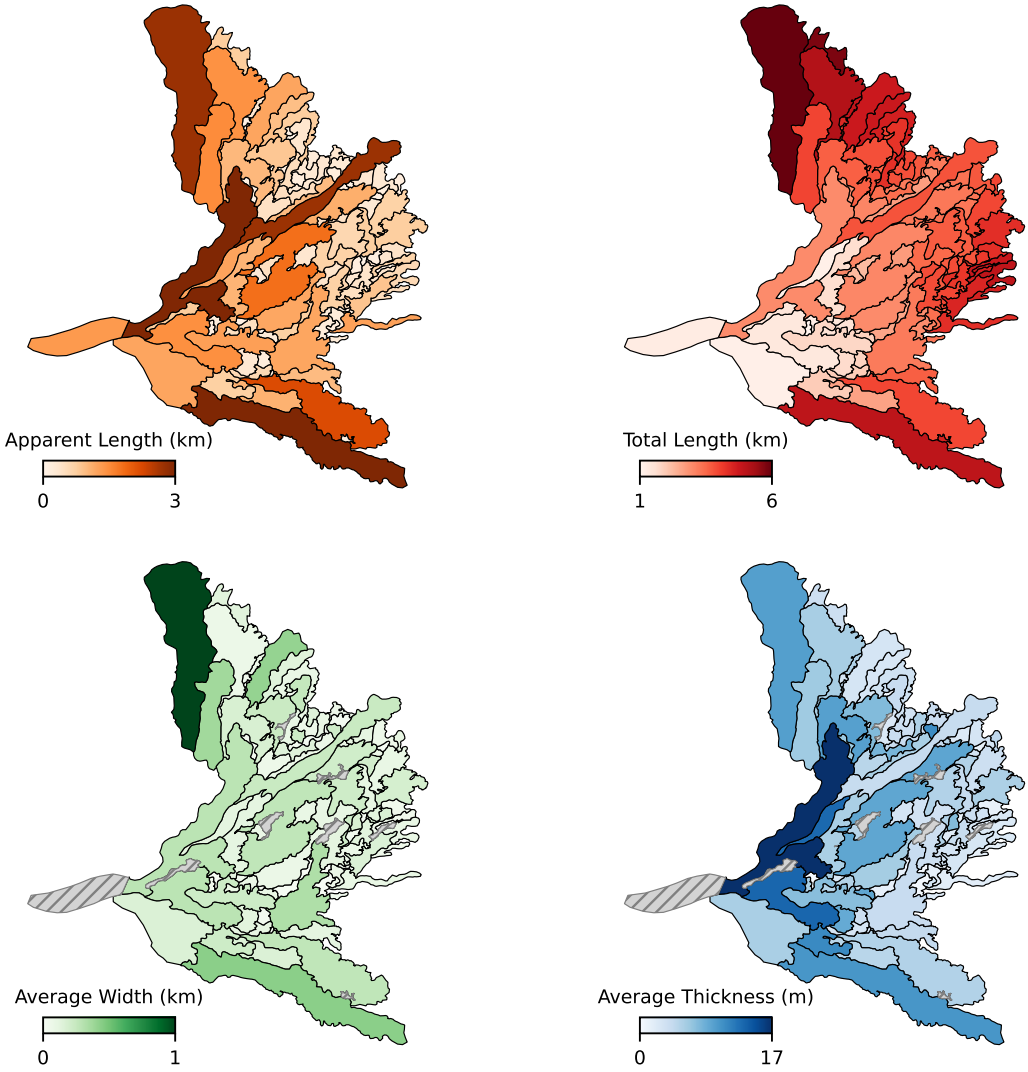


FIGURE 5.7: Map of lava flows generated by AROMAS with the value for each flow of apparent length, total length, average width and average thickness.

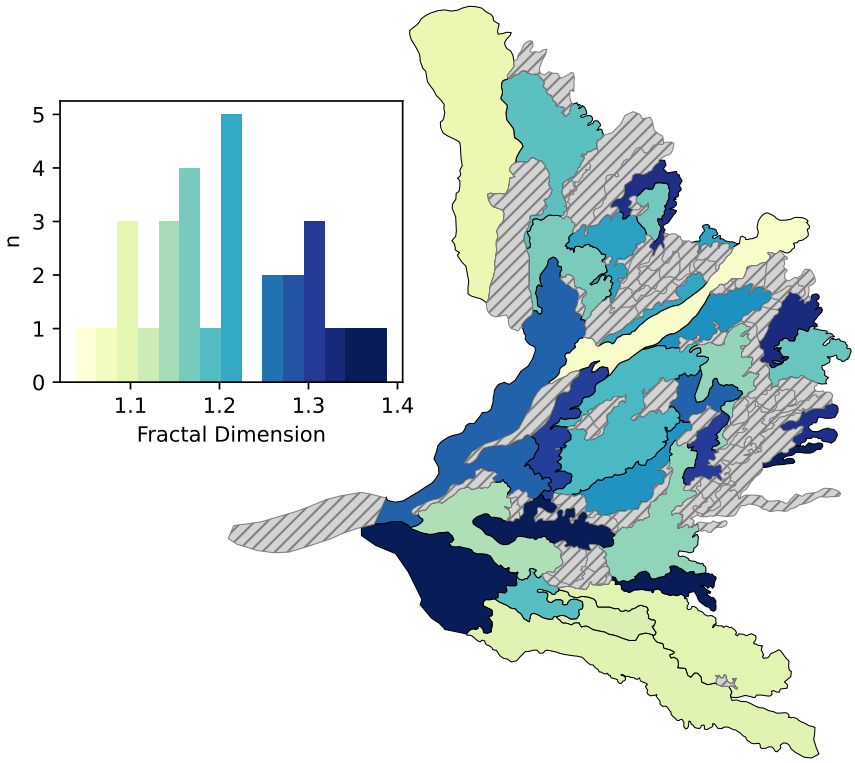


FIGURE 5.8: Map of average fractal dimension of lava flow margins. Missing values are represented in hatched grey.

# Chapter 6

# Explosive activity records in Noctis Labyrinthus

## Introduction

In the previous chapters, we have extensively discussed the effusive type of volcanic activity. However, evidence for explosive activity in the vicinity of Arsia Mons remains scarce, a common trend in Martian volcanic records. So far, we have described an extended effusive activity spanning 190-350 million years from 330 ± 60 Ma to 60 ± 20 Ma, originating from Arsia Mons' southern lava apron. These lavas cover older units, including more ancient lava emplacements and potential pyroclastic deposits. In addition to the thin dust mantling the surface of younger flows and the thicker and older loose material deposits found in an impact crater (Fig. 4.25), other potential deposits of pyroclastic origin have been found at Arsia Mons.
Surrounding collapse pits in the Arsia northern rift zone, Mouginis-Mark (2002) found evidence of a 50m-thick level of pyroclastic deposits (Fig. 1.5B). Given the lifespan of Arsia Mons and the other Tharsis volcanoes, similar deposits, continuous or episodic, could have formed during Arsia Mons' history. Using the Mars *Global Circulation Model* of Laboratoire de météorologie dynamique (Paris), Kerber et al. (2013) demonstrated that a year-long eruption at Arsia Mons associated with a

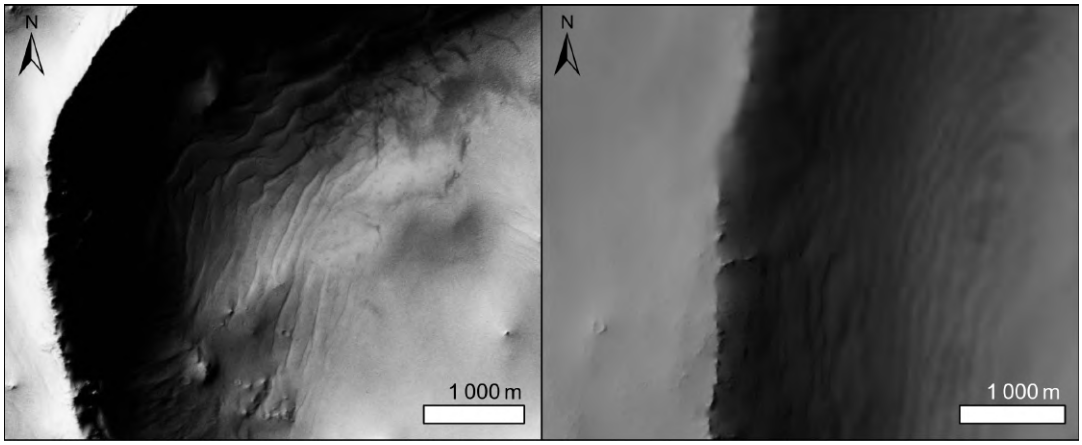


FIGURE 6.1: Bedform-like features found on a crater floor and walls near Arsia Mons as well as on Noctis Labrytinthus slopes.

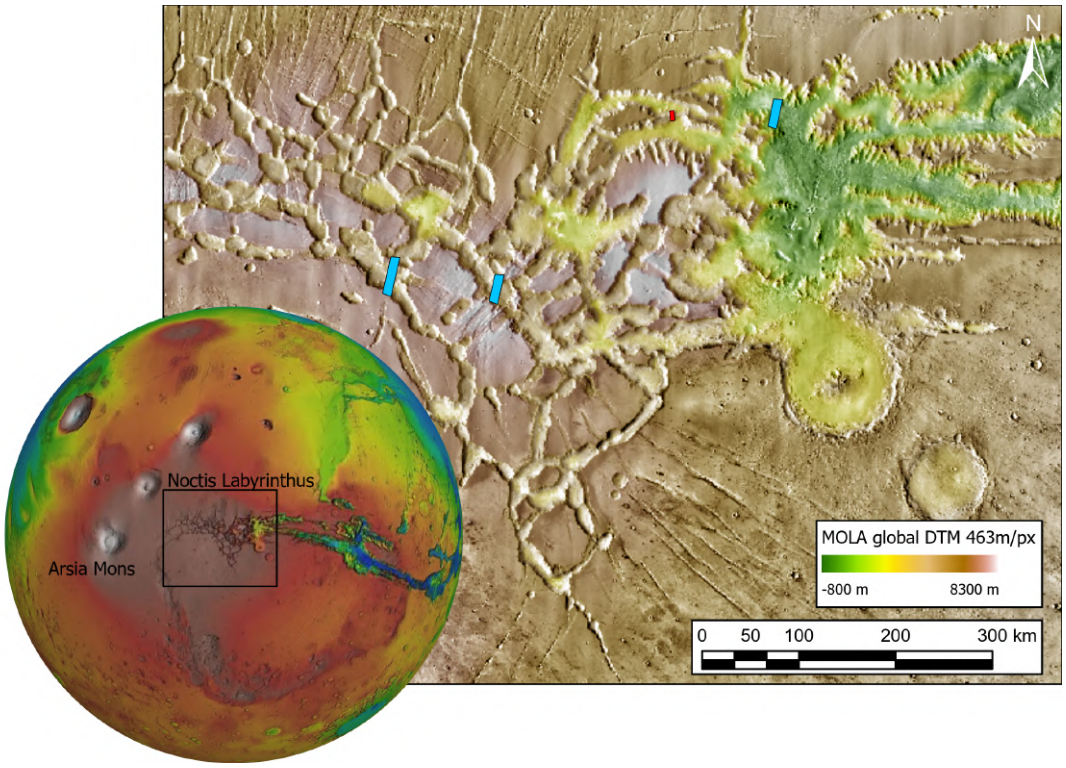


FIGURE 6.2: The Noctis Labyrinthus region with the location of CaSSIS (in blue) and HiRISE (in red) DTM footprints used to study the morphology of BLF during this work (THEMIS Day-IR with coloured elevation from MOLA.)

million km$^3$ of material could have formed tens to hundreds of meters-thick deposits as far as Valles Marineris, over 1500 kilometres away. Such deposits, however, may have been formed provided that the atmospheric pressure was one to three orders of magnitude higher than today to allow long-distance airborne transport, which was the case only more than 3 billion years ago (e.g., Forget et al., 2013).

Consequently, these putative deposits should be stratigraphically lower than the relatively recent lava flows studied so far. Because volcanic activity at Tharsis has waned throughout Mars' geological history, ancient explosive deposits should have extended further away than lava flows deposited in the last tens to hundreds of millions of years. Evidence for such explosive deposits may therefore be sought far away from the main volcanic constructs, in areas where they are less likely to be covered by more recent lava flows. The material mantling the floor of the impact crater discussed above (Fig. 4.25) pre-dates the emplacement of the late Amazonian lava flows SE of Arsia Mons. In CTX images, bedform-like features (hereafter referred to as BLF) are shaped from this material, but their aeolian bedform nature cannot be inferred given the lack of available high-resolution DTMs.

The Noctis Labryinthus region is a complex system of grabens and canyons, located on the northern side of Syria Planum, west of Valles Marineris and east of Tharsis Montes (Fig 6.2 - Bistacchi et al., 2004; Kling et al., 2021; Mège et al., 2003). Fortunately, BLF are frequently found on Noctis Labryinthus slopes (Fig. 6.1), where data are available to carry out a more detailed investigation. To this day, these peculiar

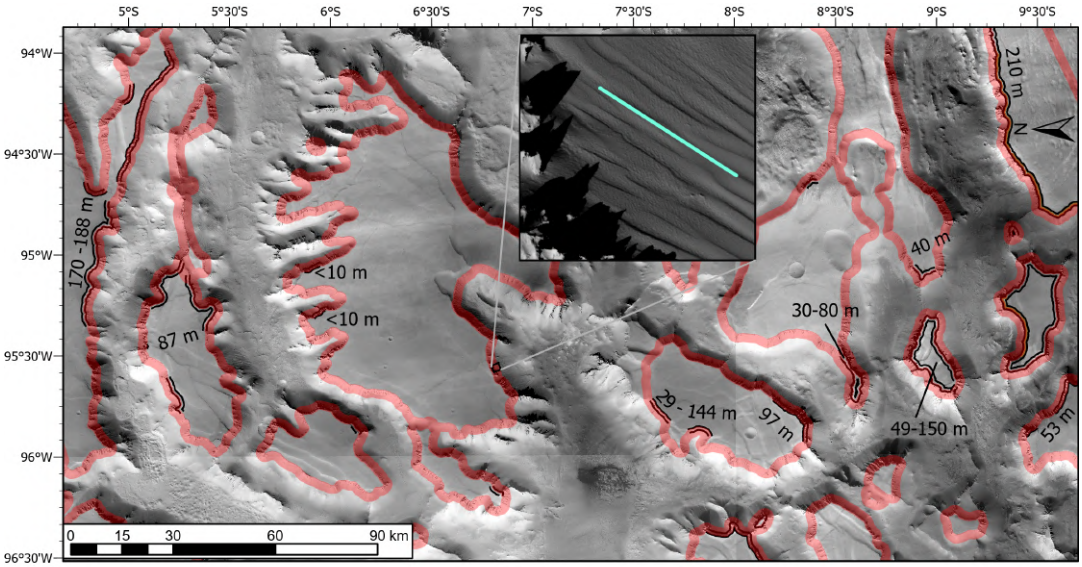


FIGURE 6.3: Area extent where BLF distribution was studied. Red areas indicate sections generated along cliffs, 2 km downslope, of plateaus and mesas. For each slope section, a line was drawn to indicate the presence or absence of BLF features, and, if present, record their average orientation in that section. Double-stroked black lines indicate an outcrop of layered deposits as well as where possible, their thickness was measured.

features have not been described in the literature and here, CaSSIS DTMs are used to provide a first description and interpretation.

## 6.1 Datasets and methods

### 6.1.1 Data

CTX, HiRISE, and THEMIS images were used to identify bedform-like features and study their context of emplacement. Three CaSSIS DTMs (C1, C2, C3) and one HiRISE DTM were used to study the shape of the features and measure their morphological characteristics. Additionally, 3 CTX DTMs were generated to support the analysis of the emplacement context of these features. The description and processing steps of these datasets can be found in chapter 2. Image IDs used to generate DTMs can be found in Table 6.1.

### 6.1.2 BLF distribution

The data were imported into ArcGIS Pro in an equirectangular projection. To assess the spatial distribution of the BLF on slopes as well as their orientation, 1 km wide and 2 km long sections were generated around the cliffs of mesas and plateaus surrounded by potentially BLF-covered slopes in a 350 by 200 km area of interest (Fig. 6.3). For each section, their presence and orientation were indicated by drawing a single line within the section giving the general orientation of the bedforms locally.

### 6.1.3 BLF morphometrics

The slope aspect of each section of the buffer zone was estimated using MOLA Global DTM. As walls in the region could display specific orientation in the first place, the frequency of slopes covered by BLF derived from such an approach would be biased. To account for this, the frequency of slopes covered by BLF was normalised to the general distribution of slope aspect distribution.
DTMs derived from a HiRISE and 3 CaSSIS stereo-pairs were used to study the shapes of the BLF and retrieve their height, width and steepness whereas spacing was measured on DTM-derived orthoimages. In practice, crestlines were digitised and interpolated on DTMs. As most features studied here are located on sloping surfaces a back-stripping filter (Hugenholtz & Barchyn, 2010) was applied to remove the topographic signal of the main slope on the DTM and virtually place the smaller-scale features on a flat surface, while preserving their topographic signature.

## 6.2 Results

### 6.2.1 BLF distribution

Statistical analysis of BLF geographic distribution shows that they are more frequently found on south-facing walls in Noctis Labyrinthus (Fig. 6.4B). Normalised distribution based on general wall aspect distribution displays similar trends, with a high frequency of BLF from SW to SE-facing walls (up to 80% per bin - Fig. 6.4C), and low to null on northwards slopes even though the latter are well-represented in the area of study (over 40% - Fig. 6.4A). BLF in the area of study have a NNE-SSW orientation (Fig. 6.4D).

### 6.2.2 BLF surface characteristics

The surface of the BLF is covered by a light-toned loose material displaying a honeycomb pattern and deltoid-shaped features. At the foot of the walls, bedforms are usually exposed, displaying a lower albedo in CTX and HiRISE imagery, and appear to be heavily cratered (Fig. 6.5). Transverse Aeolian Ridges (TARs - e.g. Day and Zimbelman, 2021) are found on chasma floors at the foot of the walls, where they cover topographic lows formed by the BLF (Fig. 6.5C), suggesting the latter predate TARs formation. In some instances, the features are lobate and show striking similarities with periglacial features known as solifluction lobes (Fig. 6.6 - Kling et al., 2021; Price, 1974).

### 6.2.3 Context of emplacement and Layered Deposits

Mesas and plateaus in the area around which slopes where BLFs are found are often mantled by capping layered deposits (Fig.6.7). This unit lies over a hard rock basement and displays short-scale variations of apparent thickness, ranging from a few

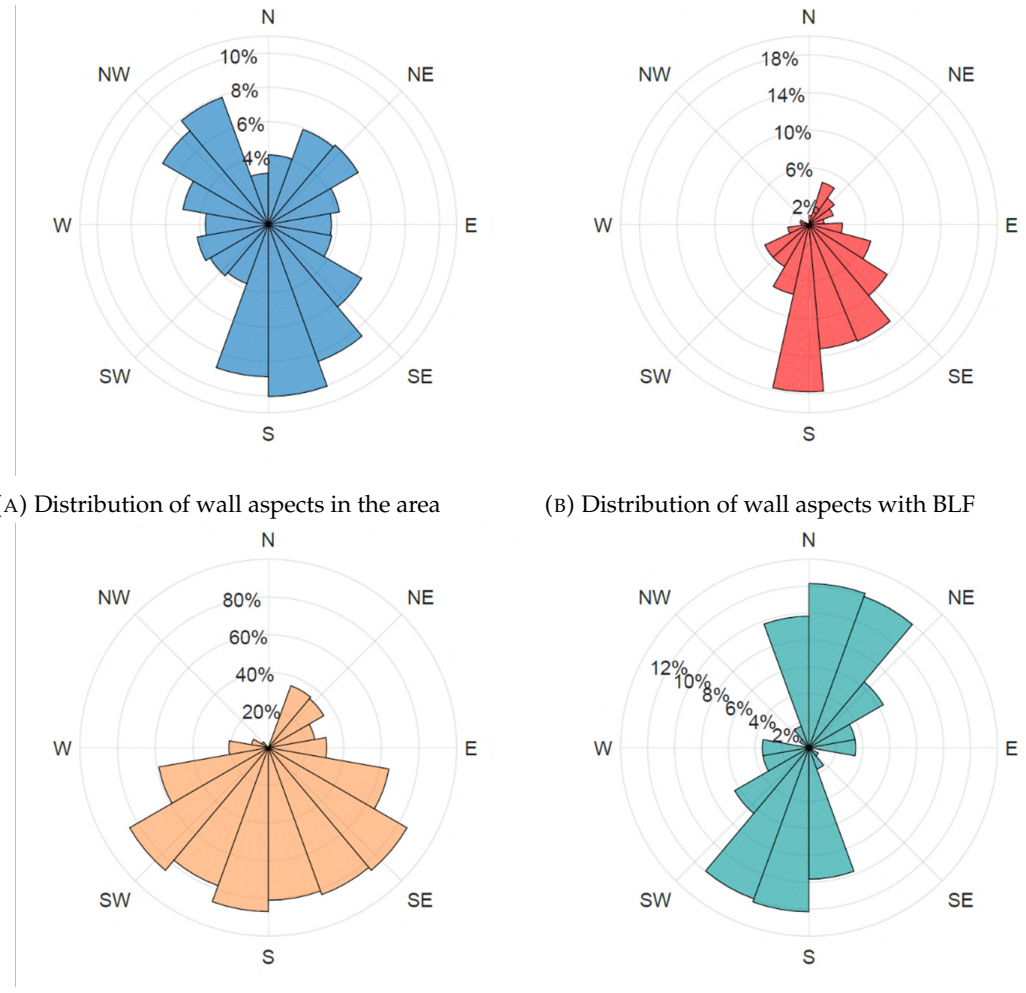


(A) Distribution of wall aspects in the area

(B) Distribution of wall aspects with BLF

(C) Percentage of walls with BLF

(D) Distribution of BLF azimuths

FIGURE 6.4: Rose diagrams of BLF statistical distribution with respect to the aspect of walls.

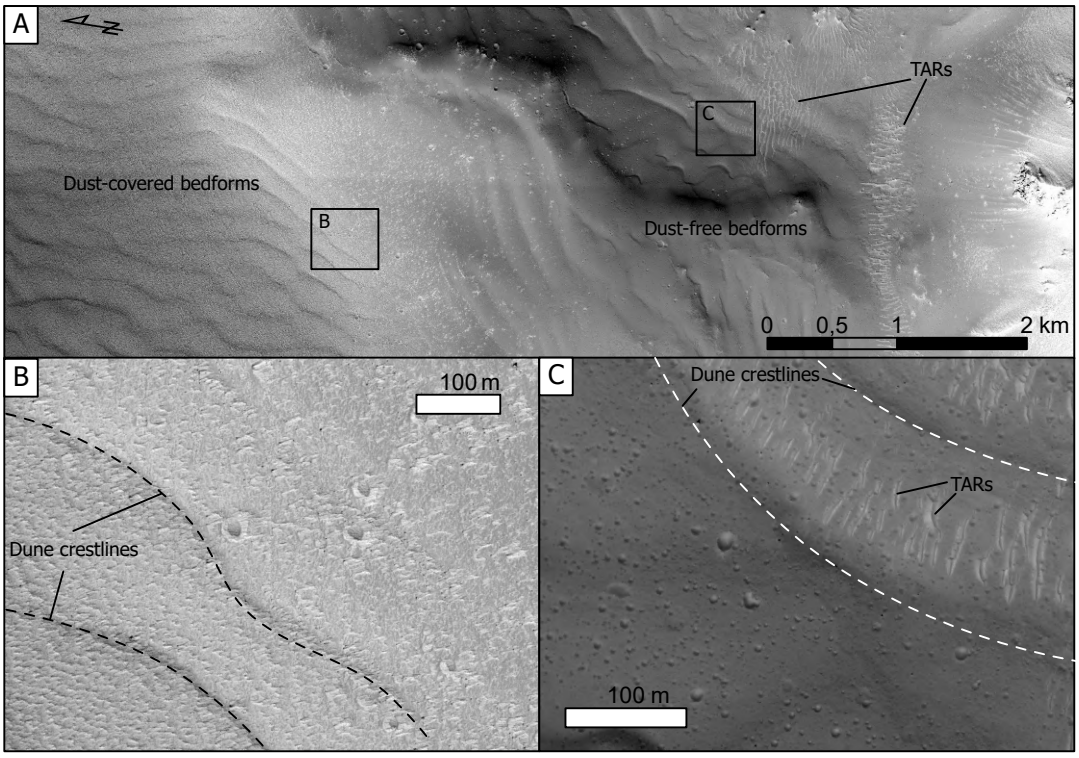


FIGURE 6.5: BLF located on a slope. **A**: General view of the features with the northern part covered by light-toned material and the exposed part in the South, downslope. **B**: Topographic changes induced by BLF are visible under the light-toned material. **C**: Exposed bedform surface with high-density of impact craters. HiRISE (ESP_046251_1710)

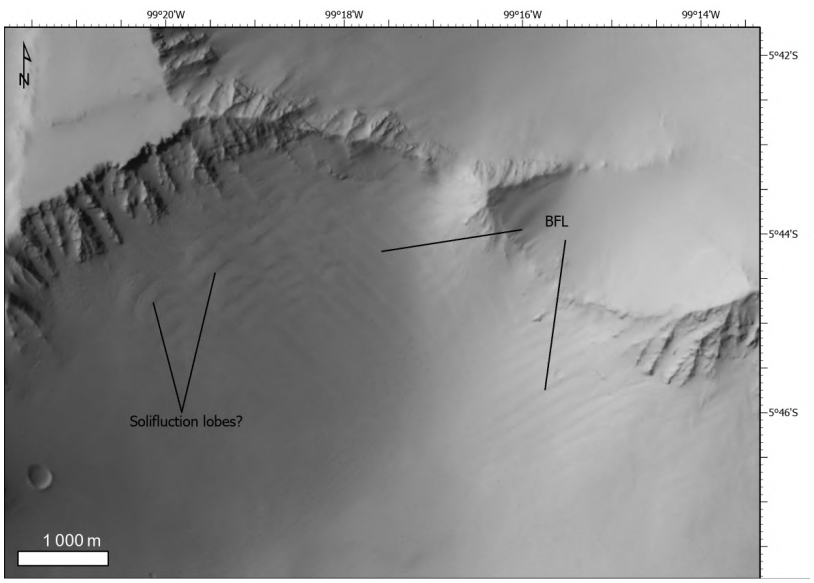


FIGURE 6.6: Slope covered by solifluction lobes and BLF, forming from the same material. Solifluction lobes are perpendicular to slope direction as they are gravity-driven.

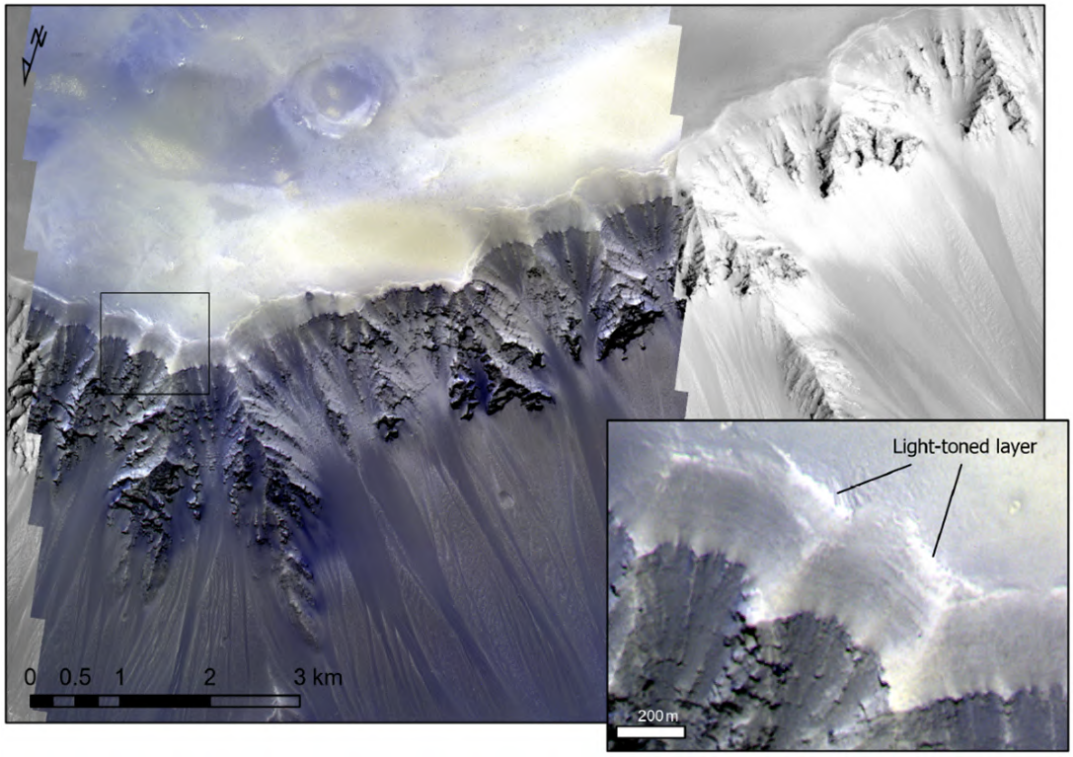


FIGURE 6.7: Light-toned layered deposits on top of a plateau. CaSSIS image MY35_012306_190_0 (NIR-RED-BLU composite) and CTX Mosaic.

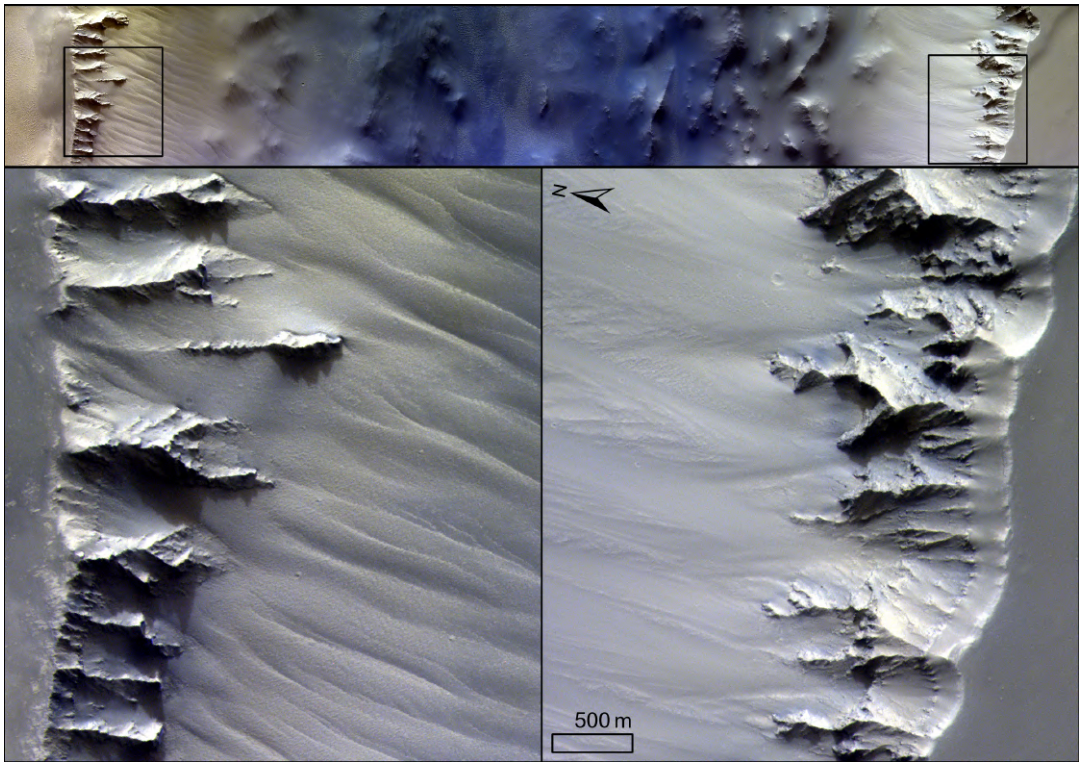


FIGURE 6.8: South and north-facing walls displaying reworked deposits and BLF, and exposed outcrop of layered deposits respectively. CaSSIS MY36_018051_190_0. NIR-PAN-BLU colour composite.

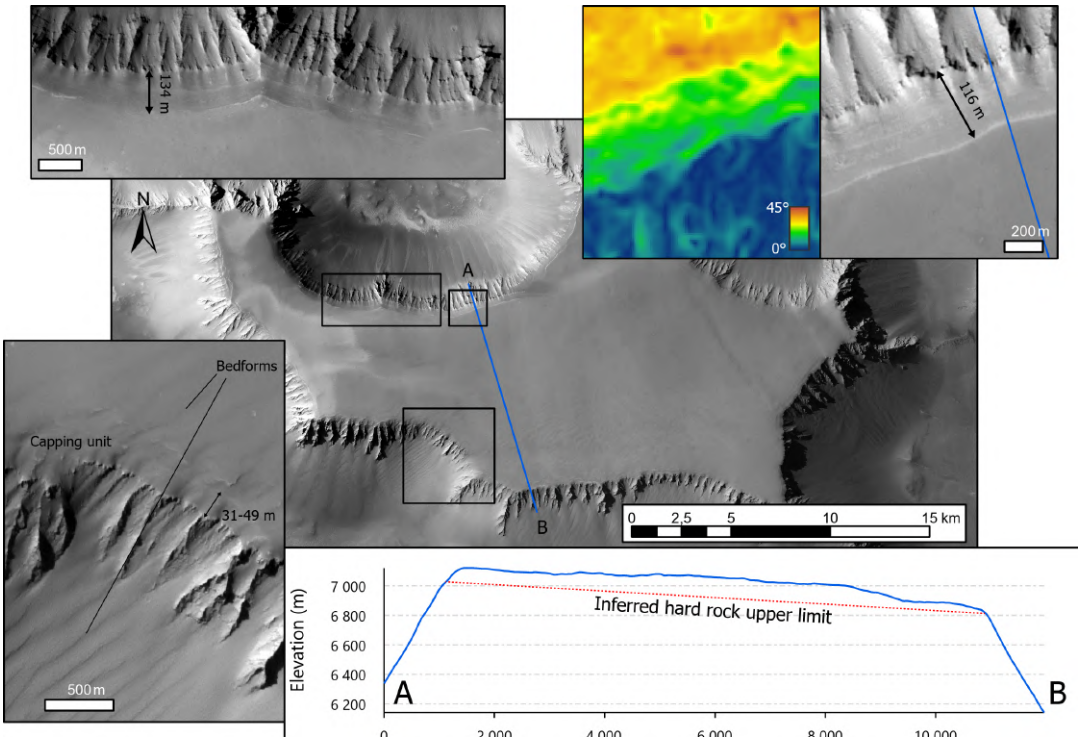


FIGURE 6.9: Close-up view on a mesa with a >100 m thick layered deposits with exposed outcrop to the north, and reworked into BLFs to the south. The colour map is a slope map. Analysis of the generated CTX DTM shows a slope angle break between the layered deposits and the rock basement. CTX DTM: CTX_010226_1765_053609_1764

tens of meters to >300 m (Fig. 6.3). Apparent thickness variation is often associated with paleo-topographic variations and central mesas in the ROI display less to no visible outcrops.

North-facing outcrops also display internal layering (Fig. 6.7, 6.8, 6.9) whereas none is visible on deposits covering the top of south-facing walls (Fig. 6.9). A slope angle map derived from CTX DTM reveals a slope break between the rock basement (>35°of slope) and the layered deposit outcrop overlaying it, with a slope angle of 21± 3°(Fig. 6.9). At the top of plateaus and mesas, capping deposits are frequently reworked into BLF (Fig. 6.9) indicating they could be made from the same material. BLFs are found to extend from the flat plateau surface to the slopes.

### 6.2.4 BLF features morphology

Results on spacing, height, and width measurements of the BLF are reported in Table 6.1. Cross-sections of the BLF in each area covered by the DTMs show that they display an asymmetric profile characteristic of aeolian bedforms (Fig. 6.10, 6.11, 6.12, 6.13). Leeward, windward, and main surface slope angles are reported in Table 6.2. The top of the bedforms visible on the HiRISE image displays secondary features (Fig. 6.13) which appear to be yardangs on the visible image. Aeolian bedforms found on C1 and C2 are on average three times higher than those studied on C3 for the same spacing and a slightly larger width (Table 6.1). Bedforms visible on HiRISE

| DTM/Image ID | N* | Spacing (m) | Height (m) | Width (m) |
|---|---|---|---|---|
| MY34_004777_354 (C1) | 17 | 155 ± 43 | 1.6 ± 0.6 | 148 ± 42 |
| MY34_003882_351 (C2) | 52 | 169 ± 54 | 1.7 ± 0.9 | 152 ± 54 |
| MY34_005175_351 (C3) | 13 | 173 ± 21 | 0.5 ± 0.2 | 125 ± 24 |
| ESP_029504_04693_1745 (HiRISE) | 29 | 244 ± 21 | 9.5 ± 1.2 | 210 ± 46 |

TABLE 6.1: Image IDs of DTMs with the number of bedforms, their average spacing, height, and width on each of them respectively.

| DTM Image ID | Substratum slope (°) | Substratum aspect | Leeward slope (°) | Windward slope (°) | Paleo-wind direction |
|---|---|---|---|---|---|
| C1 | 20.2 | N45 | 3.6 ± 1.1 | 1.7 ± 0.3 | ESE |
| C2 | 20.7 | N190 | 1.8 ± 0.5 | 1.0 ± 0.2 | SE |
| C3 | 26.8 | N212 | 0.9 ± 0.2 | 0.5 ± 0.2 | SSE |
| HiRISE | 24.4 | N160 | 14.2 ± 0.9 | 6.3 ± 1.1 | N |

TABLE 6.2: Substratum characteristics on each DTM, with bedform leeward and windward slope values as well as inferred paleo-wind direction.

have a height order of magnitude greater than bedforms found on CaSSIS DTMs while their width and spacing are only 50% higher (Table 6.1).
Bedform asymmetry is more pronounced on bedforms located on C1 and HiRISE (leeward/windward ratio of 2.14 and 2.27 respectively – Table 6.2) than those visible on C2 and C3 (ratio of 1.79 and 1.71 respectively – Table 6.2). Paleo-wind direction inferred from leeward/windward slope identification suggests a downslope transport on C2 and C3, and parallel to the slope to downslope on C1 (Table 6.2). The paleo-wind direction of bedforms on the HiRISE DTM suggests an upslope transport.
Fig. 6.14 shows a linear correlation between bedform width and height for C1, C2, and C3 combined, and for the HiRISE DTM. Spacing is also correlated to height for bedforms visible on C1 and C2 combined, on C3, and on HiRISE

## 6.3 Discussion

### 6.3.1 Nature and emplacement of BLF

The asymmetric profile of the features studied here confirms that they are aeolian paleo-bedforms. Their relationships with the capping unit on plateaus and mesas indicate they could correspond to non-consolidated material transported by the wind from the plateau surface to the surrounding slopes. This hypothesis is supported by the fact that they are found more frequently on southern-facing slopes, indicating a regional transport, from north to south (Fig. 6.4), progressively covering the internal layering on the outcrop and the underlying slope (Fig. 6.9). Paleo-wind orientation inferred from CaSSIS DTMs (Fig. 6.10, 6.11, 6.12, & Table 6.2) is consistent with a downslope katabatic wind progressively carrying the loose material particles from the top of the plateau downslope. However, the orientation of bedforms located on

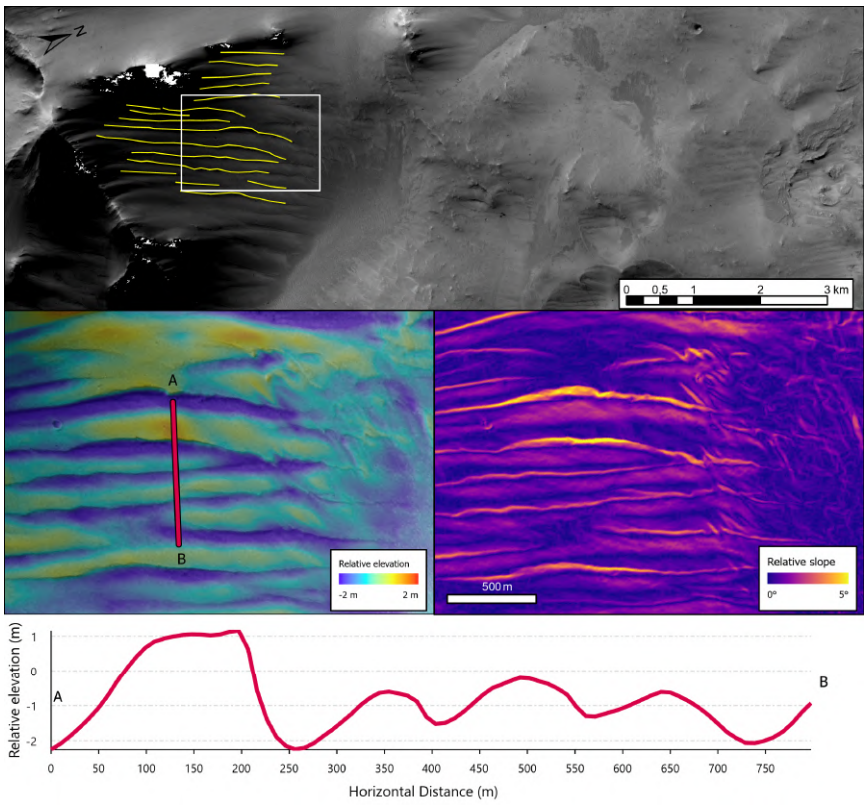


FIGURE 6.10: Topographic analysis of CaSSIS DTM C1

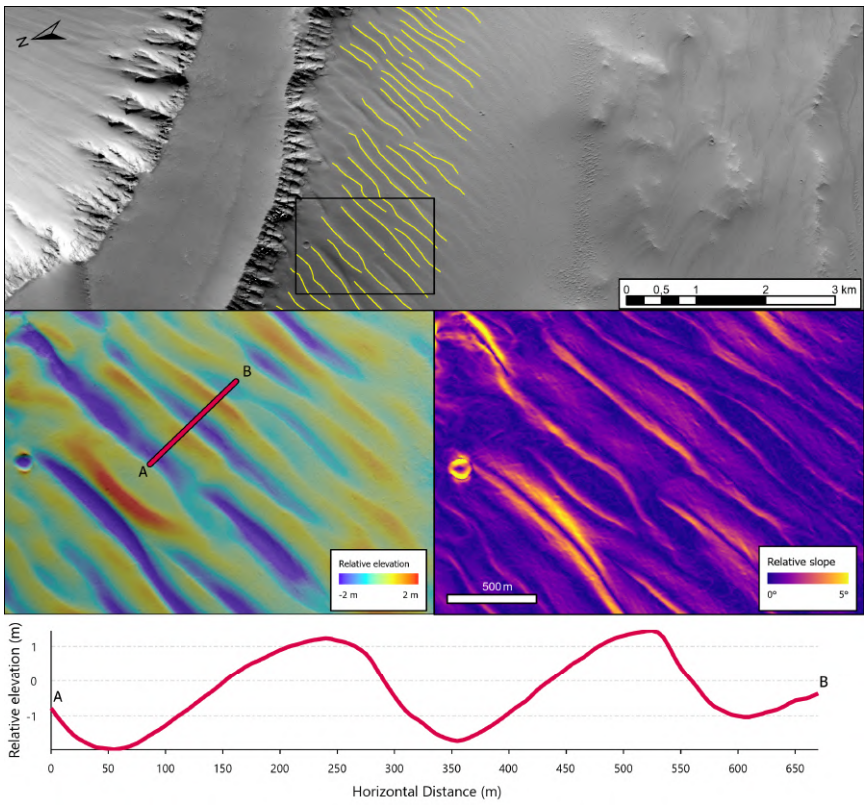


FIGURE 6.11: Topographic analysis of CaSSIS DTM C2

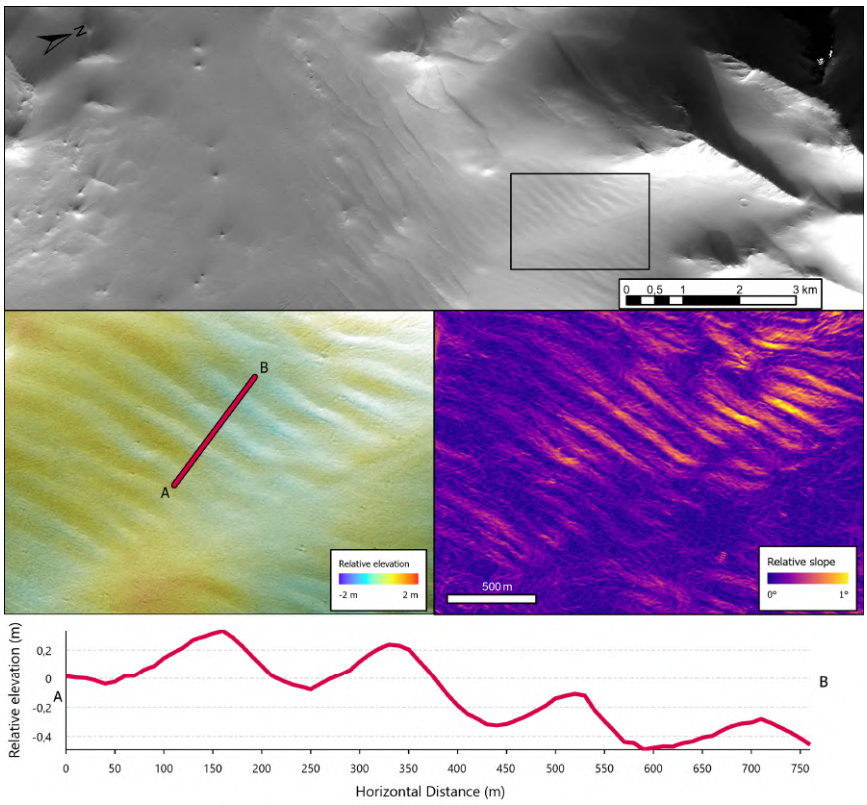


FIGURE 6.12: Topographic analysis of CaSSIS DTM C3

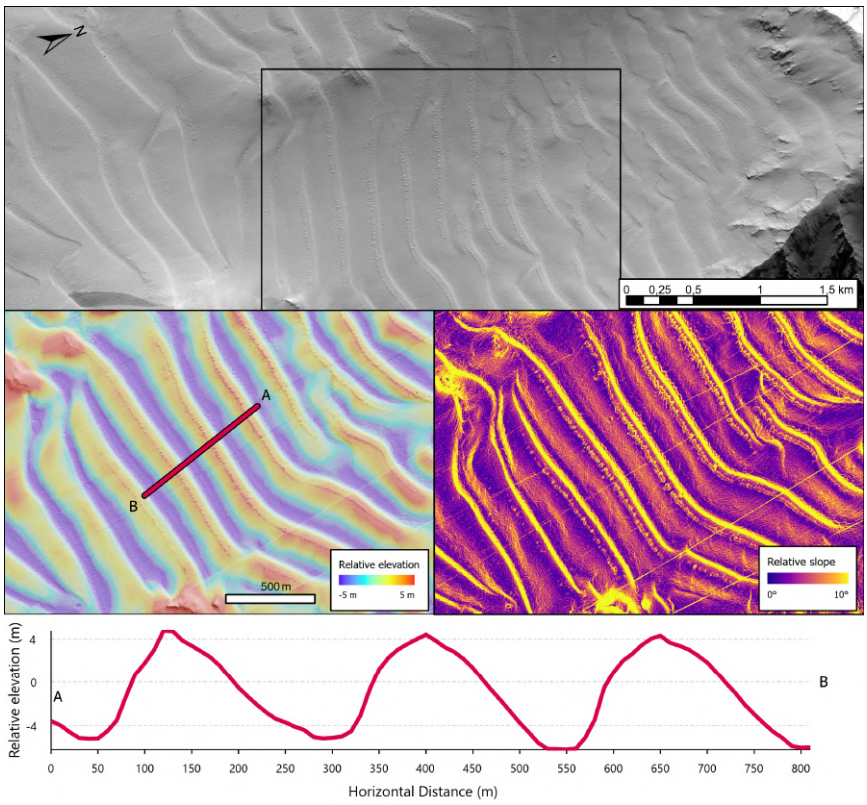


FIGURE 6.13: Topographic analysis of HiRISE DTM

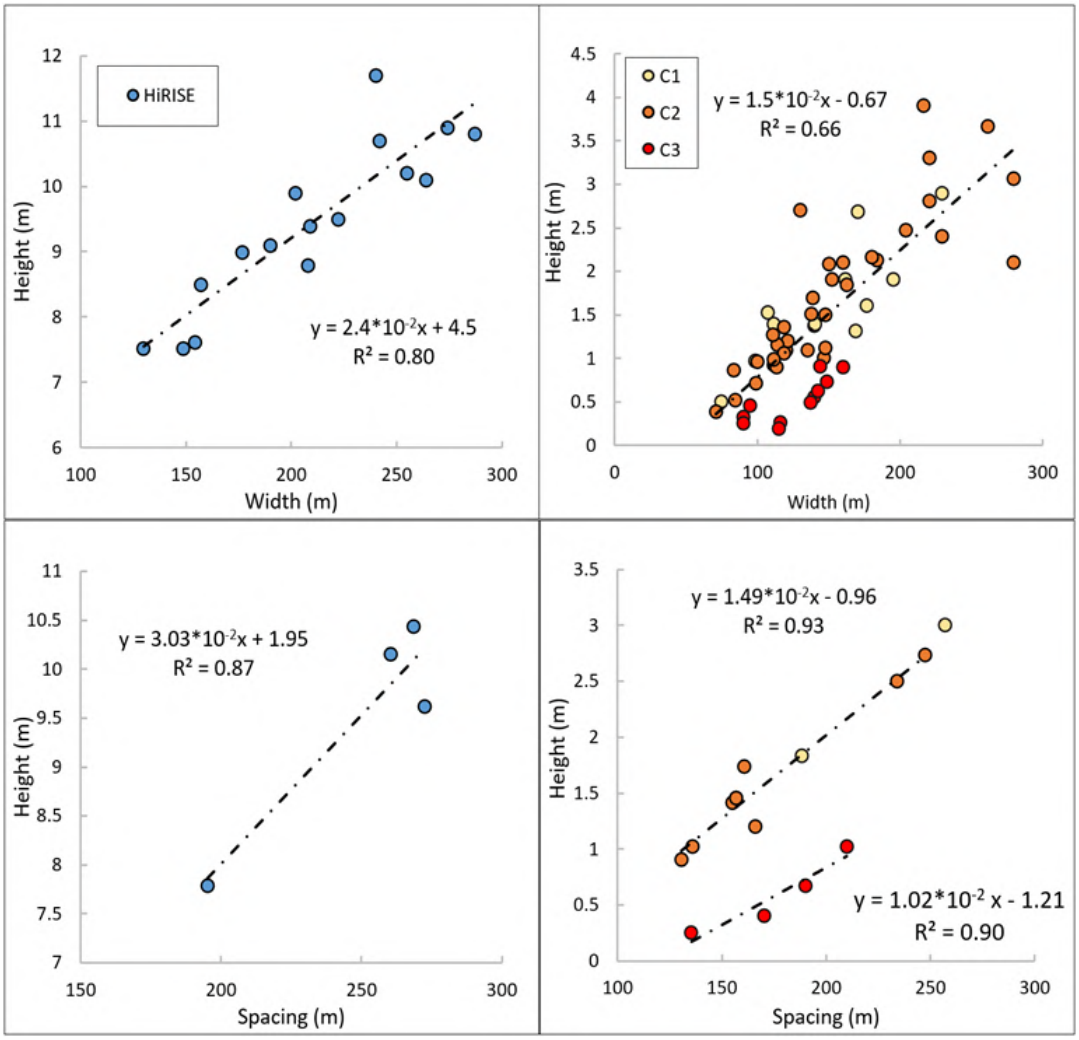


FIGURE 6.14: Paleo-bedforms morphometrics on the HiRISE DTM and C1, C2, C3 combined. **Top**: Height-to-width ratio for individual bedforms. **Bottom**: Height to spacing relationship; spacing is measured between bedforms of different heights. For each height group, average spacing and height are calculated.

the HiRISE DTM indicates an upslope transport suggesting a more complex story implying several stages of emplacements from different sources.
Bedform erosion visible on the HiRISE DTM and the high density of impact craters on exposed bedforms (Fig. 6.5) suggests that they are no longer active. Relationships between aeolian bedforms and TARs also lean towards an ancient emplacement age. Variations in height between bedforms observed on the CaSSIS C1, C2 and C3 DTMs compared to those covered by HiRISE could be related to differences in initial material supply, wind direction, frequency, speed, or even erosion rate before and after cementation occurred. Spacing differences between bedforms on CaSSIS and bedforms on HiRISE are less than 50%, while height differences are one order of magnitude. Assuming the spacing-to-height ratio was initially the same, this could indicate a higher abrasion rate of the bedforms in the area observed on the CaSSIS images. Another possibility is that the aeolian material accumulated for a longer time in the area covered by the HiRISE image. A third hypothesis is that initially of similar height in both areas, the bedforms observed on the CaSSIS images were less cemented. The upper part would have been remobilized by wind, in contrary to the area seen by the HiRISE image, which would have been cemented to the top, or at least to a higher level in the dune.
Post-emplacement cementation could result from groundwater and mineralisation, as in paleo dunes in Valles Marineris (Chojnacki et al., 2020). The formation of ice thought to fill the pores in the bedform material requires environmental conditions different from the present conditions, and is prone to liquid water molecule deposition, then percolation, prior to freezing. These conditions require temperatures above 0°C and increased atmospheric pressure. Such conditions would therefore explain the deposition of ash in Noctis Labyrinthus, as well as the condensation, deposition, percolation, and liquid water in these deposits. Obliquity changes to present-day conditions would freeze the water and immobilise the bedforms; the succession of freezing/thawing cycles arising from the succession of climatic cycles between pyroclastic material deposition and today would control current bedform height.

### 6.3.2 DTM comparison and CaSSIS performance

As there is a lack of overlap between the datasets, one may argue that variations in bedform height observed may also be explained by differences in performance between the different instruments. Further work should focus on identifying a spot covered by stereo-pairs from both instruments in order to really compare their derived DTMs.
Regardless of this shortcoming, CaSSIS DTMs refined by photogrammetry used here show that are suitable to study short-scale landforms, despite footprint size being larger and resolution coarser than DTM generated from HiRISE stereo pairs. In this respect, photoclinometric processing of DTMs generated by stereoscopy appears to be an ideal approach to ground morphometric analysis.

### 6.3.3 Layered deposit origin

The layered deposits found in eastern Noctis Labyrinthus are morphologically similar to the light-toned layered deposits (LLDs) found in Valles Marineris and described by several authors (Le Deit et al., 2010; Weitz et al., 2008). One of the potential origins for these deposits proposed was that they are of pyroclastic origin.
Differential erosion highlighted by a slope angle break (Fig. 6.9) suggests that they are made of a weaker material than the underlying rock basement, which is consistent with a volcanic airfall origin. At Arsia Mons, pyroclastic emplacement described by Mouginis-Mark et al. (2022), located in the NE of the edifice, share similar morphological characteristics with those at Noctis Labyrinthus: a light-toned layered deposits overlaying a massive rock at a lower angle of response. The Arsia Mons deposits discussed here are located on the edifice itself and could correspond to different emplacements in terms of source and chronology than those found on Valles Marineris and Noctis Labyrinthus plateaus. However, Kerber et al. (2013) demonstrated that, under thicker atmospheric conditions, explosive activity at Tharsis may have formed hundreds of meters thick deposits as far as Valles Marineris. Such atmospheric conditions requirements are compatible with the groundwater cementation hypothesis.
The presence or absence of paleo-bedform frequency on the plateaus may be explained by changes in capping unit consolidation or local variations of paleo-wind velocity. Morphometrics of the bedforms indicate a mobilised layer of at least a few meters on CaSSIS, compared to the tens to hundreds of meters thick LLDs covering plateaus, showing that the LD unit may only be or have been partially cemented.
The light-toned material covering most of the bedforms and plateaus (Fig. 6.5) shows a resemblance to the one observed and described by Runyon et al. (2021). This material displays strong similarities with dust aggregates commonly found at Tharsis Montes (e.g. Bridges et al., 2010) and Syria Planum (Runyon et al., 2021), and is thought to be of volcanic origin as well, although likely more recent.
As proposed by Le Deit et al. (2010), LLDs found in Valles Marineris and Noctis Labyrinthus could also consist of dust/ash mixed with ice particles. The presence of ice in the subsurface would provide a reservoir that might have fed the valley networks and sinuous ridges observed on Valles Marineris plateaus (e.g.Chapman et al., 2010; Le Deit et al., 2010) which would result from thawing episodes during higher obliquity periods during which liquid water was stable at the surface. Such an ice-pyroclastic material mixture would provide a suitable material composition for the observed development of the solifluction lobes (Fig. – Kling et al., 2021). Slope angle differences between LD outcrops and underlying rock basements (Fig. 6.9) suggest a lower than usual slope surface material viscosity, which ice can contribute to reducing. Ice is thought to have played a key role in shaping slope landforms in Valles Marineris too (Kite et al., 2016; Makowska et al., 2016; Mège and Bourgeois, 2011). These findings highlight a strong imprint of subsurface ice in the development of equatorial landforms over a region of considerable size.

2

# Chapter 7

# Discussion and Conclusion

## 7.1 Discussion

### 7.1.1 Reconstructed stratigraphy

The results show that recent effusive activity occurred simultaneously at Arsia Mons around the lava apron and within the caldera. Previous studies showed that this fluid lava outpouring episode follows an earlier episode of more explosive activity (Ganesh et al., 2020; Mouginis-Mark, 2002). Stratigraphically, the corresponding pyroclastic deposits should be located below the lava flows mapped in this work. Results from impact crater retention ages show ages as old 660 ±100 Ma for a flow located southeast of the study area (Fig. 4.19). The thin atmospheric density during the late Amazonian period hardly sustains a stable ash plume (Glaze & Baloga, 2002), ruling out airborne transportation to long distances away from the vent (Kerber et al., 2013). This loose material was identified in this work in an impact crater and seems to have been reworked into paleo-bedforms (Fig. 4.25).
Similar paleo-bedforms are observed as far as Noctis Labrytinthus. Their presence at such a long distance from the Arsia volcano (or any other giant Tharsis volcanic edifice) indicates a high pyroclastic deposit dispersion and requires deposition during a period of higher atmospheric pressure. The LLDs in Noctis Labyrinthus and Valles Marineris are sometimes associated with the paleo-bedforms could be the source of the latter. An extensive study of their location and variations of thickness could provide further insights into their origin. An airborne pyroclastic deposit originating from Arsia Mons or other Tharsis volcanoes would show a decreasing thickness away from the source. Since no outcrop exposing the internal layering can be found in western Noctis Labyrinthus compared to the eastern part (e.g., Fig. 6.7), this may suggest a source located in a different region. Further work and mapping focused on the contact between Amazonian lava flows and Noctis Labyrinthus could provide more insights into the origin of these deposits.

### 7.1.2 Effusive rate

The morphological characteristics of the lava obtained through AROMAS allow to estimate the total volume of erupted material for this set of flows. Although improvements could still be made on the computation of length, width and thickness (see sections below and 4.4.1), an estimation can already be proposed to calculate the effusive rate. A flow volume can be modelled as half the volume of an ellipsoid with the following equation:

$$V = \frac{\frac{4}{3}\pi l \frac{w}{2} h}{2}$$

where $V$ is the volume of the flow, and $l$, $w$, $h$, its total length, average width and thickness. Because the width and thickness can vary along the flow, their standard deviation can be calculated, giving lower and upper bounds for the total volume. To this error can be added the error on the vertical resolution of MOLA of ±3 on the thickness, in the case of Mars.
With AROMAS, a more accurate estimation of the volume and the overlapped area can be provided whereas, for instance, J. A. Richardson et al. (2017) used a range of potential lava flow thicknesses from 10 to 90 m. The inferred lava flow length path through the stratigraphy also bypasses the issue of non-visible lava flow extent and provides an estimation of the total length. However, computing the volume with the total length defined as the length between the distal part of flows to the potential source could yield unrealistically high values. Flows are wider and thicker further away from the vent. Therefore, extrapolating the average width and thickness to the proximal part would be incorrect. Assuming the bulk volume of the flow is located in its more distal part, where it is not topographically confined, the total length used below for effusive rate estimation is constrained to the uppermost part of the youngest flow.

#### Arsia Mons

At Arsia Mons, assuming that the comprehensive volume of flows erupted within the 300 to 50 Ma, the effusive rate can be estimated to range from 0.21 to 0.98 $km^3.Myr^{-1}$. For comparison, J. A. Richardson et al. (2017) found a maximum effusive rate of 1 to 8 $km^3.Myr^{-1}$ during 150 Ma. Coeval lava emplacement at the caldera and at the lava aprons increases the total effusive rate for the same period at Arsia Mons. As pointed out by J. A. Richardson et al. (2017), the minimum magma production rate to sustain a magma chamber at depth (L. Wilson et al., 2001b) is orders of magnitude higher than rates inferred from the effusive rate, using the intrusive-extrusive ratio from e.g. Greeley and Schneid (1991). This means that either the extrusive/intrusive ratio is not correct or the estimated volume of extruded basalt at the surface is too low. If intra-caldera and apron recent activity are coeval and share a common magma source at depth, computation of the effusive

rate for the last 300 Myrs at Arsia would require including all the volcanic flows around the shield. Similar lava flow sets to the one studied during this work likely exist around Arsia Mons, although they may be partially covered by glacial deposits to the west.

#### Lanzarote

The lava flows of La Corona were dated  26 ka and follow a previous volcanic episode at  91 ka (Coello et al., 1992). Effusive rates for that period were found to range from 0.013 to 0.028 $km^3.kyr^{-1}$ (Becerril et al., 2017). Using the AROMAS estimate for the total volume of La Corona lava flows over a 90 000 year period, the effusive rate ranges from 0.0057 to 0.023 $km^3.kyr^{-1}$. The AROMAS methodology therefore provides robust results. The northern Lanzarote volcanic episodes often included widespread pyroclast deposition (Tomasi et al., 2023) which are ignored by this method. Lava flows which are now underwater in response to the late Pleistocene sea level variations, as well as lava flows which propagated to the ocean through lava tubes also contributed to the total volume of erupted material but are missing from the estimation done here by AROMAS.

### 7.1.3 AROMAS stratigraphy and morphology

The AROMAS workflow allows to reconstruction of the stratigraphy and morphometric parameters of lava flows. In the two examples presented in this work, we saw that AROMAS successfully generates a stratigraphic map, but also gives morphometric values such as the total lengths of the flows. However, the current design of the workflow has some minor shortcomings which future work should focus on to remove them. In particular, the topological sorting function and the determination of the total length of the flows can be improved (see section 4.4.1). In addition, further improvements in future versions of AROMAS will strengthen the accuracy of the results.

#### Symbology

Currently, the symbology classification is ignored by the workflow, which means that an erosive contact is interpreted the same way as a lava flow scarp, for instance. While both contact lines correctly yield an emplacement higher in the stratigraphic column (i.e. younger), they correspond to vastly different types of lava margins. In the case of a flow bounded by channel levees, AROMAS would currently measure its width and fractal dimension. Here the width could be interesting to calculate the volume of the flow, but inferring rheological properties from such width measurement or the fractal dimension would be incorrect.

Apart from the contact type, their reliability should also be taken into account before computing the morphometric parameters. For instance, an uncertain or inferred contact would yield a different fractal dimension than a sharp one.

#### Fractal dimension

AROMAS replicates the method used by Bruno et al. (1992) to compute the fractal dimension of the lava flow margins and infer the flow type, which consists of a structured walk using different rod lengths. More recent work has demonstrated the importance of scale in the analysis of flow margin fractal dimension. Schaefer et al. (2021) showed that the bi-normal distribution between 'a'ā and pāhoehoe disappears at a larger scale (i.e. higher mean rod length) and transitional lava types such as rubbly and slabby flows can display varying fractal dimension values. In their studies, the authors used rod lengths varying between tens of metres to hundreds of metres. On Mars, given the image resolution and size of the lava flows, the rod length used in this work can be in the thousands of metres. How the fractal dimension patterns evolve for such rod lengths is not formally determined due to the absence of terrestrial measurements at this scale. Nevertheless, AROMAS could provide valuable insights into lava flow classification using the fractal dimension. The results presented here indicate an inverse correlation between thermal inertia diversity and fractal dimension. Future AROMAS versions based on new multiscale fractal dimension measurements at terrestrial lava flows shall yield a more comprehensive lava flow type characterisation from remote sensing. It would eventually make possible a reliable determination of lava flow viscosity from calculated fractal dimension.

#### Surface analysis from multispectral data

In complement to an improved fractal dimension retrieval, an automated analysis of the flow surface composition and texture using THEMIS or CaSSISspectral information could be added to AROMAS, following the work of Crown and Ramsey (2017). Such an endeavour would face the problem of dust cover in the area studied in this work but could be more readily applied to other places on Mars where the lava flow surface is better exposed, and even on Earth.

#### Combining relative and absolute chronology

To estimate the effusive rate at Arsia Mons, J. A. Richardson et al. (2017) combined the results from the relative stratigraphy and impact crater retention age. Using a Monte Carlo simulation, the authors simulated 10,000 sets of ages to fill the gaps in the stratigraphic tree where no absolute age could be derived (i.e. where the units are too small to retain enough impact crater). Using this approach could allow us to better estimate the effusive rate evolution for a given set of volcanic flows.

## 7.2 Conclusion

Reconstructing the chrono-stratigraphy of volcanic emplacement on Mars provides insights into understanding the internal dynamics of the planet. Knowing the effusive rate (i.e. the volume of erupted lava per unit of time) of an edifice can help constrain the models of magma production rate at depth. Current methods rely on the assumption of the volume of erupted material. The AROMAS workflow proposes an approach to, at the same time, reconstruct the stratigraphy of different lava flows and infer morphological proprieties. Combining these allows for a better estimation of the erupted volume. Using AROMAS on recent lava flows at Arsia Mons, a recent effusive activity from 390-270 to 40-80 Ma was studied. The results demonstrate AROMAS' capabilities to reconstruct the stratigraphy of volcanic episodes and derive a total volume of erupted material. In addition, the analysis of the fractal dimension of lava flow margins shows a promising perspective for lava flow type characterisation from the remote sensing perspective. The terrestrial example presented here also demonstrates the flexibility of AROMAS regardless of the planetary body. Its application could be extended to lava flows on Venus and Io, with the help of data collected by future missions like ESA EnVision and NASA Veritas to Venus or ESA JUICE to the Jovian system.

The second part of this work demonstrated the performances of the CaSSIS DTMs refined through photogrammetry. These data will complement the wealth of already existing datasets and could prove to be valuable for future work regarding aeolian bedforms or other smaller-scale geological features on Mars.

# Appendix A

# AROMAS main code

---

```
#--------------------------------------
#####Importing modules, packages and files
#--------------------------------------

#To manipulate shapefiles and geometry objects
import geopandas as gpd
import shapely
from shapely.ops import substring, polygonize, unary_union
from shapely.geometry import Polygon, Point, LineString, MultiLineString
import arcpy #From ArcGIS Pro. Future versions will not need it.
from shapely.strtree import STRtree


#Dealing with distances, azimuths and projections
from geopy.distance import distance as geopy_distance
from geopy.point import Point as GeopyPoint
from pyproj import CRS

#To interpolate the elevation from the geometry objects
import rasterio
from rasterio import features, windows
from skimage.measure import find_contours
from pyproj import Transformer

#Plot
import matplotlib.pyplot as plt
import matplotlib as mpl
import colorsys
from matplotlib_scalebar.scalebar import ScaleBar
from mpl_toolkits.axes_grid1.inset_locator import inset_axes
from adjustText import adjust_text
cm = 1/2.54 #For matplotlib fig size

#Misc
import math
```

```
import numpy as np
import customFuctions as cF

#Tree building
import networkx as nx

#The directory where the shapefiles are stored
workDir = r'your\path\to\work\dir'

#Import the geological contacts
path_to_contacts = r'\contacts.shp'

#Import the polygons (If created from ArcGIS)
path_to_poly = r'\units.shp'

#Import the DEM GeoTIFF
geotiff = r'your\path\to\DEM.tif'

#----------------------------------------------------------------------
### Here We prepare the shapefiles and import them into the script as
    GeoPandas Data Frame which contain the
### geometry and the attribute table of each shapefile.
### Preferably, feature vertices should be densified in order to "harmonize
    them" and make the routine runs smoother
#----------------------------------------------------------------------

#Allow overwrite
arcpy.env.overwriteOutput = True

#-#-#-#-#-#-#-#-#-#-#-#-#-#-#-
#Convert the polylines to polygons
arcpy.management.FeatureToPolygon(workDir+path_to_contacts,
    workDir+r'\autoGeneratedLavaFlows.shp')
path_to_poly = r'\autoGeneratedLavaFlows.shp'
#-#-#-#-#-#-#-#-#-#-#-#-#-#-#-

#Copy shapefiles before densifying
path_to_contacts_densified = r'\contacts_densified.shp'
path_to_poly_densified = r'\polygons_densified.shp'
arcpy.management.Copy(workDir+path_to_contacts,
    workDir+path_to_contacts_densified)
arcpy.management.Copy(workDir+path_to_poly, workDir+path_to_poly_densified)

# #Densify the shapefiles
arcpy.edit.Densify(workDir+path_to_contacts_densified, "DISTANCE", 50)
arcpy.edit.Densify(workDir+path_to_poly_densified, "DISTANCE", 50)

#Store to GeoDataFrame
```

```
geolContacts = gpd.read_file(workDir+path_to_contacts_densified)
geolContacts = geolContacts.explode(index_parts=False) #Make sure
    multi-part geometries are split into individual features
lavaFlows = gpd.read_file(workDir+path_to_poly_densified)

#Add a label to each lava flow
lavaFlows['label'] = ['lvf_'+str(index) for index in list(lavaFlows.index)]
lavaFlows['node'] = [str(index) for index in list(lavaFlows.index)]

#-------------------------------------------------------------------------
### Run the functions on the GeoDataFrames
#-------------------------------------------------------------------------

listAnalizedMargins = build_strati_dict(lavaFlows, geolContacts,
    percent=True)

#-------------------------------------------------------------------------
### Now that the list of margins and their relationships is built, we can
    clean the list and create a dictionnary
#-------------------------------------------------------------------------

#The empty dictionnary
stratiRelations = {}

#Iterate each entry in the list corresponding to the margins of a lava flow
for node, lvf in enumerate(listAnalizedMargins):

    listParents =[] #This will contain the list of neighbouring nodes and
        the relationships
    listNeighbours = [] #A seperate list to avoid double entries of
        neighbours and check
    listRelations =[]

    for i, margin in enumerate(lvf.geometry):
        if lvf['neighbours'].iloc[i] not in listNeighbours: #Check for
            double entries
            listNeighbours.append(lvf['neighbours'].iloc[i])
            listRelations.append(lvf['relation'].iloc[i])

    for j, neighbour in enumerate(listNeighbours):
        listParents.append((str(listNeighbours[j]), listRelations[j]))

    stratiRelations[str(node)] = listParents #Store in the dictionnary

#-------------------------------------------------
### Read the dictionnary and create a directed graph
# -------------------------------------------------
```

```
# Create a directed graph
G = nx.DiGraph()

# Iterate through the relationships and add them to the graph
for node, edges in stratiRelations.items():
    for edge in edges:
        # Reverse the direction of the edge
        if edge[1] == 'above':
            G.add_edge(edge[0], node, relationship=edge[1])
        elif edge[1] == 'below':
            G.add_edge(node, edge[0], relationship=edge[1])

#-------------------------------------------------------
### Check that the diGraph is acyclic
#-------------------------------------------------------
if not nx.is_directed_acyclic_graph(G):
    cycles = nx.find_cycle(G)
    raise Exception("The diGraph contains cycles around the following
        nodes:"+str(cycles)+"\n Run the 'fix' routine and/or edit
        shapefiles")
else:
    #Save the dictionnary
    np.save('relationsDict_fullwithmargins.npy', stratiRelations)

#-------------------------------------------------------------
### The following routine aims to reconstruct the stratigrapy from the
    dictionnary
#-------------------------------------------------------------

#Keep the count of layers
layerCount = 0

#topological_generations stratifies a DAG into generations.
#More info on:
    https://networkx.org/documentation/stable/reference/algorithms/
generated/networkx.algorithms.dag.topological_generations.html
for layer, nodes in enumerate(nx.topological_generations(G)):
    layerCount +=1
    for node in nodes:
         G.nodes[node]["layer"] = layer #Add the layer number to the diGraph
             dictionnary

#Setting the colour map
colormap = get_colors_from_colormap('Spectral', layerCount) #Creates a
    custom colormap

pos={} #The pos dictionnary is read later to plot the diGraph
colorDict = {} #Color dictionnary to plot with the correct colour
```

```
for layer, nodes in enumerate(nx.topological_generations(G)):
    nbNodes = len(nodes)
    coorY = -float(layer) #The height level on the figure
    if nbNodes == 1:
        coorX = layerCount/2 #Centered
        for n, node in enumerate(nodes):
            pos[node] = [coorX, coorY]
            colorDict[node]=[colormap[layer], layer, node]
    else:
        #Create the range of X coord based on the number of items
        coorX = pick_symmetric_numbers(0, layerCount, nbNodes)
        for n, node in enumerate(nodes):
            pos[node] = [coorX[n], coorY]
            colorDict[node]=[colormap[layer], layer, node]

#Create the colour range for the plot based on the dictionnary
colorList=[]
toDF = [] #To merge with the lavaFlow GDf and plot
for node in G:
    colorList.append(tuple(colorDict[node][0]))
    toDF.append([colorDict[node][1], colorDict[node][2]])

#joining the strati data with the lavaflows geometries
stratiInfo = pd.DataFrame(data=toDF, columns=['layer', 'nodeNumber'])
stratiInfo['label']=['lvf_'+str(index) for index in
    list(stratiInfo['nodeNumber'])]
lavaFlows = lavaFlows.merge(stratiInfo, on='label')


#-------------------------------------------------------------
### This code aims to merge margins and prepare the computation of the
    fractal coefficient
#-------------------------------------------------------------

#-----------------------------------------------------------
### First we merge the "good" continuous margins together
#-----------------------------------------------------------
mergedLines = []
for lvf in listAnalizedMargins:

    # First we store them in individual list
    listMargins = []
    for i in range(len(lvf.geometry)):

        #The "below" are the overlapping margins. Free margins are inclded
            here also.
```

```
        if lvf['relation'].iloc[i] == 'below' or lvf['relation'].iloc[i] ==
            None :
            listMargins.append(lvf.geometry.iloc[i])

    # Merge the continguous lines
    mergedLines.append(shapely.ops.linemerge(listMargins))

#-----------------------------------------------------------
### Now that the lines were merged, that have to be sorted between either
    Mutli and single LineStrings
#-----------------------------------------------------------
marginsForFract = []
for item in mergedLines:

    #Lines were merged into one or only one line was there
    if item.geom_type == 'LineString':
        marginsForFract.append([item])

    #Non-contiguous lines formed MultiLineStrings
    elif item.geom_type == 'MultiLineString':
        multiMargins = []
        for part in item.geoms: #Explode the MultiLineStrings
            multiMargins.append(part)
        marginsForFract.append(multiMargins)
    else:
        #Any other form of geometry, ignore them
        marginsForFract.append(None)

# Add the merged margins into the GeoDataFrame
lavaFlows['marginsForFract'] = marginsForFract

#-----------------------------------------------------------
### Run the fractal dimension function and store it in the GeoDataFrame
#-----------------------------------------------------------
fractDim_list, corrCoef_list =
    fractalDimensionForLavaFlows(lavaFlows['marginsForFract'])
lavaFlows['fractDim'] = fractDim_list
lavaFlows['corrCoef'] = corrCoef_list

#-----------------------------------------------------------------
### Lava flow length
#-----------------------------------------------------------------



#-----------------------------------------------------------------
### Find all the leave and source nodes
#-----------------------------------------------------------------
leaf_nodes = find_leaf_nodes(G)
```

```
source_nodes = []
for node in leaf_nodes:
    source_nodes.append(findPathToTop(node, G))

#-----------------------------------------------------------------
### Check that all the nodes are covered
#-----------------------------------------------------------------

checkList = []
#iterate that list
for leafNode in leaf_nodes:

    #Choose the source node
    sourceNode = source_nodes[leaf_nodes.index(leafNode)]

    #Calculate the path
    path = nx.shortest_path(G, source=sourceNode, target=leafNode,
        weight=None, method='dijkstra')
    path.reverse()

    #First we iterate the nodes in the path to generate the lengths
    for node in path:
        if node not in checkList:
            checkList.append(node)

#Now compare the checklist with the list of nodes and add the missing nodes
for node in G.nodes:
    if node not in checkList:
        source_nodes.append(findPathToTop(node, G))
        leaf_nodes.append(node)

#-----------------------------------------------------------------
### Go through every node and calculate their apparent and inferred length,
    and their width.
#-----------------------------------------------------------------

# Geographic long/lat coordinate system
mars2000IAU = 'GEOGCS["Mars 2000", DATUM["D_Mars_2000",
    SPHEROID["Mars_2000_IAU_IAG",3396190.0,169.89444722361179]],
    PRIMEM["Greenwich",0], UNIT["Decimal_Degree",0.0174532925199433]]'

#Convert X/Y to Lat/Lon
lavaFlows_geo = lavaFlows.to_crs(mars2000IAU)

import warnings

#A functions returns a warning for calling centroid on geographic coords
with warnings.catch_warnings(record=True):
```

```
layer=layerCount
alreadyDone_app= []
alreadyDone_inf = []
lengthLines = []

#Store in dictio
apparentLength_geoms = []
inferredLenght_geoms = []
pathLength_geoms = []

#parameters for length calc
distPoints = 0.01

#Open the DTM
raster = rasterio.open(geotiff)

#Now iterate that list
for leafNode in leaf_nodes:

    #Choose the source node
    sourceNode = source_nodes[leaf_nodes.index(leafNode)]

    #Calculate the path
    path = nx.shortest_path(G, source=sourceNode, target=leafNode,
        weight=None, method='dijkstra')
    path.reverse()


    pathLen_list =[]

    #First we iterate the nodes in the path to generate the lengths
    for node in path:

        startPoint = None
        endPoint = None
        pathEndPoint = None

        #Select the lava
        currentLava = lavaFlows.loc[lavaFlows['label']=='lvf_'+node]

        #Select the vertices
        verticesCoords =
            currentLava.reset_index().geometry[0].exterior.coords
        vertices = [Point(coord) for coord in verticesCoords]

        #Get the height and store do GDF
        verticesGDF = get_vertices_height(vertices, raster)
```

```
#Endpoint (i.e. the lowest point of the lava flow ~ the tip)
endPoint =
    verticesGDF.loc[verticesGDF['height'].idxmin()].geometry

#Check whether or not the node is a top parent node
if path.index(node) == len(path) -1: #TOP NODE

    #Source point is the highest point
    startPoint =
        verticesGDF.loc[verticesGDF['height'].idxmax()].geometry

    #Get the index of the node below
    childIndex = path.index(node)-1
    pathEndPoint = getContactPoint(currentLava, lavaFlows, path,
        childIndex, raster)
    pathLen, drop = calculateLavaLength(pathEndPoint, startPoint,
        currentLava, nbiter = 1, distPoints=distPoints)
    pathLen_list.append(pathLen)

elif path.index(node) == 0: #BOTTOM NODE
    #Get the index of the node above
    parentIndex = path.index(node)+1
    startPoint = getContactPoint(currentLava, lavaFlows, path,
        parentIndex, raster)
    pathLen_list.append(None)

else: #INTERMEDIATE NODE
    ###The low point can be the contact with child node
    #Get the index of the node above
    parentIndex = path.index(node)+1
    startPoint = getContactPoint(currentLava, lavaFlows, path,
        parentIndex, raster)

    #Get the index of the node below
    childIndex = path.index(node)-1
    pathEndPoint = getContactPoint(currentLava, lavaFlows, path,
        childIndex, raster)
    pathLen, drop = calculateLavaLength(pathEndPoint, startPoint,
        currentLava, nbiter = 1, distPoints=distPoints)
    pathLen_list.append(pathLen)

#Calculate the apparent length
if node not in alreadyDone_app:
    apparentLength, width_geoms = calculateLavaLength(endPoint,
        startPoint, currentLava, nbiter = 2,
        distPoints=distPoints)
```

```
            gpdAppLength = gpd.GeoDataFrame(geometry=[apparentLength],
                crs = mars2000IAU)
            mask = lavaFlows['label'] == 'lvf_'+node
            #print(len(width_geoms))
            #print('lvf '+str(node)+' => '+str(len(width_geoms)))
            lavaFlows_geo.loc[mask, 'appLength_geom'] = apparentLength
            lavaFlows_geo.loc[mask, 'appLength'] =
                gpdAppLength.to_crs(lavaFlows.crs).geometry[0].length
                #Convert to map coordinate
            toMultiString =
                width_geoms.to_crs(lavaFlows.crs).geometry.to_list()
            lavaFlows_geo.loc[mask, 'width_geoms'] =
                MultiLineString(toMultiString)
            #lavaFlows_geo.loc[mask, 'width'] =
                width_geoms.to_crs(lavaFlows.crs).geometry.length.mean()
            #Add to done list
            alreadyDone_app.append(node)

    #Now we will put the data alltogether and calculate the infered
        length
    for node in path:
        inferredLength_list = []
        if node not in alreadyDone_inf:

            #Check if not the top:
            if path.index(node) != len(path) -1:

                #Now iterate combine the path nodes together
                for i in range(path.index(node)+1, len(path)):
                    inferredLength_list.append(pathLen_list[i])

                #merge the path lines together
                if len(inferredLength_list) > 1:
                    multi_line = MultiLineString(inferredLength_list)
                    merged_line = shapely.ops.linemerge(multi_line)
                else:
                    merged_line = inferredLength_list[0]

                #Add to the gdf
                mask = lavaFlows['label'] == 'lvf_'+node
                lavaFlows_geo.loc[mask, 'inferredLength_geom'] =
                    merged_line
                inferredLenght_geoms.append(merged_line)

                #Store to GPD and convert to projected to measure the
                    length
```

```
                    gpdInferredLength =
                        gpd.GeoDataFrame(geometry=[merged_line], crs =
                        mars2000IAU).to_crs(lavaFlows.crs)


                    #Calculate the total length
                    lavaFlows_geo.loc[mask, 'totalLength'] =
                        gpdInferredLength.geometry[0].length +
                        lavaFlows_geo.loc[mask, 'appLength']

                else:
                    mask = lavaFlows['label'] == 'lvf_'+node
                    lavaFlows_geo.loc[mask, 'totalLength'] =
                        lavaFlows_geo.loc[mask, 'appLength'] #Only the
                        apparent length if it's a top layer
                    inferredLenght_geoms.append(None)

                alreadyDone_inf.append(node)

                print('Computing lava flow length: ' +
                    str(round(len(alreadyDone_inf)/len(lavaFlows)*100,2))+'%',
                        end="\r")

#-----------------------------------------------------------------
#Lava flow width
#-----------------------------------------------------------------

goodWidth_list = []
avgWidth = []
for i in lavaFlows_geo.index:
    lvf = lavaFlows_geo.iloc[i]
    goodWidth_geom = []
    goodWidth = []
    if lvf['marginsForFract']:
        #Get width lines and iterate them
        for widthLine in lvf['width_geoms'].geoms:
            goodStart= False
            goodEnd = False
            for margin in lvf['marginsForFract']:
                #Check if the ends are bound by good margins
                if Point(widthLine.coords[0]).within(margin.buffer(10)):
                    goodStart = True
                if Point(widthLine.coords[-1]).within(margin.buffer(10)):
                    goodEnd =True
            if goodStart and goodEnd:
                #Keep the width
                goodWidth_geom.append(widthLine)
                goodWidth.append(widthLine.length)
```

```
        if goodWidth:
            avgWidth.append(sum(goodWidth)/len(goodWidth))
        else:
            avgWidth.append(None)
    else:
        avgWidth.append(None)

    goodWidth_list.append(goodWidth_geom)

lavaFlows_geo['goodWidth'] = goodWidth_list
lavaFlows_geo['avgWidth'] = avgWidth

#-----------------------------------------------------------------
### Lava flow thickness
#-----------------------------------------------------------------

#import MOLA
path_to_mola = r'\MolaShots.shp'

#import and project the mola shots
molaShots = gpd.read_file(workDir+path_to_mola) #ESRI shqpefile created
    from PDS ODE MOLA QUery in Long/Lat
molaShots_proj = molaShots.to_crs(lavaFlows.crs)

fullList = []
for i in lavaFlows.index:
    lvf = lavaFlows.iloc[i]
    listForFlow =[]
    if lvf['marginsForFract']:
        for margin in lvf['marginsForFract']:
            listForMargin = []
            groupedPoints = prepareMolaData(margin, molaShots_proj)
            for n, group in enumerate(groupedPoints):

                #Select the associated points
                currentOrbitPoints = groupedPoints[n]

                if len(currentOrbitPoints) > 3: #Min 3 points

                    #Get the lowest point
                    minPoint = currentOrbitPoints['TOPOGRAPHY'].min()

                    #Calculate the elevation difference
                    currentOrbitPoints['THICKNESS'] = abs(minPoint -
                        currentOrbitPoints['TOPOGRAPHY'])

                    #List for current margin
```

```
                listForMargin.append(currentOrbitPoints)
            else:
                listForMargin.append(None)
        #print(listForMargin)
        listForFlow.append(listForMargin)
    else:
        listForFlow.append(None)

    fullList.append(listForFlow)

avgThick = []
for lava in fullList:
    thick=[]
    for margin in lava:
        if margin is not None:
            for orbit in margin:
                if orbit is not None:
                    thick.append(orbit['THICKNESS'].max())
    if thick:
        avgThick.append(sum(thick)/len(thick))
    else:
        avgThick.append(None)

lavaFlows_geo['avgThick'] = avgThick

#-----------------------------------------------------------------
### Plotting the statistics
#-----------------------------------------------------------------
fig , axs = plt.subplots(nrows = 3, ncols=2, figsize = (18*cm, 26*cm))

counts = axs[0,0].hist((lavaFlows_geo['avgWidth']), bins=12)
median = lavaFlows_geo['avgWidth'].median()
mean = lavaFlows_geo['avgWidth'].mean()
std = lavaFlows_geo['avgWidth'].std()

axs[0,0].vlines(x = mean, ymin=0, ymax = max(counts[0])+1, color='red')
axs[0,0].vlines(x = mean-std, ymin=0, ymax = max(counts[0])+1, color='k',
    ls='-.')
axs[0,0].vlines(x = mean+std, ymin=0, ymax = max(counts[0])+1, color='k',
    ls='-.')

axs[0,0].fill_betweenx([0,max(counts[0])+1], [mean-std], [mean+std], color
    = 'lightgray')
axs[0,0].set_ylim(0, max(counts[0])+1 )
axs[0,0].hist(lavaFlows_geo['avgWidth'], bins = 12, linewidth = 0.5,
    edgecolor = 'black', color = 'orange')
axs[0,0].set_xlabel('Lava flow width (m)')
axs[0,0].set_ylabel('Counts')
```

```
axs[0,1].plot(lavaFlows_geo['avgWidth'], lavaFlows_geo['avgThick'],
    marker='+', ls = ' ', color = 'red' )
axs[0,1].set_xlabel('Average width (m)')
axs[0,1].set_ylabel('Average thickness (m)')


counts = axs[1,0].hist((lavaFlows_geo['avgThick']), bins=12)
median = lavaFlows_geo['avgThick'].median()
mean = lavaFlows_geo['avgThick'].mean()
std = lavaFlows_geo['avgThick'].std()

axs[1,0].vlines(x = mean, ymin=0, ymax = max(counts[0])+1, color='red')
axs[1,0].vlines(x = mean-std, ymin=0, ymax = max(counts[0])+1, color='k',
    ls='-.')
axs[1,0].vlines(x = mean+std, ymin=0, ymax = max(counts[0])+1, color='k',
    ls='-.')

axs[1,0].fill_betweenx([0,max(counts[0])+1], [mean-std], [mean+std], color
    = 'lightgray')
axs[1,0].set_ylim(0, max(counts[0])+1 )
axs[1,0].hist(lavaFlows_geo['avgThick'], bins = 12, linewidth = 0.5,
    edgecolor = 'black', color = 'royalblue')
axs[1,0].set_xlabel('Lava flow thickness (m)')
axs[1,0].set_ylabel('Counts')


axs[1,1].plot(lavaFlows_geo['avgThick'], lavaFlows_geo['fractDim'],
    marker='+', ls = ' ', color = 'royalblue' )
axs[1,1].set_xlabel('Average thickness (m)')
axs[1,1].set_ylabel('Fractal dimension')


counts = axs[2,0].hist((lavaFlows_geo['fractDim']), bins=20, range=(1.0,
    2.0))
median = lavaFlows_geo['fractDim'].median()
mean = lavaFlows_geo['fractDim'].mean()
std = lavaFlows_geo['fractDim'].std()

axs[2,0].vlines(x = mean, ymin=0, ymax = max(counts[0])+1, color='red')
axs[2,0].vlines(x = mean-std, ymin=0, ymax = max(counts[0])+1, color='k',
    ls='-.')
axs[2,0].vlines(x = mean+std, ymin=0, ymax = max(counts[0])+1, color='k',
    ls='-.')

axs[2,0].fill_betweenx([0,max(counts[0])+1], [mean-std], [mean+std], color
    = 'lightgray')
```

```
axs[2,0].set_ylim(0, max(counts[0])+1 )
axs[2,0].hist(lavaFlows_geo['fractDim'], bins = 20, linewidth = 0.5,
    edgecolor = 'black', color = 'teal', range=(1.0, 2.0))
axs[2,0].set_xlabel('Fractal dimension')
axs[2,0].set_ylabel('Counts')


axs[2,1].plot(lavaFlows_geo['avgWidth'], lavaFlows_geo['fractDim'],
    marker='+', ls = ' ', color = 'teal' )
axs[2,1].set_xlabel('Fractal dimension')
axs[2,1].set_ylabel('Average width (m)')

fig.tight_layout()


#---------------------------------------------------------------------
### Create Topographic contours for the map
#---------------------------------------------------------------------

#Get the extent for the map
minx, miny, maxx, maxy = lavaFlows_geo.geometry.total_bounds
geographic_extent = [round(minx,1), round(miny,1), round(maxx,1),
    round(maxy,1)]

# Open the raster file
src = rasterio.open(geotiff)

# Get the CRS of the raster
raster_crs = src.crs

# Create a Transformer object for transforming coordinates.
transformer = Transformer.from_crs(mars2000IAU, raster_crs, always_xy=True)

# Transform geographic coordinates to the raster's CRS
minx_proj, miny_proj = transformer.transform(geographic_extent[0],
    geographic_extent[1])
maxx_proj, maxy_proj = transformer.transform(geographic_extent[2],
    geographic_extent[3])

# Transform projected coordinates to pixel coordinates
bottom, left = src.index(minx_proj, miny_proj)
top, right = src.index(maxx_proj, maxy_proj)

# Define the window to read based on the pixel coordinates
window = windows.Window.from_slices((top, bottom), (left, right))

# Read the window into an array
array = src.read(1, window=window)
```

```
# Store raster metadata (adjust transform to match window)
transform = src.window_transform(window)
crs = src.crs

#Create XYZ mesh arrays and flip vertically the raster to match the shape
    of the mesh
x = np.linspace(geographic_extent[0], geographic_extent[2], array.shape[1])
y = np.linspace(geographic_extent[1], geographic_extent[3], array.shape[0])
X, Y = np.meshgrid(x, y)
Z = np.flipud(array)

#-----------------------------------------------------------------------
### Plot the map and the tree
#-----------------------------------------------------------------------

#remove the last row (background unit)
# lavaFlows_geo.drop(lavaFlows_geo.tail(1).index,inplace=True)

# set up the Axes objects
fig, ax = plt.subplots(figsize=(18*cm, 18*cm))

#Set the figure
ax.set_xlim([round(minx,1), round(maxx,1)])
ax.set_ylim([round(miny,1), round(maxy,1)])
ax.set_xlabel('Longitude (East)', fontsize = 10)
ax.set_ylabel('Latitude (North)', fontsize = 10)
#ax.set_title("Test sample", fontsize = 11)

#Create a inset axes for the color bar inside the figure
cbaxes = inset_axes(ax, width="30%", height="3%", loc=3, borderpad=1.5)
cbaxes.set_title('Stratigraphic level', fontsize = 8)

#Add a North arrow
x, y, arrow_length = 0.95, 0.95, 0.1
ax.annotate('N', xy=(x, y), xytext=(x, y-arrow_length),
            arrowprops=dict(facecolor='black', width=5, headwidth=15),
            ha='center', va='center', fontsize=14,
            xycoords=ax.transAxes)


#Create a new column to have the high values representing high
    stratigraphical level
lavaFlows_geo['reverseLayer'] = [lavaFlows_geo['layer_x'].max() - lvf for
    lvf in lavaFlows_geo['layer_x']]

#Plot the polygons and the contours
```

```
lavaFlows_geo.plot(ax=ax, cmap=mpl.colormaps['Spectral_r'], #Reverse the
    colorbar
                column='reverseLayer',
                edgecolor="black",
                linewidth = 0.5,
                zorder = 1,
                legend = True,
                legend_kwds={"cax": cbaxes, "orientation": 'horizontal'}
                    #Insert the colorbar in the inset axes
                 )
CS = ax.contour(X, Y, Z, 2, colors='black', linewidths = 0.5)
ax.clabel(CS, inline=1, fontsize=8) #Add labels to the contour lines
CSmin = ax.contour(X, Y, Z, 4, colors='grey', linewidths = 0.5,
    linestyles='dashed') #Add minor contours dashed

#Tweak the the colorbar legend
cbaxes.set_xticks([0, 10], ['Old', 'Young'], fontsize=8)
cbaxes.set_yticks([])

#Add a grid to the map
ax.grid(visible = True, zorder = 3, linewidth=0.25, linestyle='-.')

#Add labels to the polygons
texts = []
bbox = dict(boxstyle="round", fc="0.8")
for idx, row in lavaFlows_geo.iterrows():
    texts.append(ax.annotate(text=row['node'], bbox=bbox,
        xy=(row.geometry.centroid.x, row.geometry.centroid.y), ha='center',
        va='center', fontsize=7))

# # Use adjust_text to resolve overlapping labels
adjust_text(texts, ax=ax, force_points=0.3, force_text=0.8,
    expand_points=(1,1), expand_text=(1,1))
fig.savefig(r"C:\Users\tesso\OneDrive\Documents\Work\PhD - Manuscript
    Thesis\latex\Figures\chapterAROMAS\geologicalMap_sample.pdf")
# fig.tight_layout()
# fig.savefig("lavaFlow_map.png")

#---------------------------------------------------------------------
#### Plot the tree
#---------------------------------------------------------------------
fig, ax = plt.subplots(figsize=(15*cm, 15*cm))

#Create the digraph
nx.draw_networkx_nodes(G, edgecolors = colorList, node_color = 'lightgrey',
    linewidths=3, pos=pos, ax=ax)
nx.draw_networkx_edges(G, width=0.25, pos=pos, ax=ax)
nx.draw_networkx_labels(G, font_size = 10, pos=pos, ax=ax)
```

```
ax.set_title("Stratigraphical Relationships of units", fontsize=11)
#fig.tight_layout()
fig.savefig(r"C:\Users\tesso\OneDrive\Documents\Work\PhD - Manuscript
    Thesis\latex\Figures\chapterAROMAS\stratiTree.pdf")

#---------------------------------------------------------------------
### Plot the margin map
#---------------------------------------------------------------------

# set up the Axes objects
fig, ax = plt.subplots(nrows=1, figsize=(18*cm, 18*cm))

#Set the figure
ax.set_xlim([round(minx,1), round(maxx,1)])
ax.set_ylim([round(miny,1), round(maxy,1)])
ax.set_xlabel('Longitude (East)')
ax.set_ylabel('Latitude (North)')
#ax.set_title("AROMAS Lava Flows test sample")

#Add a North arrow
ax.annotate('N', xy=(x, y), xytext=(x, y-arrow_length),
           arrowprops=dict(facecolor='black', width=5, headwidth=15),
           ha='center', va='center', fontsize=18,
           xycoords=ax.transAxes)

#Plot the polygons and the contours
lavaFlows_geo.plot(ax=ax, cmap=mpl.colormaps['viridis'], #Reverse the
    colorbar
                column='fractDim',
                edgecolor="black",
                linewidth = 0.5,
                zorder = 1,
                legend = True,
                scheme="quantiles",
                legend_kwds={"title": "Fractal Dimension", "loc": 'lower
                    left'},
                missing_kwds={
                    "color": "lightgrey",
                    "edgecolor": "red",
                    "hatch": "///",
                    "label": "Missing values",
                },
               )
CS = ax.contour(X, Y, Z, 2, colors='black', linewidths = 0.5)
ax.clabel(CS, inline=1, fontsize=8) #Add labels to the contour lines
CSmin = ax.contour(X, Y, Z, 4, colors='grey', linewidths = 0.5,
    linestyles='dashed') #Add minor contours dashed
```

```
#Add a grid to the map
ax.grid(visible = True, zorder = 3, linewidth=0.25, linestyle='-.')

#Add labels to the polygons
texts = []
bbox = dict(boxstyle="round", fc="0.8")
for idx, row in lavaFlows_geo.iterrows():
    texts.append(ax.annotate(text=row['node'], bbox=bbox,
        xy=(row.geometry.representative_point().x,
        row.geometry.representative_point().y), ha='center', va='center',
        fontsize=7))

# # Use adjust_text to resolve overlapping labels
adjust_text(texts, ax=ax, force_points=0.3, force_text=0.8,
    expand_points=(1,1), expand_text=(1,1))




#------------------------------------------------------------------------
### Plot the thickness map
#------------------------------------------------------------------------

# set up the Axes objects
fig, ax = plt.subplots(nrows=1, figsize=(18*cm, 18*cm))

#Set the figure
ax.set_xlim([round(minx,1), round(maxx,1)])
ax.set_ylim([round(miny,1), round(maxy,1)])
ax.set_xlabel('Longitude (East)')
ax.set_ylabel('Latitude (North)')
#ax.set_title("AROMAS Lava Flows test sample")

#Add a North arrow
ax.annotate('N', xy=(x, y), xytext=(x, y-arrow_length),
           arrowprops=dict(facecolor='black', width=5, headwidth=15),
           ha='center', va='center', fontsize=18,
           xycoords=ax.transAxes)

#Plot the polygons and the contours
lavaFlows_geo.plot(ax=ax, cmap=mpl.colormaps['viridis'], #Reverse the
    colorbar
                column='avgThick',
                edgecolor="black",
                linewidth = 0.5,
                zorder = 1,
                legend = True,
                scheme="quantiles",
```

```
                    legend_kwds={"title": "Average thickness", "loc": 'lower
                        left'},
                    missing_kwds={
                        "color": "lightgrey",
                        "edgecolor": "red",
                        "hatch": "///",
                        "label": "Missing values",
                    },
                    )
CS = ax.contour(X, Y, Z, 2, colors='black', linewidths = 0.5)
ax.clabel(CS, inline=1, fontsize=8) #Add labels to the contour lines
CSmin = ax.contour(X, Y, Z, 4, colors='grey', linewidths = 0.5,
    linestyles='dashed') #Add minor contours dashed

#Add a grid to the map
ax.grid(visible = True, zorder = 3, linewidth=0.25, linestyle='-.')

#Add labels to the polygons
texts = []
bbox = dict(boxstyle="round", fc="0.8")
for idx, row in lavaFlows_geo.iterrows():
    texts.append(ax.annotate(text=row['node'], bbox=bbox,
        xy=(row.geometry.representative_point().x,
        row.geometry.representative_point().y), ha='center', va='center',
        fontsize=7))

# # Use adjust_text to resolve overlapping labels
adjust_text(texts, ax=ax, force_points=0.3, force_text=0.8,
    expand_points=(1,1), expand_text=(1,1))
```

# Appendix B

# AROMAS Stratigraphy

---

```
def point_at_90_degrees(pt1, pt2):
    """
    Function to calculate the position of a point located at 90 degrees
    with respect to a vector formed by two points

    :param pt1, pt2: points in long, lat coordinates
    """
    # Calculate the midpoint of the vector
    mx = (pt1[0] + pt2[0]) / 2
    my = (pt1[1] + pt2[1]) / 2

    # Calculate the vector components
    dx = pt2[0] - pt1[0]
    dy = pt2[1] - pt1[1]

    # Calculate the length of the vector
    length = math.sqrt(dx**2 + dy**2)

    # Calculate the unit vector components
    ux = dx / length
    uy = dy / length

    # Calculate the components of the vector rotated 90 degrees clockwise
    vx = -uy
    vy = ux

    # Calculate the coordinates of the point located at 90 degrees
    x = mx + length/2 * vx
    y = my + length/2 * vy

    return Point(x, y)

def infer_stratigraphy(lvf, contact, geolContacts, geolContacts_tree):
    """
```

```
    Function that check the overlapping relationship of a unit with its
        neighbour at a specific contact.

    Parameters:
    - lvf, contact: Shapely Polygon and LineString.
    - geolContacts: GeoDataFrame containing all the contacts
    - geolContacts_tree: STRtree of all the contacts
    """

    # A minium of 50 m is chosen
    if contact.length > 50:

        #Select the contacts from the global list that matches the current
            margin
        contacts = geolContacts_tree.query(contact.buffer(1.0),
            predicate='intersects')

        #Initiate in case several contacts are matching, select the longest
        maxLength = 0
        storeContact = None

        #Iterate the potential several contacts that are matching and select
            the matching vertices
        for contact_idx in contacts:
            contact_geom = geolContacts.iloc[contact_idx].geometry
            tempList = [Point(vertex) for vertex in contact_geom.coords if
                contact.intersects(Point(vertex).buffer(1.0))]

            #At least 3 points
            if len(tempList) > 2:
                #Create a LineString from the select vertices
                line_tempList = LineString(tempList)

                #Measure its length to compare to the current maximum
                line_length = line_tempList.length

                if line_length > maxLength:
                    contactType = geolContacts['type'].iloc[contact_idx]
                    maxLength = line_length
                    storeContact = line_tempList
                    storeIdx = contact_idx

        if storeContact:

            #Find the middle vertex
            nbVertices = len(storeContact.coords)
            midIndex = int(nbVertices/2)
```

```
            #Select the middle vertex and the previous point
            pt1 = storeContact.coords[midIndex-1]
            pt2 = storeContact.coords[midIndex]

            #Create a point at 90 degrees, right hand side
            pt90 = point_at_90_degrees(pt1, pt2)

            #Check the location of the created point and infer stratigraphy
            if lvf.contains(pt90):
                return "above"
            else:
                return "below"

def build_margins(lavaFlow, lavaFlows, listNeighbours, geolContacts,
    geolContacts_tree):
    """
    Function that iterates the margins of a unit, infer stratigraphy, list
        and store them.

    Parameters:
    - lavaFlow: Shapely Polygon with the current lava flow
    - lavaFlows, geolContacts: GeoDataFrames containing the lava flows in
    Shapely Polygons and the contacts Shapely LineStrings.
    - ListNeigbours: list of neighbouring units
    - geolContacts_tree: STRtree of all the contacts
    """

    #Pick a random neighbour to start the iteration (here the first in the
        list)
    touchedNeighbour = listNeighbours[0]
    currentNeighbour = lavaFlows.iloc[touchedNeighbour].geometry

    listVertices = [] #List that contain the vertices for the first margin
    listMargins = [] #List that will contain all the margins as LineStrings
    listRelations = [] #List that will contain the strati relationships
    listNodes=[] #List that will contain the node numbers of the
        neighbouring unit for each margin
    #listContactTypes = [] #List that will contain the contact type (sure,
        inferred, etc.)

    #Iterate the vertices
    for i, vertex in enumerate(lavaFlow.exterior.coords):

        #If the neighbour is changing => new margin
        if not Point(vertex).intersects(currentNeighbour.buffer(1)): #Add a
            1 meter buffer to avoid mismatch

            #Add the last vertex
```

```
            listVertices.append(vertex)

            #Create a new margin and store it
            if len(listVertices)>2:
                margin = LineString(listVertices)

                #Infer the stratigraphical relationship at this margin
                #relation, contactType = infer_stratigraphy(lavaFlow, margin,
                    geolContacts, geolContacts_tree)
                relation = infer_stratigraphy(lavaFlow, margin, geolContacts,
                    geolContacts_tree)

                #These three lists should have the same length at the end and
                    will be used to create a GDF
                listNodes.append(touchedNeighbour) #The neighbour's node
                    number
                listRelations.append(relation) #Above or Below
                listMargins.append(margin) #The margin geometry itself
                #listContactTypes.append(contactType)

            #Reset the list for the next margin and add the new first point
            listVertices = []
            listVertices.append(vertex)

            #Identify the new neighbour node number from the neighbour's list
            for neighbour in listNeighbours:
                neighGeom = lavaFlows.iloc[neighbour].geometry.buffer(1)
                if Point(vertex).intersects(neighGeom):
                    touchedNeighbour = neighbour #Node number
                    currentNeighbour =
                        lavaFlows.iloc[touchedNeighbour].geometry #Neighbour's
                        geometry

        else:
            #Continue on the same margin and add the vertex
            listVertices.append(vertex)

    #Finish and create the last margin
    if len(listVertices)>1:
        margin = LineString(listVertices)
        relation = infer_stratigraphy(lavaFlow, margin, geolContacts,
            geolContacts_tree)
        listNodes.append(touchedNeighbour)
        listRelations.append(relation)
        listMargins.append(margin)
        #listContactTypes.append(contactType)

    #Store the data into a GeoDataFrame
```

```
    rawStorage = gpd.GeoDataFrame(geometry = listMargins, crs=lavaFlows.crs)
    rawStorage['neighbours'] = listNodes
    rawStorage['relation'] = listRelations
    #rawStorage['contactType'] = listContactTypes

    return rawStorage

### This function consists in, from the list of polygons and the list of
    contacts, create a dictionary containing
### information about the stratigraphical relationship of each unit with
    its neightbours.
### WARNING This is a time consuming step

def build_strati_dict(lavaFlows, geolContacts, percent=True):
    """
    Main function.

    Parameters:
    - lavaFlows, geolContacts: GeoDataFrames containing the lava flows in
    Shapely Polygons and the contacts Shapely LineStrings.
    - percent (Boolean): Display the percentage of completion
    """

    # Create an R-tree index for lavaFlows
    lavaFlows_tree = STRtree(lavaFlows.geometry)

    # Create an R-tree index for geolContacts
    geolContacts_tree = STRtree(geolContacts.geometry)

    listAnalizedMargins = []

    #Iterate each lava flow geometry
    for i, lvf in enumerate(lavaFlows.geometry):
        #List all the neighbouring units that share a contact with the
            current unit
        listNeighbours = lavaFlows_tree.query(lvf, predicate='intersects')
        listNeighbours = np.delete(listNeighbours, np.where(listNeighbours
            == i)) #Remove the main unit

        #Run the function that will analyze the margins and establish the
            relationship between the units
        listAnalizedMargins.append(build_margins(lvf, lavaFlows,
            listNeighbours, geolContacts, geolContacts_tree))

        #Percentage to keep track of the progress
        if percent:
            currentpercent = 0
            if i/len(lavaFlows.geometry) > currentpercent:
```

```
            print(f"{round(i/len(lavaFlows.geometry) * 100, 2)}% ...",
                end = '\r')

    return listAnalizedMargins

def get_colors_from_colormap(cmap_name, n):
    """
    Create a list of colors that will be used for the plot
    """
    cmap = plt.get_cmap(cmap_name)
    colors = cmap(np.linspace(0, 1, n))
    return colors

def pick_symmetric_numbers(start, stop, num):
    """
    Create a list of numbers separated symmetrically by two numbers
    """
    # Determine the interval size
    interval = (stop - start) / (num - 1)

    # Determine the midpoint
    midpoint = (start + stop) / 2

    # Determine the left and right boundaries
    left_boundary = midpoint - (interval * (num // 2))
    right_boundary = midpoint + (interval * (num // 2))

    # Generate the symmetric numbers
    numbers = np.linspace(left_boundary, right_boundary, num)

    return numbers
```

# Appendix C

# AROMAS Length and Width

```
#### Let's create the list of leaf nodes and calculate their path to the
    top parent node
def find_leaf_nodes(graph):
    leaf_nodes = [node for node in graph.nodes() if
        graph.out_degree(node)==0]
    return leaf_nodes


def findPathToTop(inNode, G):
    topNodes = [node for node in G.nodes if G.nodes[node]['layer'] == 0]

    storePath = list(G.nodes) #Create a long list of nodes

    for topNode in topNodes:
        if nx.has_path(G, topNode, inNode):
            path = nx.shortest_path(G, topNode, inNode, method='dijkstra')
            if len(path)<len(storePath):
                storePath = path
                storeTopNode = topNode

    return storeTopNode

def get_all_vertices(geometry):
    """
    Extract all vertices from a geometry.

    Parameters:
    geometry (shapely.geometry object): The geometry to extract vertices
        from.

    Returns:
    list of Point objects: A list of Point objects representing the vertices.
    """

    vertices = []
```

```
    gdf = gpd.GeoDataFrame(geometry=[geometry],
        crs=currentLava.crs).explode()

    for geom in gdf.geometry:
        if geom.geom_type == 'Polygon':
            for x, y in list(geom.exterior.coords):
                vertices.append(Point(x, y))
        else:
            for x, y in list(geom.coords):
                vertices.append(Point(x, y))

    return vertices

def get_vertices_height(pointsList, raster):
    """
    Get the height of vertices from a raster dataset.

    Parameters:
    pointsList (list of Point objects): List of Point objects representing
        vertices.
    raster (rasterio dataset): The raster dataset used to extract height
        information.

    Returns:
    geopandas.GeoDataFrame: A GeoDataFrame containing the vertices with
        their associated heights.
    """

    verticesHeight = [raster.read(1, window=((raster.index(point.x,
        point.y)[0], raster.index(point.x, point.y)[0] + 1),
                                                (raster.index(point.x,
                                                    point.y)[1],
                                                    raster.index(point.x,
                                                    point.y)[1] + 1))) for point
                                                    in pointsList]

    verticesHeight = [e.item() for e in verticesHeight]

    verticesGDF = gpd.GeoDataFrame(geometry=pointsList, crs=currentLava.crs)
    verticesGDF['height'] = verticesHeight

    return verticesGDF

def getContactPoint(currentLava, lavaFlows, path, neighbourIndex, raster):
    """
    Find the contact point between two geometries and return the highest
        vertex.
```

```
    Parameters:
    currentLava (geopandas.GeoDataFrame): The current lava geometry.
    lavaFlows (geopandas.GeoDataFrame): A dataframe of lava flows.
    path (list of int): Path information.
    neighbourIndex (int): Index of the neighbor.
    raster (rasterio dataset): The raster dataset used for interpolation.

    Returns:
    shapely.geometry.Point: The contact point between the geometries with
        the highest vertex.
    """

    currentLava_geom = currentLava.reset_index().geometry[0]
    neighbour_gdf =
        lavaFlows.loc[lavaFlows['label']=='lvf_'+str(path[neighbourIndex])]
    neighbour_geom = neighbour_gdf.reset_index().geometry[0]
    inter = currentLava_geom.intersection(neighbour_geom)

    contactVertices = get_all_vertices(inter)
    contactVtxGDF = get_vertices_height(contactVertices, raster)
    contactPoint =
        contactVtxGDF.loc[contactVtxGDF['height'].idxmax()].geometry

    return contactPoint

def calculate_perpendicular_endpoint(point, line, offset_distance):
    """
    Calculate the endpoint of a perpendicular line from a point to a line.

    Parameters:
    point (shapely.geometry.Point): The point from which the perpendicular
        line starts.
    line (shapely.geometry.LineString): The line to which the perpendicular
        line is drawn.
    offset_distance (float): The distance between the point and the
        perpendicular line.

    Returns:
    shapely.geometry.Point: The endpoint of the perpendicular line.
    """

    idx = line.project(point)
    next_point = line.interpolate(idx + 0.0001)
    dist, angle = calculate_distance_and_bearing(point, next_point)
    perp_angle = angle + 90.0 if offset_distance > 0 else angle - 90.0
    midPoint = LineString([point, next_point]).centroid
    perp_endpoint = dist.destination(point=(midPoint.y, midPoint.x),
        bearing=perp_angle, distance=abs(offset_distance))
```

```
    return Point(perp_endpoint.longitude, perp_endpoint.latitude)

def calculate_distance_and_bearing(point1, point2):
    """
    Calculate the distance and bearing between two points.

    Parameters:
    point1 (shapely.geometry.Point): The first point.
    point2 (shapely.geometry.Point): The second point.

    Returns:
    tuple: A tuple containing the distance and bearing between the points.
    """

    lat1, lon1 = math.radians(point1.y), math.radians(point1.x)
    lat2, lon2 = math.radians(point2.y), math.radians(point2.x)

    dist = geopy_distance((point1.y, point1.x), (point2.y, point2.x))
    delta_lon = lon2 - lon1
    y = math.sin(delta_lon) * math.cos(lat2)
    x = math.cos(lat1) * math.sin(lat2) - math.sin(lat1) * math.cos(lat2) *
        math.cos(delta_lon)
    bearing = math.atan2(y, x)

    bearing_degrees = math.degrees(bearing)
    bearing_adjusted = (bearing_degrees + 360) % 360

    return dist, bearing_adjusted


def de_casteljau(points, t):
    """
    Use De Casteljau's algorithm to interpolate points along a curve.

    Parameters:
    points (list of tuples): List of control points.
    t (float): Interpolation parameter (0 <= t <= 1).

    Returns:
    tuple: Interpolated point.
    """
    if len(points) == 1:
        return points[0]

    new_points = []
    for i in range(len(points) - 1):
        new_points.append((1 - t) * points[i] + t * points[i + 1])
```

```
    return de_casteljau(new_points, t)

def bezier_curve(points, num_points=100):
    """
    Generate a smooth curve by interpolating points using De Casteljau's
        algorithm.

    Parameters:
    points (list of tuples): Control points that define the shape of the
        curve.
    num_points (int): Number of points to generate for the curve (default is
        100).

    Returns:
    np.ndarray: Array of interpolated points representing the curve.
    """
    # Create an empty numpy array to store the interpolated points'
        coordinates.
    curve = np.zeros((num_points, 2))

    # Iterate over a range of points between 0 and 1 to create the curve.
    for i, t in enumerate(np.linspace(0, 1, num_points)):
        # Use De Casteljau's algorithm to interpolate points along the curve.
        curve[i] = de_casteljau(points, t)
    return curve

def smooth_line(input_line, num_points=100):
    """
    Smooth the input line using bezier curve method.

    parameters:
    input_line: LineString to smooth
    num_points: int. How many points are used to smooth the line
    """
    #Extract the vertices
    points = np.array(input_line.coords)
    #Create new vertices
    smoothed_points = bezier_curve(points, num_points)
    #Create a new line from new vertices
    smoothed_line = LineString(smoothed_points)

    return smoothed_line

def calculateLavaLength(minPoint, maxPoint, currentLava, nbiter = 1,
    distPoints=0.01):
    """
    Function that calculate lava length between two given points for n
        iterations
```

```
parameters:
minPoint, maxPoint: Points between which the length will be calculated
currentLave: Shapely Polygon with the lava to measure
nbiter: Explicit.
distPoints: distance in degrees between to lateral/width lines
"""

#Select the farthest points
farthest1 = maxPoint
farthest2 = minPoint

#Convert to LatLong
pointsGDF = gpd.GeoDataFrame(geometry = [maxPoint, minPoint], crs =
    currentLava.crs).to_crs(mars2000IAU)
lavaGDF = gpd.GeoDataFrame(geometry =
    [currentLava.reset_index().geometry[0]], crs =
    currentLava.crs).to_crs(mars2000IAU)

#Create the first baseline
longLine = LineString([pointsGDF.iloc[0].geometry,
    pointsGDF.iloc[1].geometry])

#Densify the line
distances = [distPoints * i for i in range(int(longLine.length /
    distPoints) + 1)] # 1 deg ~ 59 km => 500 m ~ 0.0084

#List of points on the length line
pointsOnTheLine = [longLine.interpolate(d) for d in distances]

#Iterate several times for various results
for gen in range(nbiter):
    #Creating perpendicular lines
    wideLines = [LineString([calculate_perpendicular_endpoint(point,
        longLine, 500), calculate_perpendicular_endpoint(point,
        longLine, -500)]) for point in pointsOnTheLine]

    #Clip the lines by the polygon
    listInter=[]
    for line in wideLines:
        intersection = line.intersection(lavaGDF.geometry[0])
        if intersection.geom_type == 'MultiLineString':
            intersection = max(list(intersection.geoms), key=lambda part:
                part.length)
        if not intersection.is_empty:
            listInter.append(intersection)

    #Store the wide lines
```

```
        wideLinesGDF = gpd.GeoDataFrame(geometry = listInter, crs =
            mars2000IAU)

        #Get the center of each wide lines
        newList = list(wideLinesGDF.centroid)
        newList.insert(0, pointsGDF.iloc[0].geometry) #The first point
        newList.append(pointsGDF.iloc[1].geometry) #The last point of the
            old list

        #Creating centroids
        pointsOnTheLine = newList

        #Creating the new longLine
        longLine = LineString(pointsOnTheLine)

        #Smoothing the line using bezier curve
        smoothed_line = smooth_line(longLine, num_points=100)

        #Reasign the longLine for the next iteration
        longLine = smoothed_line

        #Select the same number of points as on the original Line string
        pointsOnTheLine = [longLine.interpolate(d) for d in distances]

    return longLine, wideLinesGDF
```

# Appendix D

# AROMAS Thickness

```
def prepareMolaData(lvf, molaShots):

    #Create a buffer zone
    buffLava = lvf.buffer(500)

    #Select the MOLA points within the margin
    selectedPoints = gpd.sjoin(molaShots_proj,
        gpd.GeoDataFrame(geometry=[buffLava], crs = lavaFlows.crs) ,
        how="inner", predicate="within")

    # Create an empty dictionary to store the groups of points
    groupedPoints = {}

    # Identify breaks in the index sequence
    breaks = np.where(np.diff(selectedPoints.index) != 1)[0] + 1
    if len(breaks) > 0:
        # If there are breaks, the first group starts at the first index and
            ends at the first break
        groupedPoints[0] = selectedPoints.iloc[0:breaks[0]]

        # Then we create a group for each pair of breaks
        for i in range(len(breaks) - 1):
            groupedPoints[i+1] = selectedPoints.iloc[breaks[i]:breaks[i+1]]

        # The last group starts at the last break and goes to the end of the
            DataFrame
        groupedPoints[len(breaks)] = selectedPoints.iloc[breaks[-1]:]
    else:
        # If there are no breaks, the entire DataFrame is one group
        groupedPoints[0] = selectedPoints

    return groupedPoints
```

# Appendix E

# AROMAS Fractal Dimension

---

```
def findNextPointOnLine(currentPointIdx, margin, distance):
    """
    Finds the next point on the margin at the rod distance.

    Parameters:
    -currentPointIdx: index of the point in the list of vertices in the
        margin
    -margin: Shapely LineString with the input margin.
    -distance: in meters, where to search for the next point.
    """
    #To check whether the next point was found
    found = False

    #Iterate vertices from the current index
    for i, vertex in enumerate(margin.coords[currentPointIdx:]):

        #How far is the next point on the margin
        currentDistance =
            Point(vertex).distance(Point(margin.coords[currentPointIdx]))

        #Have we passed the point?
        if distance < currentDistance:
            #We passed the point
            found = True
            return vertex, i+currentPointIdx

    #No point found, we are beyond the margin length
    if not found:
        return None, None

def createMarginForFractal(margin, rod_length):
    """
    Function called in the main which creates a new version
    of the margin using a rod
```

```
    Parameters:
    margin: Shapely LineString with the input margin.
    rod_length: int. Explicit.
    """
    #Create a variable which will contain the next point on the margin at
        the rod distance
    nextPoint = Point(margin.coords[0]) #Initiate it with the first point
    currentPointIdx = 0 #Store the index
    listVertices=[] # Keep the creates vertices in a list

    #While a next point is found (i.e. not the end of the margin)
    while nextPoint:
        #Add the point to the list
        listVertices.append(nextPoint)

        #Try to find the next point with respect to the current point index
        nextPoint, currentPointIdx = findNextPointOnLine(currentPointIdx,
            margin, rod_length)

    #At least 1 vertex
    if len(listVertices)>1:
        return LineString(listVertices) #Create a LineString from the list
            of points
    else:
        return None

def calculateFractalDimension(natMargin, minRodLength=500,
    maxRodLength=4000, nbRodLengths = 4, plot=False):
    """
    Calculate the fractal dimension of an input margin following Bruno et
        al. 1992, 1994.

    Parameters:
    - natMargin: Shapely LineString with the input margin.
    - minRodLength: int with minimum length used for the computation.
    - maxRodLength: int with maximum length used for the computation.
    - plot: Boolean. Choose whether or not to display the plots.
    """

    #--------------------------------------------------------------------
    ### First we need to digitzed the margin at different "scale" using
    ### various rod lengths in order
    #--------------------------------------------------------------------

    #Create a list integers logarithmically spaced with the various rod
        lengths
    rod_lengths = np.rint(np.logspace(math.log10(minRodLength),
        math.log10(maxRodLength), nbRodLengths))
```

```
#Create empty lists to store results
listMargins = [] #To store the margins creates at each iteration (i.e.
    for each rod length)
total_length_log = [] #Log of the length of the margin
total_length = [] # Length of the margin
rod_length_log = [] #Log of the rod length

#Iterate the rod lengths
for rod_length in rod_lengths:
    margin = None #Clear previous margin

    #Digitize, if possible, a new margin using this specific rod length
    margin = createMarginForFractal(natMargin, rod_length)

    #Check whether a margin could be digitzed
    if margin:
        #Store the results
        total_length_log.append(math.log10(margin.length))
        total_length.append(margin.length)
        rod_length_log.append(math.log10(rod_length))
        listMargins.append(margin)
    else:
        #Add a None to keep the lists the same size as lavaFlows
        rod_length_log.append(None)
        total_length_log.append(None)
        total_length.append(None)

#-----------------------------------------------------
### Now we plot the data and try to fit a linear function in loglog
### to compute the fractal dimension (i.e. 1 - the slope of this
    function).
#-----------------------------------------------------

#Create X and Y lists in log scale removing the None values
x_log = [point for point in rod_length_log if point is not None]
y_log = [point for point in total_length_log if point is not None]

#Fit a linear function to x and y
coefficients_log = np.polyfit(x_log, y_log, 1)
poly_log = np.poly1d(coefficients_log) #Store the fitting coefficient
y_fit_log = poly_log(x_log) #Create Y values with the fitted function

# Calculate the correlation coefficient R2
correlation_matrix = np.corrcoef(x_log, y_log)
correlation_coefficient = pow(correlation_matrix[0, 1],2)

# Plot the results if plot == True
```

```
    if plot:
        fig, axs = plt.subplots(1, 2, figsize = (15*cm, 8*cm))
        axs[0].grid(visible=True, which='both', axis='both')
        axs[0].plot(x_log, y_log, 'o') #The data
        axs[0].plot(x_log, y_fit_log, 'r--') #The fitted function
        axs[0].set_xlabel('Rod Length (m)', fontsize = 11)
        axs[0].set_ylabel('Total Length (m)', fontsize = 11)
        axs[0].tick_params(axis='x', which='both', rotation =90)
        axs[0].annotate('R2: '+str(round(correlation_coefficient,
            3))+'\n'+'Fract. Dim.: '+str(round(1-coefficients_log[0], 3)),
                   [0.7, 0.7], xycoords='axes fraction') # Display the corr.
                       coef.
        axs[0].set_title('Length of the margin:
            '+str(round(natMargin.length))+' m')

        #---------------------------------
        ### Plot the map to show the digitized margins
        #---------------------------------

        #Create a GeoDataFrame
        marginsGDF = gpd.GeoDataFrame(geometry=listMargins) #Store the
            margins
        marginsGDF['rod_lengths'] = [round(pow(10, logRod)) for logRod in
            x_log] #add rod length to the table
        marginsGDF.plot(ax=axs[1], column='rod_lengths', linestyle=':',
            categorical=True, legend = True)
        leg = axs[1].get_legend()
        leg.set_bbox_to_anchor((0.9,-0.1))
        axs[1].add_artist(ScaleBar(1))
        axs[1].set_axis_off()

        fig.tight_layout()

    #Return the Fractal Dimension and the Correlation coefficient
    return 1-coefficients_log[0], correlation_coefficient

def fractalDimensionForLavaFlows(margins):
    """
    Input a list of margins (from the GDF of lava flows for instance)
    and output lists the same lenghts as input with the fractal dimension
    and the corresponding correlation coeffictient

    Parameters:
    - margins: list of Shapely Linestrings with margins
    """

    #Empty lists to store outpits
    fractDim_list = []
```

```
    corrCoef_list = []

    #Iterate the margins
    for lvf in margins:
        #Check if the flow has compatible margins
        if lvf:
            #If several margins for one flow
            if len(lvf)>1:
                #Compute the mean
                fractMean = []
                corrMean = []
                for margin in lvf:
                    if margin.length > 8000:
                        fractDim, corrCoef = calculateFractalDimension(margin)
                        fractMean.append(fractDim)
                        corrMean.append(corrCoef)
                if len(fractMean) == 0:
                    fractDim_list.append(None)
                    corrCoef_list.append(None)
                else:
                    fractDim_list.append(sum(fractMean)/len(fractMean))
                    corrCoef_list.append(sum(corrMean)/len(corrMean))
            else:
                if lvf[0].length > 8000:
                    fractDim, corrCoef = calculateFractalDimension(lvf[0])
                    fractDim_list.append(fractDim)
                    corrCoef_list.append(corrCoef)
                else:
                    fractDim_list.append(None)
                    corrCoef_list.append(None)
        else:
            fractDim_list.append(None)
            corrCoef_list.append(None)

    return fractDim_list, corrCoef_list
```

# Bibliography


Adams, N. K., Houghton, B. F., Fagents, S. A., & Hildreth, W. (2006). The transition from explosive to effusive eruptive regime: The example of the 1912 Novarupta eruption, Alaska. *Geological Society of America Bulletin*, *118*(5-6), 620–634. https://doi.org/10.1130/B25768.1

Albee, A. L., Arvidson, R. E., Palluconi, F., & Thorpe, T. (2001). Overview of the Mars Global Surveyor mission. *Journal of Geophysical Research: Planets*, *106*(E10), 23291–23316. https://doi.org/10.1029/2000JE001306

Anderson, R. C., Dohm, J. M., Golombek, M. P., Haldemann, A. F. C., Franklin, B. J., Tanaka, K. L., Lias, J., & Peer, B. (2001). Primary centers and secondary concentrations of tectonic activity through time in the western hemisphere of Mars. *Journal of Geophysical Research: Planets*, *106*(E9), 20563–20585. https://doi.org/10.1029/2000JE001278

Baloga, S. M. (2003). Rheology of a long lava flow at Pavonis Mons, Mars. *Journal of Geophysical Research*, *108*(E7), 5066. https://doi.org/10.1029/2002JE001981

Banin, A., Clark, B. C., & Waenke, H. (1992, January). *Surface chemistry and mineralogy.* ADS Bibcode: 1992mars.book..594B.

Baratoux, D., Toplis, M. J., Monnereau, M., & Gasnault, O. (2011). Thermal history of Mars inferred from orbital geochemistry of volcanic provinces. *Nature*, *472*(7343), 338–341. https://doi.org/10.1038/nature09903

Becerril, L., Marti, J., Bartolini, S., & Geyer, A. (2017). Assessing qualitative long-term volcanic hazards at Lanzarote Island (Canary Islands). *Natural Hazards and Earth System Sciences*, *17*(7), 1145–1157. https://doi.org/10.5194/nhess-17-1145-2017

Beyer, R. A., Alexandrov, O., & McMichael, S. (2018). The Ames Stereo Pipeline: NASA's Open Source Software for Deriving and Processing Terrain Data. *Earth and Space Science*, *5*(9), 537–548. https://doi.org/10.1029/2018EA000409

Bickel, V. T., Conway, S. J., Tesson, P.-A., Manconi, A., Loew, S., & Mall, U. (2020). Deep Learning-Driven Detection and Mapping of Rockfalls on Mars. *IEEE Journal of Selected Topics in Applied Earth Observations and Remote Sensing*, *13*, 2831–2841. https://doi.org/10.1109/JSTARS.2020.2991588

Bistacchi, N., Massironi, M., & Baggio, P. (2004). Large-scale fault kinematic analysis in Noctis Labyrinthus (Mars). *Planetary and Space Science*, *52*(1-3), 215–222. https://doi.org/10.1016/j.pss.2003.08.015

Bleacher, J. E., Greeley, R., Williams, D. A., Cave, S. R., & Neukum, G. (2007). Trends in effusive style at the Tharsis Montes, Mars, and implications for the development of the Tharsis province. *Journal of Geophysical Research*, *112*(E9), E09005. https://doi.org/10.1029/2006JE002873

Bleacher, J. E., Orr, T. R., De Wet, A. P., Zimbelman, J. R., Hamilton, C. W., Brent Garry, W., Crumpler, L. S., & Williams, D. A. (2017). Plateaus and sinuous ridges as the fingerprints of lava flow inflation in the Eastern Tharsis Plains of Mars. *Journal of Volcanology and Geothermal Research*, *342*, 29–46. https://doi.org/10.1016/j.jvolgeores.2017.03.025

Boehm, W., & Müller, A. (1999). On de Casteljau's algorithm. *Computer Aided Geometric Design*, *16*(7), 587–605. https://doi.org/10.1016/S0167-8396(99)00023-0

Bouley, S., Baratoux, D., Matsuyama, I., Forget, F., Séjourné, A., Turbet, M., & Costard, F. (2016). Late Tharsis formation and implications for early Mars. *Nature*, *531*(7594), 344–347. https://doi.org/10.1038/nature17171

Bouley, S., Baratoux, D., Paulien, N., Missenard, Y., & Saint-Bézar, B. (2018). The revised tectonic history of Tharsis. *Earth and Planetary Science Letters*, *488*, 126–133. https://doi.org/10.1016/j.epsl.2018.02.019

Boynton, W. V., Feldman, W. C., Squyres, S. W., Prettyman, T. H., Brückner, J., Evans, L. G., Reedy, R. C., Starr, R., Arnold, J. R., Drake, D. M., Englert, P. A. J., Metzger, A. E., Mitrofanov, I., Trombka, J. I., d'Uston, C., Wänke, H., Gasnault, O., Hamara, D. K., Janes, D. M., … Shinohara, C. (2002). Distribution of Hydrogen in the Near Surface of Mars: Evidence for Subsurface Ice Deposits. *Science*, *297*(5578), 81–85. https://doi.org/10.1126/science.1073722

Breuer, D., Yuen, D. A., Spohn, T., & Zhang, S. (1998). Three dimensional models of Martian mantle convection with phase transitions. *Geophysical Research Letters*, *25*(3), 229–232. https://doi.org/10.1029/97GL03767

Bridges, N., Banks, M., Beyer, R., Chuang, F., Dobrea, E. N., Herkenhoff, K., Keszthelyi, L., Fishbaugh, K., McEwen, A., Michaels, T., Thomson, B., & Wray, J. (2010). Aeolian bedforms, yardangs, and indurated surfaces in the Tharsis Montes as seen by the HiRISE Camera: Evidence for dust aggregates. *Icarus*, *205*(1), 165–182. https://doi.org/10.1016/j.icarus.2009.05.017

Broquet, A., & Andrews-Hanna, J. C. (2022). Geophysical evidence for an active mantle plume underneath Elysium Planitia on Mars. *Nature Astronomy*. https://doi.org/10.1038/s41550-022-01836-3

Brož, P., & Hauber, E. (2012). A unique volcanic field in Tharsis, Mars: Pyroclastic cones as evidence for explosive eruptions. *Icarus*, *218*(1), 88–99. https://doi.org/10.1016/j.icarus.2011.11.030

Brož, P., & Hauber, E. (2013). Hydrovolcanic tuff rings and cones as indicators for phreatomagmatic explosive eruptions on Mars: PHREATOMAGMATIC ERUPTIONS ON MARS. *Journal of Geophysical Research: Planets*, *118*(8), 1656–1675. https://doi.org/10.1002/jgre.20120

Brož, P., Bernhardt, H., Conway, S. J., & Parekh, R. (2021). An overview of explosive volcanism on Mars. *Journal of Volcanology and Geothermal Research*, *409*, 107125. https://doi.org/10.1016/j.jvolgeores.2020.107125

Bruno, B. C., Taylor, G. J., Rowland, S. K., & Baloga, S. M. (1994). Quantifying the effect of rheology on lava-flow margins using fractal geometry. *Bulletin of Volcanology*, *56*(3), 193–206. https://doi.org/10.1007/BF00279604

Bruno, B. C., Taylor, G. J., Rowland, S. K., Lucey, P. G., & Self, S. (1992). Lava flows are fractals. *Geophysical Research Letters*, *19*(3), 305–308. https://doi.org/10.1029/91GL03039

Carr, M. H., Masursky, H., & Saunders, R. S. (1973). A generalized geologic map of Mars. *Journal of Geophysical Research*, *78*(20), 4031–4036. https://doi.org/10.1029/JB078i020p04031

Carr, M. H. (1973). Volcanism on Mars. *Journal of Geophysical Research*, *78*(20), 4049–4062. https://doi.org/10.1029/JB078i020p04049

Carr, M. H. (1974). Tectonism and volcanism of the Tharsis Region of Mars. *Journal of Geophysical Research*, *79*(26), 3943–3949. https://doi.org/10.1029/JB079i026p03943

Carracedo, J. C., Day, S., Guillou, H., Rodríguez Badiola, E., Canas, J. A., & Pérez Torrado, F. J. (1998). Hotspot volcanism close to a passive continental margin: The Canary Islands. *Geological Magazine*, *135*(5), 591–604. https://doi.org/10.1017/S0016756898001447

Carracedo, J. C., Troll, V. R., Day, J. M. D., Geiger, H., Aulinas, M., Soler, V., Deegan, F. M., Perez-Torrado, F. J., Gisbert, G., Gazel, E., Rodriguez-Gonzalez, A., & Albert, H. (2022). The 2021 eruption of the Cumbre Vieja volcanic ridge on La Palma, Canary Islands. *Geology Today*, *38*(3), 94–107. https://doi.org/10.1111/gto.12388

Cassidy, M., Manga, M., Cashman, K., & Bachmann, O. (2018). Controls on explosive-effusive volcanic eruption styles. *Nature Communications*, *9*(1), 2839. https://doi.org/10.1038/s41467-018-05293-3

Chapman, M. G., Neukum, G., Dumke, A., Michael, G., Van Gasselt, S., Kneissl, T., Zuschneid, W., Hauber, E., Ansan, V., Mangold, N., & Masson, P. (2010). Noachian–Hesperian geologic history of the Echus Chasma and Kasei Valles system on Mars: New data and interpretations. *Earth and Planetary Science Letters*, *294*(3-4), 256–271. https://doi.org/10.1016/j.epsl.2009.11.032

Chevrel, M. O., Favalli, M., Villeneuve, N., Harris, A. J. L., Fornaciai, A., Richter, N., Derrien, A., Boissier, P., Di Muro, A., & Peltier, A. (2021). Lava flow hazard map of Piton de la Fournaise volcano. *Natural Hazards and Earth System Sciences*, *21*(8), 2355–2377. https://doi.org/10.5194/nhess-21-2355-2021

Chevrel, M. O., Platz, T., Hauber, E., Baratoux, D., Lavallée, Y., & Dingwell, D. (2013). Lava flow rheology: A comparison of morphological and petrological methods. *Earth and Planetary Science Letters*, *384*, 109–120. https://doi.org/10.1016/j.epsl.2013.09.022

Chicarro, A., Martin, P., & Trautner, R. (2004). The Mars Express mission: An overview. *1240*, 3–13
ADS Bibcode: 2004ESASP1240....3C.

Chojnacki, M., Fenton, L. K., Weintraub, A. R., Edgar, L. A., Jodhpurkar, M. J., & Edwards, C. S. (2020). Ancient Martian Aeolian Sand Dune Deposits Recorded in the Stratigraphy of Valles Marineris and Implications for Past Climates. *Journal of Geophysical Research: Planets*, *125*(9), e2020JE006510. https://doi.org/10.1029/2020JE006510

Christensen, P. R., Engle, E., Anwar, S., Dickenshied, S., Noss, D., Gorelick, N., & Weiss-Malik, M. (2009). JMARS - A Planetary GIS. *2009*, IN22A–06
ADS Bibcode: 2009AGUFMIN22A..06C.

Christensen, P. R., Jakosky, B. M., Kieffer, H. H., Malin, M. C., McSween, H. Y., Nealson, K., Mehall, G. L., Silverman, S. H., Ferry, S., Caplinger, M., et al. (2004). The thermal emission imaging system (THEMIS) for the Mars 2001 Odyssey Mission. *Space Science Reviews*, *110*(1), 85–130.

Clapham, M. E., & Renne, P. R. (2019). Flood Basalts and Mass Extinctions. *Annual Review of Earth and Planetary Sciences*, *47*(1), 275–303. https://doi.org/10.1146/annurev-earth-053018-060136

Coello, J., Cantagrel, J.-M., Hernán, F., Fúster, J.-M., Ibarrola, E., Ancochea, E., Casquet, C., Jamond, C., Díaz De Téran, J.-R., & Cendrero, A. (1992). Evolution of the eastern volcanic ridge of the Canary Islands based on new K-Ar data. *Journal of Volcanology and Geothermal Research*, *53*(1-4), 251–274. https://doi.org/10.1016/0377-0273(92)90085-R

Corradino, C., Ganci, G., Cappello, A., Bilotta, G., Hérault, A., & Del Negro, C. (2019). Mapping Recent Lava Flows at Mount Etna Using Multispectral Sentinel-2 Images and Machine Learning Techniques. *Remote Sensing*, *11*(16), 1916. https://doi.org/10.3390/rs11161916

Costa, M. M., Jensen, N. K., Bouvier, L. C., Connelly, J. N., Mikouchi, T., Horstwood, M. S. A., Suuronen, J.-P., Moynier, F., Deng, Z., Agranier, A., Martin, L. A. J., Johnson, T. E., Nemchin, A. A., & Bizzarro, M. (2020). The internal structure and geodynamics of Mars inferred from a 4.2-Gyr zircon record. *Proceedings of the National Academy of Sciences*, *117*(49), 30973–30979. https://doi.org/10.1073/pnas.2016326117

Crown, D. A., & Ramsey, M. S. (2017). Morphologic and thermophysical characteristics of lava flows southwest of Arsia Mons, Mars. *Journal of Volcanology and Geothermal Research*, *342*, 13–28. https://doi.org/10.1016/j.jvolgeores.2016.07.008

Crumpler, L., & Aubele, J. (1978). Structural evolution of Arsia Mons, Pavonis Mons, and Ascreus Mons: Tharsis region of Mars. *Icarus*, *34*(3), 496–511. https://doi.org/10.1016/0019-1035(78)90041-6

Day, M., & Zimbelman, J. R. (2021). Ripples, megaripples, and TARs, Oh, My! Recommendations regarding Mars aeolian bedform terminology. *Icarus*, *369*, 114647. https://doi.org/10.1016/j.icarus.2021.114647

Dickson, J. L., Kerber, L. A., Fassett, C. I., & Ehlmann, B. L. (2018). A Global, Blended CTX Mosaic of Mars with Vectorized Seam Mapping: A New Mosaicking Pipeline Using Principles of Non-Destructive Image Editing, 2480
ADS Bibcode: 2018LPI....49.2480D.

Doute, S., & Jiang, C. (2020). Small-Scale Topographical Characterization of the Martian Surface With In-Orbit Imagery. *IEEE Transactions on Geoscience and Remote Sensing*, *58*(1), 447–460. https://doi.org/10.1109/TGRS.2019.2937172

Dundas, C. M., Bramson, A. M., Ojha, L., Wray, J. J., Mellon, M. T., Byrne, S., McEwen, A. S., Putzig, N. E., Viola, D., Sutton, S., Clark, E., & Holt, J. W. (2018). Exposed subsurface ice sheets in the Martian mid-latitudes. *Science*, *359*(6372), 199–201. https://doi.org/10.1126/science.aao1619

ESRI Shapefile Technical Description. (1998).

Farmer, C. B. (1976). Liquid water on Mars. *Icarus*, *28*(2), 279–289. https://doi.org/10.1016/0019-1035(76)90038-5

Fergason, R. L., Christensen, P. R., & Kieffer, H. H. (2006). High-resolution thermal inertia derived from the Thermal Emission Imaging System (THEMIS): Thermal model and applications. *Journal of Geophysical Research: Planets*, *111*(E12), 2006JE002735. https://doi.org/10.1029/2006JE002735

Forget, F., Wordsworth, R., Millour, E., Madeleine, J.-B., Kerber, L., Leconte, J., Marcq, E., & Haberle, R. (2013). 3D modelling of the early martian climate under a denser CO2 atmosphere: Temperatures and CO2 ice clouds. *Icarus*, *222*(1), 81–99. https://doi.org/10.1016/j.icarus.2012.10.019

Gaddis, L., Anderson, J., Becker, K., Becker, T., Cook, D., Edwards, K., Eliason, E., Hare, T., Kieffer, H., Lee, E. M., Mathews, J., Soderblom, L., Sucharski, T., Torson, J., McEwen, A., & Robinson, M. (1997). An Overview of the Integrated Software for Imaging Spectrometers (ISIS), 387
ADS Bibcode: 1997LPI....28..387G.

Ganesh, I., Carter, L. M., & Smith, I. B. (2020). SHARAD mapping of Arsia Mons caldera. *Journal of Volcanology and Geothermal Research*, *390*, 106748. https://doi.org/10.1016/j.jvolgeores.2019.106748

Geldmacher, J., Hoernle, K., Van Den Bogaard, P., Zankl, G., & Garbe-Schönberg, D. (2001). Earlier history of the >70-Ma-old Canary hotspot based on the temporal and geochemical evolution of the Selvagen Archipelago and neighboring seamounts in the eastern North Atlantic. *Journal of Volcanology and Geothermal Research*, *111*(1-4), 55–87. https://doi.org/10.1016/S0377-0273(01)00220-7

Giacomini, L., Massironi, M., Martellato, E., Pasquarè, G., Frigeri, A., & Cremonese, G. (2009). Inflated flows on Daedalia Planum (Mars)? Clues from a comparative analysis with the Payen volcanic complex (Argentina). *Planetary and Space Science*, *57*(5-6), 556–570. https://doi.org/10.1016/j.pss.2008.12.001

Giardini, D., Lognonné, P., Banerdt, W. B., Pike, W. T., Christensen, U., Ceylan, S., Clinton, J. F., van Driel, M., Stähler, S. C., Böse, M., Garcia, R. F., Khan, A., Panning, M., Perrin, C., Banfield, D., Beucler, E., Charalambous, C., Euchner, F., Horleston, A., … Yana, C. (2020). The seismicity of Mars. *Nature Geoscience*, *13*(3), 205–212. https://doi.org/10.1038/s41561-020-0539-8

Gillies, S., van der Wel, C., Van den Bossche, J., Taves, M. W., Arnott, J., & Ward, B. C. (2023, October). Shapely. https://doi.org/10.5281/ZENODO.5597138

Glaze, L. S., & Baloga, S. M. (2002). Volcanic plume heights on Mars: Limits of validity for convective models. *Journal of Geophysical Research: Planets*, *107*(E10). https://doi.org/10.1029/2001JE001830

Greeley, R. (1982). The Snake River Plain, Idaho: Representative of a new category of volcanism. *Journal of Geophysical Research*, *87*(B4), 2705. https://doi.org/10.1029/JB087iB04p02705

Greeley, R., & Schneid, B. D. (1991). Magma Generation on Mars: Amounts, Rates, and Comparisons with Earth, Moon, and Venus. *Science*, *254*(5034), 996–998. https://doi.org/10.1126/science.254.5034.996

Greeley, R., & Spudis, P. D. (1981). Volcanism on Mars. *Reviews of Geophysics*, *19*(1), 13. https://doi.org/10.1029/RG019i001p00013

Grott, M., Morschhauser, A., Breuer, D., & Hauber, E. (2011). Volcanic outgassing of CO2 and H2O on Mars. *Earth and Planetary Science Letters*, *308*(3-4), 391–400. https://doi.org/10.1016/j.epsl.2011.06.014

Halevy, I., & Head III, J. W. (2014). Episodic warming of early Mars by punctuated volcanism. *Nature Geoscience*, *7*(12), 865–868. https://doi.org/10.1038/ngeo2293

Hamilton, C. W., Mouginis-Mark, P. J., Sori, M. M., Scheidt, S. P., & Bramson, A. M. (2018). Episodes of Aqueous Flooding and Effusive Volcanism Associated With Hrad Vallis, Mars. *Journal of Geophysical Research: Planets*, *123*(6), 1484–1510. https://doi.org/10.1029/2018JE005543

Harris, A. J. L., Rowland, S. K., Villeneuve, N., & Thordarson, T. (2017). Pāhoehoe, ʻaʻā, and block lava: An illustrated history of the nomenclature. *Bulletin of Volcanology*, *79*(1), 7. https://doi.org/10.1007/s00445-016-1075-7

Hartmann, W. K., & Daubar, I. J. (2017a). Martian cratering 11. Utilizing decameter scale crater populations to study Martian history. *Meteoritics & Planetary Science*, *52*(3), 493–510. https://doi.org/10.1111/maps.12807

Hartmann, W. K., & Daubar, I. J. (2017b). Martian cratering 11. Utilizing decameter scale crater populations to study Martian history. *Meteoritics & Planetary Science*, *52*(3), 493–510. https://doi.org/10.1111/maps.12807

Hartmann, W. K. (1973). Martian surface and crust: Review and synthesis. *Icarus*, *19*(4), 550–575. https://doi.org/10.1016/0019-1035(73)90083-3

Hartmann, W. K. (2005). Martian cratering 8: Isochron refinement and the chronology of Mars. *Icarus*, *174*(2), 294–320. https://doi.org/10.1016/j.icarus.2004.11.023

Hauber, E., Brož, P., Jagert, F., Jodłowski, P., & Platz, T. (2011). Very recent and widespread basaltic volcanism on Mars: RECENT WIDE-SPREAD VOLCANISM ON MARS. *Geophysical Research Letters*, *38*(10), n/a–n/a. https://doi.org/10.1029/2011GL047310

Hauber, E., Bleacher, J., Gwinner, K., Williams, D., & Greeley, R. (2009). The topography and morphology of low shields and associated landforms of plains volcanism in the Tharsis region of Mars. *Journal of Volcanology and Geothermal Research*, *185*(1-2), 69–95. https://doi.org/10.1016/j.jvolgeores.2009.04.015

Head, J. W., & Marchant, D. R. (2003). Cold-based mountain glaciers on Mars: Western Arsia Mons. *Geology*, *31*(7), 641. https://doi.org/10.1130/0091-7613(2003)031<0641:CMGOMW>2.0.CO;2

Hecht, M. (2002). Metastability of Liquid Water on Mars. *Icarus*, *156*(2), 373–386. https://doi.org/10.1006/icar.2001.6794

Hiesinger, H., van der Bogert, C. H., Pasckert, J. H., Funcke, L., Giacomini, L., Ostrach, L. R., & Robinson, M. S. (2012). How old are young lunar craters?: HOW OLD ARE YOUNG LUNAR CRATERS? *Journal of Geophysical Research: Planets*, *117*(E12), n/a–n/a. https://doi.org/10.1029/2011JE003935

Hodges, C. A., & Moore, H. J. (1994, January). *Atlas of volcanic landforms on Mars*. ADS Bibcode: 1994avlm.book.....H.

Hoehler, T. M., Som, S. M., & Kiang, N. Y. (2018). Life's Requirements. In H. J. Deeg & J. A. Belmonte (Eds.), *Handbook of Exoplanets* (pp. 1–22). Springer International Publishing. https://doi.org/10.1007/978-3-319-30648-3_74-1

Hoernle, K., & Carracedo, J. C. (2009). Canary Islands geology. In *Encyclopedia of Islands* (pp. 133–143). University of California Press.

Hon, K., Gansecki, C., & Kauahikaua, J. (2003). The transition from 'a 'ā to pāhoehoe crust on flows emplaced during the Pu 'u 'Ō 'ō-Kūpaianaha eruption. *US Geological Survey Professional Paper*, *1676*(1676), 89.

Horvath, D. G., Moitra, P., Hamilton, C. W., Craddock, R. A., & Andrews-Hanna, J. C. (2021). Evidence for geologically recent explosive volcanism in Elysium Planitia, Mars. *Icarus*, *365*, 114499. https://doi.org/10.1016/j.icarus.2021.114499

Hugenholtz, C. H., & Barchyn, T. E. (2010). Spatial analysis of sand dunes with a new global topographic dataset: New approaches and opportunities. *Earth Surface Processes and Landforms*, *35*(8), 986–992. https://doi.org/10.1002/esp.2013

Hulme, G. (1976). The determination of the rheological properties and effusion rate of an Olympus Mons lava. *Icarus*, *27*(2), 207–213. https://doi.org/10.1016/0019-1035(76)90004-X

Jiang, C., Douté, S., Luo, B., & Zhang, L. (2017). Fusion of photogrammetric and photoclinometric information for high-resolution DEMs from Mars in-orbit imagery. *ISPRS Journal of Photogrammetry and Remote Sensing*, *130*, 418–430. https://doi.org/10.1016/j.isprsjprs.2017.06.010

Jordahl, K., Bossche, J. V. D., Fleischmann, M., Wasserman, J., McBride, J., Gerard, J., Tratner, J., Perry, M., Badaracco, A. G., Farmer, C., Hjelle, G. A., Snow, A. D., Cochran, M., Gillies, S., Culbertson, L., Bartos, M., Eubank, N., Maxalbert, Bilogur, A., … Leblanc, F. (2020, July). Geopandas/geopandas: V0.8.1. https://doi.org/10.5281/ZENODO.3946761

Kerber, L., Forget, F., Madeleine, J.-B., Wordsworth, R., Head, J. W., & Wilson, L. (2013). The effect of atmospheric pressure on the dispersal of pyroclasts from martian volcanoes. *Icarus*, *223*(1), 149–156. https://doi.org/10.1016/j.icarus.2012.11.037

Keszthelyi, L., & McEwen, A. (2007, May). Comparison of flood lavas on Earth and Mars. In M. Chapman (Ed.), *The Geology of Mars* (1st ed., pp. 126–150). Cambridge University Press. https://doi.org/10.1017/CBO9780511536014.006

Kite, E. S., Sneed, J., Mayer, D. P., Lewis, K. W., Michaels, T. I., Hore, A., & Rafkin, S. C. R. (2016). Evolution of major sedimentary mounds on Mars: Buildup via anticompensational stacking modulated by climate change. *Journal of Geophysical Research: Planets*, *121*(11), 2282–2324. https://doi.org/10.1002/2016JE005135

Kling, C. L., Byrne, P. K., Atkins, R. M., & Wegmann, K. W. (2021). Tectonic Deformation and Volatile Loss in the Formation of Noctis Labyrinthus, Mars. *Journal of Geophysical Research: Planets*, *126*(11), e2020JE006555. https://doi.org/10.1029/2020JE006555

Kolzenburg, S., Jaenicke, J., Münzer, U., & Dingwell, D. (2018). The effect of inflation on the morphology-derived rheological parameters of lava flows and its implications for interpreting remote sensing data - A case study on the 2014/2015 eruption at Holuhraun, Iceland. *Journal of Volcanology and Geothermal Research*, *357*, 200–212. https://doi.org/10.1016/j.jvolgeores.2018.04.024

Kuntz, M. A., Spiker, E. C., Rubin, M., Champion, D. E., & Lefebvre, R. H. (1986). Radiocarbon Studies of Latest Pleistocene and Holocene Lava Flows of the Snake River Plain, Idaho: Data, Lessons, Interpretations. *Quaternary Research*, *25*(2), 163–176. https://doi.org/10.1016/0033-5894(86)90054-2

Kusanagi, T., & Matsui, T. (2000). The change of eruption styles of Martian volcanoes and estimates of the water content of the Martian mantle. *Physics of the Earth and Planetary Interiors*, *117*(1-4), 437–447. https://doi.org/10.1016/S0031-9201(99)00112-0

Kussul, N., Lavreniuk, M., Skakun, S., & Shelestov, A. (2017). Deep Learning Classification of Land Cover and Crop Types Using Remote Sensing Data. *IEEE Geoscience and Remote Sensing Letters*, *14*(5), 778–782. https://doi.org/10.1109/LGRS.2017.2681128

Ladd, J. R., Otis, J., Warren, C. N., & Weingart, S. (2017). Exploring and Analyzing Network Data with Python (B. Walsh, Ed.). *Programming Historian*, (6). https://doi.org/10.46430/phen0064

Le Deit, L., Bourgeois, O., Mège, D., Hauber, E., Le Mouélic, S., Massé, M., Jaumann, R., & Bibring, J.-P. (2010). Morphology, stratigraphy, and mineralogical composition of a layered formation covering the plateaus around Valles Marineris, Mars: Implications for its geological history. *Icarus*, *208*(2), 684–703. https://doi.org/10.1016/j.icarus.2010.03.012

Lee, C. (2019). Automated crater detection on Mars using deep learning. *Planetary and Space Science*, *170*, 16–28. https://doi.org/10.1016/j.pss.2019.03.008

Lodders, K. (1998). A survey of shergottite, nakhlite and chassigny meteorites whole-rock compositions. *Meteoritics & Planetary Science*, *33*(S4), A183–A190. https://doi.org/10.1111/j.1945-5100.1998.tb01331.x

Lopez, T., Antoine, R., Baratoux, D., Rabinowicz, M., Kurita, K., & d'Uston, L. (2012). Thermal anomalies on pit craters and sinuous rilles of Arsia Mons: Possible signatures of atmospheric gas circulation in the volcano. *Journal of Geophysical Research: Planets*, *117*(E9), 2012JE004050. https://doi.org/10.1029/2012JE004050

Macdonald, G. A. (1953). Pahoehoe, aa, and block lava. *American Journal of Science*, *251*(3), 169–191. https://doi.org/10.2475/ajs.251.3.169

Makowska, M., Mège, D., Gueydan, F., & Chéry, J. (2016). Mechanical conditions and modes of paraglacial deep-seated gravitational spreading in Valles Marineris, Mars. *Geomorphology*, *268*, 246–252. https://doi.org/10.1016/j.geomorph.2016.06.011

Malin, M. C., Bell, J. F., Cantor, B. A., Caplinger, M. A., Calvin, W. M., Clancy, R. T., Edgett, K. S., Edwards, L., Haberle, R. M., James, P. B., Lee, S. W., Ravine, M. A., Thomas, P. C., & Wolff, M. J. (2007). Context Camera Investigation on board the Mars Reconnaissance Orbiter. *Journal of Geophysical Research*, *112*(E5), E05S04. https://doi.org/10.1029/2006JE002808

Masursky, H. (1973). An overview of geological results from Mariner 9. *Journal of Geophysical Research*, *78*(20), 4009–4030. https://doi.org/10.1029/JB078i020p04009

Mayer, D. P., & Kite, E. S. (2016). An Integrated Workflow for Producing Digital Terrain Models of Mars from CTX and HiRISE Stereo Data Using the NASA Ames Stereo Pipeline, 1241
ADS Bibcode: 2016LPI....47.1241M.

McCauley, J., Carr, M., Cutts, J., Hartmann, W., Masursky, H., Milton, D., Sharp, R., & Wilhelms, D. (1972). Preliminary mariner 9 report on the geology of Mars. *Icarus*, *17*(2), 289–327. https://doi.org/10.1016/0019-1035(72)90003-6

McEwen, A. S., Eliason, E. M., Bergstrom, J. W., Bridges, N. T., Hansen, C. J., Delamere, W. A., Grant, J. A., Gulick, V. C., Herkenhoff, K. E., Keszthelyi, L., Kirk, R. L., Mellon, M. T., Squyres, S. W., Thomas, N., & Weitz, C. M. (2007). Mars Reconnaissance Orbiter's High Resolution Imaging Science Experiment (HiRISE). *Journal of Geophysical Research*, *112*(E5), E05S02. https://doi.org/10.1029/2005JE002605

Mège, D., & Bourgeois, O. (2011). Equatorial glaciations on Mars revealed by gravitational collapse of Valles Marineris wallslopes. *Earth and Planetary Science Letters*, *310*(3-4), 182–191. https://doi.org/10.1016/j.epsl.2011.08.030

Mège, D., Cook, A. C., Garel, E., Lagabrielle, Y., & Cormier, M.-H. (2003). Volcanic rifting at Martian grabens. *Journal of Geophysical Research: Planets*, *108*(E5), 2002JE001852. https://doi.org/10.1029/2002JE001852

Mège, D., & Masson, P. (1996a). Amounts of crustal stretching in Valles Marineris, Mars. *Planetary and Space Science*, *44*(8), 749–781. https://doi.org/10.1016/0032-0633(96)00013-X

Mège, D., & Masson, P. (1996b). A plume tectonics model for the Tharsis province, Mars. *Planetary and Space Science*, *44*(12), 1499–1546. https://doi.org/10.1016/S0032-0633(96)00113-4

Melosh, H. (1980). Tectonic patterns on a reoriented planet: Mars. *Icarus*, *44*(3), 745–751. https://doi.org/10.1016/0019-1035(80)90141-4

Michael, G., & Neukum, G. (2010). Planetary surface dating from crater size–frequency distribution measurements: Partial resurfacing events and statistical age uncertainty. *Earth and Planetary Science Letters*, *294*(3-4), 223–229. https://doi.org/10.1016/j.epsl.2009.12.041

Moore, H. J., & Hodges, C. A. (1980, January). *Some Martian volcanic centgers with small edifices.* (tech. rep.).
ADS Bibcode: 1980rpgp.rept..266M.

Mouginis-Mark, P. J. (2002). Prodigious ash deposits near the summit of Arsia Mons volcano, Mars: ASH DEPOSITS ON ARSIA MONS. *Geophysical Research Letters*, *29*(16), 15-1-15–4. https://doi.org/10.1029/2002GL015296

Mouginis-Mark, P. J., Zimbelman, J. R., Crown, D. A., Wilson, L., & Gregg, T. K. (2022). Martian volcanism: Current state of knowledge and known unknowns. *Geochemistry*, *82*(4), 125886. https://doi.org/10.1016/j.chemer.2022.125886

Muirhead, B. K., Nicholas, A., & Umland, J. (2020). Mars Sample Return Mission Concept Status. *2020 IEEE Aerospace Conference*, 1–8. https://doi.org/10.1109/AERO47225.2020.9172609

Muller, J.-P., Tao, Y., Putri, A. R. D., & Conway, S. J. (2021). 3D MULTI-RESOLUTION MAPPING OF MARS USING CASP-GO ON HRSC, CRISM, CTX AND HIRISE. *The International Archives of the Photogrammetry, Remote Sensing and Spatial Information Sciences*, *XLIII-B3-2021*, 667–671. https://doi.org/10.5194/isprs-archives-XLIII-B3-2021-667-2021

Neukum, G., & Jaumann, R. (2004). HRSC: The High Resolution Stereo Camera of Mars Express. *1240*, 17–35
ADS Bibcode: 2004ESASP1240...17N.

Orosei, R., Rossi, A. P., Cantini, F., Caprarelli, G., Carter, L. M., Papiano, I., Cartacci, M., Cicchetti, A., & Noschese, R. (2017). Radar sounding of Lucus Planum, Mars, by MARSIS: RADAR SOUNDING OF LUCUS PLANUM. *Journal of*

*Geophysical Research: Planets*, *122*(7), 1405–1418. https://doi.org/10.1002/2016JE005232

Pedersen, G., Höskuldsson, A., Dürig, T., Thordarson, T., Jónsdóttir, I., Riishuus, M., Óskarsson, B., Dumont, S., Magnusson, E., Gudmundsson, M., Sigmundsson, F., Drouin, V., Gallagher, C., Askew, R., Gudnason, J., Moreland, W., Nikkola, P., Reynolds, H., & Schmith, J. (2017). Lava field evolution and emplacement dynamics of the 2014–2015 basaltic fissure eruption at Holuhraun, Iceland. *Journal of Volcanology and Geothermal Research*, *340*, 155–169. https://doi.org/10.1016/j.jvolgeores.2017.02.027

Peterson, D. W., & Tilling, R. I. (1980). Transition of basaltic lava from pahoehoe to aa, Kilauea Volcano, Hawaii: Field observations and key factors. *Journal of Volcanology and Geothermal Research*, *7*(3-4), 271–293. https://doi.org/10.1016/0377-0273(80)90033-5

Plesa, A.-C., Wieczorek, M., Knapmeyer, M., Rivoldini, A., Walterová, M., & Breuer, D. (2022). Interior dynamics and thermal evolution of Mars – a geodynamic perspective. In *Advances in Geophysics* (pp. 179–230, Vol. 63). Elsevier. https://doi.org/10.1016/bs.agph.2022.07.005

Plescia, J. B. (2004a). Morphometric properties of Martian volcanoes. *Journal of Geophysical Research*, *109*(E3), E03003. https://doi.org/10.1029/2002JE002031

Plescia, J. B. (2004b). Morphometric properties of Martian volcanoes. *Journal of Geophysical Research: Planets*, *109*(E3), 2002JE002031. https://doi.org/10.1029/2002JE002031

Plescia, J. B. (1981). The Tempe volcanic province of Mars and comparisons with the Snake River Plains of Idaho. *Icarus*, *45*(3), 586–601. https://doi.org/10.1016/0019-1035(81)90024-5

Price, L. W. (1974). THE DEVELOPMENTAL CYCLE OF SOLIFLUCTION LOBES$_*$. *Annals of the Association of American Geographers*, *64*(3), 430–438. https://doi.org/10.1111/j.1467-8306.1974.tb00991.x

Putri, A. R. D., Sidiropoulos, P., Muller, J.-P., Walter, S. H., & Michael, G. G. (2019). A New South Polar Digital Terrain Model of Mars from the High-Resolution Stereo Camera (HRSC) onboard the ESA Mars Express. *Planetary and Space Science*, *174*, 43–55. https://doi.org/10.1016/j.pss.2019.02.010

Rampino, M. R., & Stothers, R. B. (1988). Flood Basalt Volcanism During the Past 250 Million Years. *Science*, *241*(4866), 663–668. https://doi.org/10.1126/science.241.4866.663

Re, C., Fennema, A., Simioni, E., Sutton, S., Mège, D., Gwinner, K., Józefowicz, M., Munaretto, G., Pajola, M., Petrella, A., Pommerol, A., Cremonese, G., & Thomas, N. (2022). CaSSIS-based stereo products for Mars after three years in orbit. *Planetary and Space Science*, *219*, 105515. https://doi.org/10.1016/j.pss.2022.105515

Richardson, J. A., Wilson, J. A., Connor, C. B., Bleacher, J. E., & Kiyosugi, K. (2017). Recurrence rate and magma effusion rate for the latest volcanism on Arsia

Mons, Mars. *Earth and Planetary Science Letters*, *458*, 170–178. https://doi.org/10.1016/j.epsl.2016.10.040

Richardson, L. F. (1961). The problem of contiguity: An appendix to Statistics of Deadly Quarrels. Yearbook of the Society for General Systems Research. *General System Yearbook*, *6*, 139–187.

Riedel, C., Michael, G., Kneissl, T., Orgel, C., Hiesinger, H., & Van Der Bogert, C. H. (2018). A New Tool to Account for Crater Obliteration Effects in Crater Size-Frequency Distribution Measurements. *Earth and Space Science*, *5*(6), 258–267. https://doi.org/10.1002/2018EA000383

Roberts, J. H., & Zhong, S. (2007). The cause for the north–south orientation of the crustal dichotomy and the equatorial location of Tharsis on Mars. *Icarus*, *190*(1), 24–31. https://doi.org/10.1016/j.icarus.2007.03.002

Rowland, S. K., & Walker, G. P. L. (1987). Toothpaste lava: Characteristics and origin of a lava structural type transitional between pahoehoe and aa. *Bulletin of Volcanology*, *49*(4), 631–641. https://doi.org/10.1007/BF01079968

Ruff, S. W., & Christensen, P. R. (2002). Bright and dark regions on Mars: Particle size and mineralogical characteristics based on Thermal Emission Spectrometer data. *Journal of Geophysical Research: Planets*, *107*(E12). https://doi.org/10.1029/2001JE001580

Runyon, K. D., Viviano, C. E., & Day, M. (2021). Abraded pyroclastic linear paleodunes in syria and daedalia plana, mars. *Earth and Planetary Science Letters*, *557*, 116719. https://doi.org/10.1016/j.epsl.2020.116719

Scanlon, K. E., Head, J. W., & Marchant, D. R. (2015). Volcanism-induced, local wet-based glacial conditions recorded in the Late Amazonian Arsia Mons tropical mountain glacier deposits. *Icarus*, *250*, 18–31. https://doi.org/10.1016/j.icarus.2014.11.016

Schaefer, E. I., Hamilton, C. W., Neish, C. D., Sori, M. M., Bramson, A. M., & Beard, S. P. (2021). Reexamining the Potential to Classify Lava Flows From the Fractality of Their Margins. *Journal of Geophysical Research: Solid Earth*, *126*(5), e2020JB020949. https://doi.org/10.1029/2020JB020949

Scott, D. H., & Tanaka, K. L. (1986). *Geologic map of the western equatorial region of Mars* (tech. rep.). https://doi.org/10.3133/i1802A

Settle, M. (1979). Formation and deposition of volcanic sulfate aerosols on Mars. *Journal of Geophysical Research*, *84*(B14), 8343. https://doi.org/10.1029/JB084iB14p08343

Shean, D. E., Head, J. W., Fastook, J. L., & Marchant, D. R. (2007). Recent glaciation at high elevations on Arsia Mons, Mars: Implications for the formation and evolution of large tropical mountain glaciers. *Journal of Geophysical Research: Planets*, *112*(E3), 2006JE002761. https://doi.org/10.1029/2006JE002761

Sides, S. C., Becker, T. L., Becker, K. J., Edmundson, K. L., Backer, J. W., Wilson, T. J., Weller, L. A., Humphrey, I. R., Berry, K. L., Shepherd, M. R., Hahn, M. A., Rose, C. C., Rodriguez, K., Paquette, A. S., Mapel, J. A., Shinaman,

J. R., & Richie, J. O. (2017). The USGS Integrated Software for Imagers and Spectrometers (ISIS 3) Instrument Support, New Capabilities, and Releases, 2739

ADS Bibcode: 2017LPI....48.2739S.

Silburt, A., Ali-Dib, M., Zhu, C., Jackson, A., Valencia, D., Kissin, Y., Tamayo, D., & Menou, K. (2019). Lunar crater identification via deep learning. *Icarus*, *317*, 27–38. https://doi.org/10.1016/j.icarus.2018.06.022

Smets, B., Wauthier, C., & d'Oreye, N. (2010). A new map of the lava flow field of Nyamulagira (D.R. Congo) from satellite imagery. *Journal of African Earth Sciences*, *58*(5), 778–786. https://doi.org/10.1016/j.jafrearsci.2010.07.005

Smith, D. E., Zuber, M. T., Frey, H. V., Garvin, J. B., Head, J. W., Muhleman, D. O., Pettengill, G. H., Phillips, R. J., Solomon, S. C., Zwally, H. J., Banerdt, W. B., Duxbury, T. C., Golombek, M. P., Lemoine, F. G., Neumann, G. A., Rowlands, D. D., Aharonson, O., Ford, P. G., Ivanov, A. B., … Sun, X. (2001). Mars Orbiter Laser Altimeter: Experiment summary after the first year of global mapping of Mars. *Journal of Geophysical Research: Planets*, *106*(E10), 23689–23722. https://doi.org/10.1029/2000JE001364

Smith, D. E., Zuber, M. T., Solomon, S. C., Phillips, R. J., Head, J. W., Garvin, J. B., Banerdt, W. B., Muhleman, D. O., Pettengill, G. H., Neumann, G. A., Lemoine, F. G., Abshire, J. B., Aharonson, O., David, C., Brown, Hauck, S. A., Ivanov, A. B., McGovern, P. J., Zwally, H. J., & Duxbury, T. C. (1999). The Global Topography of Mars and Implications for Surface Evolution. *Science*, *284*(5419), 1495–1503. https://doi.org/10.1126/science.284.5419.1495

Spudis, P. D. (2015). Volcanism on the Moon. In *The Encyclopedia of Volcanoes* (pp. 689–700). Elsevier. https://doi.org/10.1016/B978-0-12-385938-9.00039-0

Stevenson, D. S. (2018). Our Island Earth: Granite Here, Granite Everywhere? In *Granite Skyscrapers* (pp. 287–337). Springer International Publishing. https://doi.org/10.1007/978-3-319-91503-6_7

Stewart, E. M., & Head, J. W. (2001). Ancient Martian volcanoes in the Aeolis region: New evidence from MOLA data. *Journal of Geophysical Research: Planets*, *106*(E8), 17505–17513. https://doi.org/10.1029/2000JE001322

Tanaka, K. L., & Davis, P. A. (1988). Tectonic history of the Syria Planum province of Mars. *Journal of Geophysical Research: Solid Earth*, *93*(B12), 14893–14917. https://doi.org/10.1029/JB093iB12p14893

Tanaka, K. L., Robbins, S., Fortezzo, C., Skinner, J., & Hare, T. (2014). The digital global geologic map of Mars: Chronostratigraphic ages, topographic and crater morphologic characteristics, and updated resurfacing history. *Planetary and Space Science*, *95*, 11–24. https://doi.org/10.1016/j.pss.2013.03.006

Thomas, N., Cremonese, G., Ziethe, R., Gerber, M., Brändli, M., Bruno, G., Erismann, M., Gambicorti, L., Gerber, T., Ghose, K., Gruber, M., Gubler, P., Mischler, H., Jost, J., Piazza, D., Pommerol, A., Rieder, M., Roloff, V., Servonet, A., … Wray, J. J. (2017). The Colour and Stereo Surface Imaging System (CaSSIS)

for the ExoMars Trace Gas Orbiter. *Space Science Reviews*, *212*(3-4), 1897–1944. https://doi.org/10.1007/s11214-017-0421-1

Tomasi, I., Massironi, M., Meyzen, C. M., Pozzobon, R., Sauro, F., Penasa, L., Santagata, T., Tonello, M., Santana Gomez, G. D., & Martinez-Frìas, J. (2022). Inception and Evolution of La Corona Lava Tube System (Lanzarote, Canary Islands, Spain). *Journal of Geophysical Research: Solid Earth*, *127*(6), e2022JB024056. https://doi.org/10.1029/2022JB024056

Tomasi, I., Tonello, M., Massironi, M., Tesson, P.-A., Sauro, F., Meyzen, C. M., Martìnez-Frìas, J., & Mederos, E. M. (2023). Geology of Lanzarote's northern region (Canary Island, Spain). *Journal of Maps*, 1–14. https://doi.org/10.1080/17445647.2023.2187717

Tornabene, L. L., Seelos, F. P., Pommerol, A., Thomas, N., Caudill, C. M., Becerra, P., Bridges, J. C., Byrne, S., Cardinale, M., Chojnacki, M., Conway, S. J., Cremonese, G., Dundas, C. M., El-Maarry, M. R., Fernando, J., Hansen, C. J., Hansen, K., Harrison, T. N., Henson, R., … Wray, J. J. (2018). Image Simulation and Assessment of the Colour and Spatial Capabilities of the Colour and Stereo Surface Imaging System (CaSSIS) on the ExoMars Trace Gas Orbiter. *Space Science Reviews*, *214*(1), 18. https://doi.org/10.1007/s11214-017-0436-7

Vago, J., Witasse, O., Svedhem, H., Baglioni, P., Haldemann, A., Gianfiglio, G., Blancquaert, T., McCoy, D., & de Groot, R. (2015). ESA ExoMars program: The next step in exploring Mars. *Solar System Research*, *49*(7), 518–528. https://doi.org/10.1134/S0038094615070199

Vincendon, M. (2013). Mars surface phase function constrained by orbital observations. *Planetary and Space Science*, *76*, 87–95. https://doi.org/10.1016/j.pss.2012.12.005

Vincendon, M., Forget, F., & Mustard, J. (2010). Water ice at low to midlatitudes on Mars. *Journal of Geophysical Research*, *115*(E10), E10001. https://doi.org/10.1029/2010JE003584

Wadge, G., & Lopes, R. (1991). The lobes of lava flows on Earth and Olympus Mons, Mars. *Bulletin of Volcanology*, *54*(1), 10–24. https://doi.org/10.1007/BF00278203

Washington, H. S. (1922). Deccan traps and other plateau basalts. *Geological Society of America Bulletin*, *33*(4), 765–804. https://doi.org/10.1130/GSAB-33-765

Weitz, C. M., Milliken, R. E., Grant, J. A., McEwen, A. S., Williams, R. M. E., & Bishop, J. L. (2008). Light-toned strata and inverted channels adjacent to Juventae and Ganges chasmata, Mars. *Geophysical Research Letters*, *35*(19). https://doi.org/10.1029/2008gl035317

Werner, S. C. (2009). The global martian volcanic evolutionary history. *Icarus*, *201*(1), 44–68. https://doi.org/10.1016/j.icarus.2008.12.019

Westall, F., Loizeau, D., Foucher, F., Bost, N., Betrand, M., Vago, J., & Kminek, G. (2013). Habitability on Mars from a Microbial Point of View. *Astrobiology*, *13*(9), 887–897. https://doi.org/10.1089/ast.2013.1000

Whelley, P., Matiella Novak, A., Richardson, J., Bleacher, J., Mach, K., & Smith, R. N. (2021). Stratigraphic Evidence for Early Martian Explosive Volcanism in Arabia Terra. *Geophysical Research Letters*, *48*(15). https://doi.org/10.1029/2021GL094109

White, R. S., & McKenzie, D. (1995). Mantle plumes and flood basalts. *Journal of Geophysical Research: Solid Earth*, *100*(B9), 17543–17585. https://doi.org/10.1029/95JB01585

Wiedeking, S., Lentz, A., Pasckert, J. H., Raack, J., Schmedemann, N., & Hiesinger, H. (2023). Rheological properties and ages of lava flows on Alba Mons, Mars. *Icarus*, *389*, 115267. https://doi.org/10.1016/j.icarus.2022.115267

Wilson, J. T. (1963). A POSSIBLE ORIGIN OF THE HAWAIIAN ISLANDS. *Canadian Journal of Physics*, *41*(6), 863–870. https://doi.org/10.1139/p63-094

Wilson, L., & Head, J. W. (1994). Mars: Review and analysis of volcanic eruption theory and relationships to observed landforms. *Reviews of Geophysics*, *32*(3), 221. https://doi.org/10.1029/94RG01113

Wilson, L., Scott, E. D., & Head, J. W. (2001a). Evidence for episodicity in the magma supply to the large Tharsis volcanoes. *Journal of Geophysical Research: Planets*, *106*(E1), 1423–1433. https://doi.org/10.1029/2000JE001280

Wilson, L., Scott, E. D., & Head, J. W. (2001b). Evidence for episodicity in the magma supply to the large Tharsis volcanoes. *Journal of Geophysical Research: Planets*, *106*(E1), 1423–1433. https://doi.org/10.1029/2000JE001280

Wise, D. U., Golombek, M. P., & McGill, G. E. (1979). Tharsis province of Mars: Geologic sequence, geometry, and a deformation mechanism. *Icarus*, *38*(3), 456–472. https://doi.org/10.1016/0019-1035(79)90200-8

Zimbelman, J. R. (1998). Emplacement of long lava flows on planetary surfaces. *Journal of Geophysical Research: Solid Earth*, *103*(B11), 27503–27516. https://doi.org/10.1029/98JB01123

Zuber, M. T., & Smith, D. E. (1997). Mars without Tharsis. *Journal of Geophysical Research: Planets*, *102*(E12), 28673–28685. https://doi.org/10.1029/97JE02527

Zurek, R. W., & Smrekar, S. E. (2007). An overview of the Mars Reconnaissance Orbiter (MRO) science mission. *Journal of Geophysical Research*, *112*(E5), E05S01. https://doi.org/10.1029/2006JE002701